
**Extraction of
Mercury's tidal signal and libration amplitude
from synthetic laser altimeter data sets**

Von der Fakultät für Bauingenieurwesen und Geodäsie
der Gottfried Wilhelm Leibniz Universität Hannover
zur Erlangung des Grades

DOKTOR - INGENIEUR

genehmigte Dissertation
von

Dipl.-Ing. Christian Koch

HANNOVER 2009

Diese Arbeit ist gleichzeitig veröffentlicht in:
Wissenschaftliche Arbeiten der Fachrichtung Geodäsie und Geoinformatik
der Leibniz Universität Hannover
ISSN 0174-1454, Nr. 280, Hannover 2009

Referent: Prof. Dr.-Ing. habil. Jürgen Müller
Korreferenten: Prof. Dr. rer.nat. Ulrich R. Christensen
Prof. Dr.-Ing. habil. Christian Heipke

Tag der mündlichen Prüfung: 25. Juni 2009

Summary

Within the next decade, two space missions will investigate Mercury, the innermost planet of the solar system. NASA's MESSENGER spacecraft is presently on its way to Mercury and will be inserted into orbit in 2011, while BepiColombo will be launched in 2014 to arrive at Mercury after a six-year-cruise in 2020. Both missions apply laser altimeters to map the global topography and to extract the tidal signal of Mercury's surface which occurs due to solar gravitation. The purpose of this study is to investigate different analysis methods which allow to extract the tidal elevation, expressed by the dimensionless tidal Love number h_2 . The determination of the Love number h_2 is one of the very few methods that allows to study the interior of a planet from orbiting spacecraft. Provided that Mercury has a liquid outer core, the tidal elevation amplitude is of order 1 m, corresponding to a Love number $h_2 \approx 0.7$ (Van Hoolst and Jacobs 2003), otherwise it is much smaller. Furthermore, it shall be confirmed with high confidence in the frame of the BepiColombo mission that Mercury consists of a solid inner core and a liquid outer shell. First experimental evidence for Mercury's core not being completely solid has been found by Margot et al. (2007). They used Earth-based radar interferometry, the well-known experiment proposed by Peale (1976a), to determine a value of (35.8 ± 2.0) arcsec for the amplitude Φ_{lib} of the 88-day forced libration due to torques from solar gravitation on Mercury's non-spherical mass distribution. This value suggests that only Mercury's mantle follows the solar torques, i.e. that the mantle can slip with respect to the core at the core mantle boundary. Both the tidal signal as well as the libration of Mercury describe the reaction of Mercury as a differentiated elastic body to the solar tidal forces. A combined precise determination of both the tidal Love number h_2 and the forced libration amplitude Φ_{lib} allows to put constraints on the radii of Mercury's inner and outer core which are determined by the initial sulfur content. For instance, an extraction of the tidal Love number with a precision of 10 % allows to determine the outer core radius down to an uncertainty of several tens of kilometers. In a somewhat different way, the libration amplitude depends on the core radius and, therefore, on the sulfur content of the core. With a precise knowledge of the interior structure of Mercury models can be improved which explain the origin of Mercury's weak magnetic field.

The potential science return from data of the BepiColombo laser altimeter BELA, which is adapted to the larger of the two BepiColombo satellites, the Mercury Planetary Orbiter (MPO), is investigated and analyzed. A precise determination of the tidal signal is a challenging goal as the single-shot measurement uncertainty of BELA approximately equals to the expected maximum tidal amplitude of Mercury. The time-dependent tidal signal needs to be distinguished from the static surface topography of Mercury. Therefore, the tidal signal can only be extracted by determining the global topography simultaneously. Three approaches are investigated in more detail for determining the tidal Love

number. For the extraction of the libration amplitude, which is considered a less important goal for BELA, only one method is explored, as the libration amplitude will also be determined by the SIMBIO-SYS camera onboard the BepiColombo spacecraft.

BELA data cannot be expected to be received from the BepiColombo mission before the years 2020 and 2021. Therefore, the yet unknown topography of Mercury is synthesized in the form of a spherical harmonic expansion where the degree power follows a power law with index -2 . At low spherical harmonic degrees, this power law approximately reproduces the lunar topography. The synthetic BELA data include an uncertainty of about 62.5 m mainly due to the not-modeled small-scale topography and to less extent because of the limited measurement precision.

The first approach uses a spherical harmonic expansion of the global surface topography where the coefficients are directly determined by a least-squares inversion of the simulated laser altimeter measurements. But it has the main advantage that surface topography data can directly be correlated with gravity measurements. It has one main disadvantage in that computations are time-consuming, as each single laser shot contributes to all coefficients of the global topography expressed as a spherical harmonic expansion. With this method the topography coefficients can be extracted with small uncertainties of less than 1 m down to a few centimeters for the lower harmonic degrees. The tidal signal is retrieved with an uncertainty of about 10 % (2σ -uncertainty) for the most realistic case where a non-resonant orbit and the data restriction for spacecraft altitudes up to 1000 km are included. The libration amplitude is retrieved with an uncertainty which is comparable with that retrieved by Earth-based radar interferometry (Margot et al. 2007).

The second method of using local basis functions defined in the near neighborhood of cells of a rectangular grid has the main advantage in that the computation time is significantly lower than for the global basis functions method. Due to the high shot density along the spacecraft track, which has almost fixed longitude, the basis functions are chosen to be simple step functions in latitudinal direction. In longitude direction in addition to step functions, linear and cubic spline functions have been used. The extracted topography is expressed as a rectangular grid with integer binning factors in latitude and longitude with respect to the grid of the synthetic input topography. Optimum binning, i.e. highest precision of the extracted Love number, is achieved when the output grid cell dimension is similar to the distance between two spacecraft tracks. The tidal Love number can be extracted with a precision of about 14 % (2σ -uncertainty) for the realistic case where a non-resonant orbit and the restriction, that data can only be obtained up to 1000 km spacecraft altitude, is simulated. Better results are retrieved for a resonant orbit and especially without data restriction due to the spacecraft altitude. This restriction typically reduces the number of measurements to one half compared to the case where data are used all over the orbit.

A third method has been developed to retrieve the tidal signal from an analysis at orbit crossover points without a full determination of the global static topography. The method is an alternative to check the results obtained from the other methods where the global static topography is extracted simultaneously with the tidal signal. Crossovers can mainly be found in the polar regions of Mercury. Due to Mercury's eccentric orbit around the Sun the tidal signal should still be significant at the poles. The tidal phase difference at such crossovers varies so that roughly speaking half of the crossovers can be considered to be useful to determine the tidal amplitude, while the other half can be taken to calibrate the

spacecraft altitude. The largest uncertainty for the crossover analysis arises from unknown small-scale topography between the crossover point and the next neighboring laser shots. It turns out that a rather significant number of crossover points is available for precise determination of the tidal Love number h_2 .

Keywords

Tidal Love number, forced libration amplitude, laser altimetry, Mercury, planetary topography, BepiColombo, least squares adjustment

Zusammenfassung

Innerhalb des nächsten Jahrzehnts werden zwei Weltraummissionen Merkur, den innersten Planeten des Sonnensystems, untersuchen. NASAs MESSENGER Raumsonde ist auf dem Weg zu Merkur und wird 2011 in der Umlaufbahn sein, während BepiColombo 2014 gestartet und Merkur nach sechs Jahren erreichen wird. Beide Missionen enthalten Laseraltimeter, um die globale Topographie zu kartographieren und das Gezeitensignal der Oberfläche von Merkur zu bestimmen, das durch die Gravitation der Sonne entsteht. Das Ziel der Arbeit ist die Untersuchung verschiedener Analysemethoden, um die dimensionslose Lovezahl h_2 zu bestimmen, die Information über den inneren Aufbau von Merkur enthält. Die Bestimmung der Lovezahl h_2 ist eine der wenigen Methoden, die Untersuchungen der inneren Struktur eines Planeten aus Beobachtungen einer Raumsonde erlaubt. Des Weiteren soll im Rahmen der BepiColombo Mission mit hoher Präzision untersucht werden, ob Merkur aus einem festen inneren und flüssigen äußeren Kern besteht. Sofern Merkur eine flüssigen äußeren Kern hat, wäre das Gezeitensignal in der Größenordnung von 1 m und gleichbedeutend mit einer Lovezahl von $h_2 \approx 0.7$ (Van Hoolst and Jacobs 2003), ansonsten weitaus geringer. Erste experimentelle Beweise, dass Merkur keinen komplett festen Kern hat, wurden von Margot et al. (2007) gefunden. Sie haben bodengestützte Radarinterferometrie verwendet; diese Beobachtungsmethode wurde bereits von Peale (1976a) vorgeschlagen. Für die Amplitude der 88 Tage dauernden, erzwungenen Libration Φ_{lib} , die aufgrund von Drehmomenten der solaren Gravitation auf Merkurs nichtsphärische Massenverteilung entsteht, wurde ein Wert von (35.8 ± 2.0) arcsec bestimmt. Dieser Wert deutet darauf hin, dass nur Merkurs Mantel den solaren Drehmomenten folgt. Das heisst, dass der Mantel im Vergleich zum Kern an der Kern-Mantel-Grenze verrutschen kann. Sowohl die Messung des Gezeitensignals als auch der Libration von Merkur als elastischen Körper beschreiben die Reaktion auf die solaren Gravitationskräfte. Eine kombinierte präzise Bestimmung der gezeitenabhängigen Lovezahl h_2 und der erzwungenen Librationsamplitude Φ_{lib} erlaubt, klare Grenzen für die inneren Strukturen Merkurs aufzuzeigen. Die Extraktion der Gezeiten-Lovezahl mit einer Genauigkeit von 10 % ermöglicht die Bestimmung des äußeren Kernradius bis zu einer Größenordnung von einigen Kilometern. Die Librationsamplitude hängt von der Kerngröße ab, und dies ist äquivalent mit dem Schwefelgehalt im Kern. Mit einer detaillierten Kenntnis über die innere Struktur Merkurs können Modelle verbessert werden, die dessen schwaches Magnetfeld erklären.

Das Potential der erwarteten wissenschaftlichen Resultate des BepiColombo Laseraltimeters (BELA), eines der Instrumente der größeren der beiden Raumsonden, dem Mercury Planetary Orbiter (MPO), wird untersucht und analysiert. Eine genaue Bestimmung des Gezeitensignals ist eine Herausforderung, da die Messunsicherheit der Lasermessung von BELA der erwarteten maximalen Gezeitenamplitude von Merkur entspricht. Das

zeitabhängige Gezeitensignal muss von Merkurs statischer Topographie unterschieden werden. Daher kann das Gezeitensignal nur mit einer simultanen Bestimmung der globalen Topographie erfolgen. Drei Ansätze werden für die Bestimmung der Gezeiten-Lovezahl im Detail untersucht. Für die Extrahierung der Librationsamplitude wird nur eine Methode verwendet, da diese keine so hohe Priorität als wissenschaftliches Ziel für BELA darstellt und sie mit der Kamera SIMBIO-SYS, die an der Raumsonde der Bepi-Colombo angebracht ist, ohnehin auch anderweitig bestimmt werden soll.

BELA Daten können nicht vor 2020 und 2021 erwartet werden. Die bisher unbekannt Topographie des Merkur wird synthetisch durch eine Kugelfunktionsentwicklung erzeugt, deren Leistungsdichte einem Potenzgesetz mit Exponent -2 folgt. Dieses Potenzgesetz ähnelt für niedrige Grade der Kugelfunktionsentwicklung der Mondtopographie. Wegen nicht im Modell enthaltener Topographievariationen kleiner Maßstäbe, und zu einem geringeren Maß aufgrund begrenzter Messpräzision beinhalten die synthetischen BELA Daten eine Unsicherheit von 62.5 m.

Der erste Ansatz verwendet eine Kugelfunktionsentwicklung zur Beschreibung der globalen Topographie, und die Koeffizienten werden direkt durch eine Inversion nach der Methode der kleinsten Quadrate aus simulierten Lasermessungen bestimmt. Die Methode hat den Vorteil, dass die Oberflächentopographie direkt mit dem Schwerfeldmessungen korreliert werden können, und den Nachteil, dass die Berechnungen zeitaufwändig sind, da jede Lasermessung die gesamte Topographie-Darstellung, beschrieben als Kugelfunktionen, beeinflusst. Die Topographiekoeffizienten können mit einer Unsicherheit besser als 1 m bis zu wenigen Zentimetern für niedrige harmonische Grade extrahiert werden. Das Gezeitensignal wird mit einer Unsicherheit von 10 % (2σ -Unsicherheit) für den realistischsten Fall bestimmt, bei dem ein nicht-resonanter Orbit und eine Datenrestriktion für Raumsondenhöhen bis zu 1000 km verwendet werden. Die Librationsamplitude wurde mit einer vergleichbaren Unsicherheit wie durch erdgebundene Radarinterferometrie von Margot et al. (2007) extrahiert.

Der zweite Ansatz basiert auf lokalen Basisfunktionen, die in der lokalen Umgebung von Rechteckgitterpunkten definiert sind. In Breitenrichtung werden wegen der großen Anzahl an zu erwartenden Messungen Stufenfunktionen als Basisfunktionen gewählt. In Längenrichtung werden zusätzlich zu den Stufenfunktionen noch lineare und kubische Spline Funktionen verwendet. Die extrahierte Topographie ist als Rechteckgitter mit ganzzahligen Faktoren in Gitterlänge und -breite im Vergleich zu dem Gitter der synthetischen Topographie definiert. Höchste Genauigkeit für die Lovezahl wird erreicht, wenn die Anzahl der Gitterpunkte der extrahierten Topographie dem Abstand von zwei Satellitenspuren entspricht. Die Lovezahl kann für den realistischsten Fall mit einer Unsicherheit von 14 % (2σ -Unsicherheit) bestimmt werden. Bessere Resultate werden für einen resonanten Orbit und ohne Beschränkung der Anzahl an Messungen durch die Höhenrestriktion erreicht, die die Anzahl der Lasermessungen halbiert.

Bei der dritten Methode wird die globale Topographie vernachlässigt und eine Analyse von Kreuzungspunkten für die Extraktion des Gezeitensignals untersucht. Dieser Ansatz ist eine Alternative, um die Resultate der vorherigen Methoden zu überprüfen. Kreuzungspunkte werden hauptsächlich in den Polregionen von Merkur erwartet. Wegen Merkurs elliptischem Orbit um die Sonne sollte ein deutliches Gezeitensignal vorhanden sein. Die Gezeitensignaldifferenz variiert, so dass nur etwa die Hälfte der Kreuzungspunkte für die Bestimmung des Gezeitensignals verwendet werden können, während die

restlichen zur Kalibrierung der Raumsondenhöhe genutzt werden können. Den größten Einfluss bei der Kreuzungspunktanalyse hat die kleinskalige, unbekannte Topographie zwischen dem Kreuzungspunkt und dessen nächster Umgebung. Es zeigt sich, dass eine große Anzahl an Kreuzungspunkten für eine genaue Bestimmung der Lovezahl h_2 verfügbar ist.

Schlagwörter

Gezeiten-Lovezahl, Librationsamplitude, Laseraltimetrie, Merkur, planetare Topographie, BepiColombo, Kleinste-Quadrate-Ausgleichung

Contents

Contents	ix
List of Figures	xiii
List of Tables	xv
1 Motivation	1
2 Introduction	5
2.1 Mercury	5
2.1.1 Mercury – mythology and first observations	5
2.1.2 Mercury – the planet, surface and parameters	7
2.1.3 Mercury – the interior structure	11
2.2 Missions for exploring Mercury	11
2.2.1 Mariner10	12
2.2.2 MESSENGER	13
2.2.3 BepiColombo	13
2.3 Laser altimetry	16
2.3.1 Introduction to laser altimetry	16
2.3.2 Geoscience Laser Altimeter System (GLAS)	18
2.3.3 Mars Orbiter Laser Altimeter (MOLA)	20
2.3.4 Mercury Laser Altimeter (MLA)	21
2.3.5 BepiColombo Laser Altimeter (BELA)	21
2.4 Time-dependent variations of the topography	23
2.4.1 Tidal elevation	23
2.4.2 Libration amplitudes	26
3 Forward modelling of synthetic laser altimeter data	29
3.1 Deterministic topography model of Mercury	30
3.2 Distribution of laser shot points	31
3.3 Noise sources	33
4 Topography extraction by a spherical harmonic expansion	35
4.1 Introduction into the extraction by spherical harmonic analysis	36
4.2 Least-squares inversion	37
4.2.1 Inversion for topography and Love number	37
4.2.2 Inversion for the amplitude of forced libration	38

4.3	Optimization of the weighting scheme	39
4.3.1	Uniform surface coverage	39
4.3.2	Data restrictions	42
4.4	Orbit selection and its effect on the retrieved topography	45
4.5	Precision of the extracted Love number and libration amplitude	48
5	Topography extraction by a local basis function expansion	51
5.1	Introduction into the extraction by local basis function expansion	52
5.2	Inversion method	53
5.2.1	Local basis functions defined on topographic grid cells	54
5.2.2	Gaussian elimination of the inversion matrix with band structure	57
5.3	Optimization of data binning and weighting scheme	58
5.3.1	Analytical determination of the optimum combination of grid points	58
5.3.1.1	Input and output specifications	60
5.3.1.2	Longitudinal limitations	60
5.3.1.3	Estimate of the optimum longitudinal binning	60
5.3.1.4	Latitudinal limitations	61
5.3.1.5	Summary of the retrieved conditions	61
5.3.2	Optimizing the weighting scheme	62
5.4	Simulations for temporal and spatial data restrictions	66
5.4.1	Altitude restriction	66
5.4.2	Temporal restriction	67
5.4.3	Altitude and temporal restriction	69
5.4.4	Resonant versus non-resonant orbit	69
5.4.5	Orbital data coverage restriction	71
5.5	Transformation of the extracted topography into a spherical harmonic expansion	71
6	Extraction of the tidal signal at orbit crossovers in the polar regions	77
6.1	Introduction	77
6.2	Setup of the analysis	79
6.2.1	Positioning and instrumental uncertainties	79
6.2.2	Uncertainties related to small-scale topography	80
6.2.3	Uncertainties caused by interpolation	82
6.2.3.1	Cubic spline interpolation	82
6.2.3.2	Polynomial interpolation	83
6.2.4	Error propagation of the uncertainties	84
6.2.4.1	Basic equations for the error propagation	85
6.2.4.2	Derivatives for the error propagation	85
6.3	Results	86
6.3.1	Error propagation at a crossover	86
6.3.2	Mean uncertainty at the crossovers	90
6.3.3	Optimum selection of crossover points	92
7	Discussion of the results	95

8 Outlook	99
Bibliography	103
Publications	111
Acknowledgements	113
Curriculum Vitae	115

List of Figures

2.1	Elongations and conjunctions of an inferior planet(left panel); Mercury – the ancient god at the Central Station, Mainz, Germany (right panel)	6
2.2	Tolstoj Basin on Mercury (left panel); Mariner 10 image of Discovery Rupes (right panel)	8
2.3	Power spectral density of the topography of Mars and power spectral density corresponding to the degree power	9
2.4	Guiseppe Colombo (1920-1984), Italian scientist (left panel); the Mariner 10 spacecraft and its scientific payload (right panel)	12
2.5	MESSENGER spacecraft showing instrument accomodation (left panel); the operational orbit of MESSENGER (right panel)	13
2.6	Cruise trajectory of the BepiColombo mission to Mercury	15
2.7	BepiColombo spacecraft (left panel), operational orbits of the Mercury Planetary and Magnetospheric Orbiter (right panel)	16
2.8	Scheme of laser altimeter measurements	18
2.9	Maps of Mars’ global topography	20
2.10	Scheme of BELA	22
2.11	Geometry of the torque for Mercury’s spin axis	27
3.1	Simulated input topography for one specific random number	31
4.1	Harmonic degree power of the static input topography and errors of the inversion for constant weights and uniform surface coverage	40
4.2	Extracted time-dependent variations of the static topography vs. maximum harmonic degree of the static topography for uniform weights and a uniform surface coverage	41
4.3	Extracted Love number and libration amplitude vs. the simulation time for a fixed degree of inversion for the spherical harmonic expansion	43
4.4	Mean errors of the static topography coefficients as a function of harmonic degree for data all over the orbit and data limited to spacecraft altitudes up to 1000 km	43
4.5	Extracted Love number and libration amplitude for data limited to spacecraft altitudes up to 1000 km	44
4.6	Mean errors of the static topography coefficients as a function of harmonic degree for different orbits and restrictions	46
4.7	Results for the Love number and libration amplitude vs. maximum harmonic degree of inversion for a resonant orbit	46

4.8	Results for the Love number and libration amplitude vs. maximum harmonic degree of inversion for a non-resonant orbit	47
4.9	Errors of the tidal Love number and the libration amplitude vs. the maximum degree of inversion	48
5.1	Extracted tidal Love numbers and mean standard deviations for the prepared tests and different resolutions of the topography	63
5.2	Standard deviations of the topography with the same number of grid points for in- and output topography model without restrictions and equal weights for upper panel with $i_{long} = 1$, middle panel with $i_{long} = 2$, and lower panel with $i_{long} = 4$,	64
5.3	Standard deviations of the topography for all grid points for restricting the spatial coverage	67
5.4	Standard deviations of the topography for all grid points for restricting the temporal coverage	68
5.5	Standard deviations of the topography for all grid points for restricting the temporal and spatial coverage	69
5.6	Standard deviations of the topography for all grid points for a resonant spacecraft orbit	70
5.7	Harmonic degree power of the static input topography and errors of the direct backward transformation of the input topography as well as mean errors of the transformed output topography applying step functions as local basis functions with different binning of grid points in longitude	72
5.8	Mean errors of the transformed output topography applying now linear functions with different binning of grid points in longitude	73
5.9	Mean errors of the transformed output topography applying now cubic spline functions with different binning of grid points in longitude	74
6.1	Uncertainties of each single component for a crossover	88
6.2	Uncertainty at a crossover for the error propagation for a Polynomial interpolation with degree $n = 1$	89
6.3	Uncertainty of a crossover for the error propagation for a Polynomial interpolation with degree $n = 2$	90
6.4	Uncertainty of a crossover for the error propagation for a Polynomial interpolation with degree $n = 3$	90

List of Tables

2.1	Mercury parameters	10
2.2	Scientific payload of MESSENGER	14
2.3	Scientific payload of BepiColombo	15
2.4	Laser altimeter instrument parameters	19
3.1	MPO parameters	32
5.1	List of distances between satellite tracks for different orbits	59
5.2	Specifications for the output topographic grid in longitude direction	60
6.1	Uncertainties of the single error components for a crossover	87
6.2	Estimated mean uncertainties at the crossovers	91
6.3	Estimated uncertainties at the crossovers for a maximum uncertainty of the tidal Love number with less than 3 %	92

1 Motivation

Mercury is the inner most planet of the solar system. Due to its proximity to the Sun and its orbital parameters, it is the least investigated planet. Mercury has only been visited in 1974/75, when NASA's Mariner 10 spacecraft had three flybys, and very recently, in 2008, when NASA's Messenger spacecraft executed its first two flybys before insertion into orbit around the planet in 2011. Supported by ground-based observations, it has been concluded from the data of the Mariner 10 flybys that Mercury has the highest uncompressed density among the terrestrial planets. This high density implies a metal-to-silicate ratio of about 0.6 (Solomon et al. 2007). Mercury is expected to be differentiated into core and mantle. For a core made of nearly pure iron, the core radius is predicted to be approximately 0.75 times the planetary radius (Spohn et al. 2001). If the core contained substantial amounts of a light alloying element, sulfur being the prime candidate, its fractional radius could be much larger (Harder and Schubert 2001). The presence of a weak global magnetic field (Connerney and Ness 1988) can be explained by a hydromagnetic dynamo, which requires that the core is at least partly liquid. However, an origin by crustal magnetization (e.g. Aharonson et al. 2004) is also discussed in which case the magnetic field does not put any constraint on the present state of the core. Thermal evolution models (Hauck et al. 2004, Schubert et al. 1988) suggest that Mercury's core is probably partly liquid if it contains some sulfur. However, the size of the solid inner core has a wide possible range, depending mainly on the unknown sulfur content. For low (initial) sulfur concentration in the liquid core, it may presently form only a thin shell around a large solid core. The presence of a solid inner core is probably essential for driving a dynamo in the liquid part by compositional convection (Schubert et al. 1988), and its size may control the strength and geometry of the magnetic field (Christensen 2006, Heimpel et al. 2005, Stanley et al. 2005).

Geodetic observations made from orbiting spacecraft can put constraints on the internal structure of the planet. In particular, the response to solar tidal forcing is sensitive to the size and state of the metallic core. The tidal Love number k_2 quantifies the additional gravity potential, relative to a tide-generating potential due to the mass displaced by tidal force. For example, the value of $k_2 = 0.153 \pm 0.017$ inferred for the gravity tidal Love number of Mars from radio Doppler tracking of the Mars Global Surveyor spacecraft has been used to conclude that the core of Mars is not completely solid and has a radius of 1680 ± 160 km (Yoder et al. 2003). In the case of Mercury the tidal Love numbers h_2 and k_2 have been calculated to be approximately 0.7 and 0.4, respectively, if the core is partly liquid (Van Hoolst and Jacobs 2003). For a completely frozen core, they are much smaller. The precise value of h_2 depends primarily on the core radius and to some degree on the solid inner core radius, it is in the range of 0.6–0.9 for a liquid outer core. The two tidal Love numbers, of which h_2 describes the tidal deformation of the planet's sur-

face and k_2 the change of the gravity potential resulting from the distortion of the planet's mass distribution, depend in similar way on the internal structure and hence carry similar information. However, slight differences exist and if both Love numbers were known precisely it would be possible to remove ambiguities in the structural models that fit a given value of one of the Love numbers, e.g., trade-offs between core radius and inner core radius.

Another source of information on the internal structure comes from Mercury's forced libration, i.e., the slightly uneven rotation caused by the action of solar torques on the non-symmetric permanent mass distribution of the planet. The libration amplitude, in combination with low-order coefficients of the gravity potential and the obliquity of the rotation axis, allows constraining the ratio of the moment of inertia of the solid mantle, providing it is mechanically decoupled from the core (Peale 1972, 1976a, Peale et al. 2002). Like in the case of tides, the libration amplitude in combination with the other information will allow to distinguish a completely frozen core from a partly liquid core and, in the latter case it puts constraints on the core (Rambaux et al. 2007). While this requires some assumptions on the details of the density structure in the planet, the uncertainties may be less than in case of the quantitative interpretation of the Love numbers, which also requires assumptions on the rigidity.

While the gravity Love number k_2 is determined by tracking the spacecraft's orbit, h_2 can be obtained from the precise monitoring of changes in the planet's surface. A precision of 1 m by laser altimetry needs an accurate spacecraft position.

Various techniques can be employed to determine the libration amplitude. Margot et al. (2007) used Earth-based radar interferometry to determine a value of (35.8 ± 2.0) arc-sec for the 88-day libration. A more accurate determination may be possible from orbit, either by tracking of landmarks at the surface with precise imagery (e.g. Jehn et al. 2004, Wu et al. 1997) or by laser altimetry (Zuber et al. 2007). In the latter case, the offset of topographic structures compared to their location in a reference frame rotating at a uniform rate (or one rotating with a nominal libration) is treated as another time-dependent component of the surface topography.

The aim of this study is the investigation of methods for retrieving Mercury's tidal Love number h_2 and the amplitude of forced libration Φ_{lib} from synthetic topography data sets as taken by laser altimeter onboard a spacecraft orbiting Mercury. Two space missions will explore Mercury in the next decade, with elucidating Mercury's internal structure as one of their primary goals. NASA's MESSENGER mission has executed two flybys and will enter a highly elliptical orbit in 2011 (Solomon et al. 2007). The BepiColombo mission of the European and Japanese Space agencies (ESA and JAXA, respectively) will be launched in 2014, to reach Mercury in 2020 and put two spacecraft into orbit (Erd et al. 2004). Of interest here is the Mercury Planetary Orbiter (MPO), which will have a moderate elliptical polar orbit with 400 and 1,500 km minimum and maximum altitudes above Mercury's surface, respectively. Both missions carry laser altimeters. Because the MPO orbit allows measuring the topography of the entire surface, the BepiColombo mission is chosen for studying if time-dependent topography can be recovered from the altimeter data.

The BepiColombo Laser Altimeter (BELA) is designed to map Mercury's global topography with an accuracy of ≤ 10 m (Thomas et al. 2007). Its primary goal is to determine the global (static) topography, which in combination with the gravity field allows

inferring some aspects of the internal structure, e.g., crustal thickness variations. Superimposed on the static topography are the time-dependent tidal elevation changes with an amplitude of up to 1.5 m (e.g. Van Hoolst and Jacobs 2003). The longitudinal shift of the topography due to libration can also be treated as a time-dependent variation of topography. The determination of the libration amplitude and the tidal signal are primary science goals of BELA (Oberst 2007). Therefore, the goal of this study is to investigate to what accuracy the tidal Love number h_2 and the amplitude of forced libration Φ_{lib} can be extracted from synthetic BELA data.

A rather encouraging example for the recovery of a time-dependent signal of 1 m amplitude in the presence of much larger static topography is the determination of the seasonal variation of the CO₂-ice layer thickness in the North polar region of Mars, using the data of the MOLA laser altimeter on board the Mars Global Surveyor mission (Smith et al. 2001a). The variation is not determined point-by-point, but (in case of ice thickness) as an average for a given latitude like in the case of retrieving a tidal signal. While the ice thickness can be assumed to vary smoothly with latitude and time, the precise functional dependence is not known a priori. In contrast, the shape of the tidal deformation is given as function of location and time, and only its amplitude needs to be solved for. Therefore, recovering the tidal Love number h_2 should be possible with a higher precision than determining ice layer thickness variations.

This thesis is organised as follows. Firstly, an overview of the current scientific knowledge is given in ch. 2. Afterwards the generation of the synthetic topography of Mercury is described in more detail (ch. 3). Several approaches will then be presented for extracting the time-dependent parameters of the topography. For this purpose simulated height measurements are generated, and calculated for the nominal orbit of the MPO. The operational constraints of the BELA instrument are also taken into account. Furthermore, an error estimation for the extraction of the tidal Love number h_2 from observations at crossovers of the spacecraft ground tracks on the planetary surface is performed. If the spacecraft passes these points at times of different tidal phase angles, the tidal amplitude can be calculated from the difference of the topographic measurements at these points. The main uncertainties restricting the precision of these measurements are analyzed. However, the polar orbit of the MPO will produce very few crossovers at low latitudes, where the tides are largest, and the tracks will cross at very acute angles, which make this approach somewhat unattractive (ch. 6). Higher priority is given to simultaneous inversions of the static topography and the time-dependent variations of the topography. Two approaches are investigated. The first approach uses global basis functions for inverting the entire set of simulated measurements simultaneously for the global long-wavelength topography (represented by a spherical harmonic expansion), the tidal Love number, and the libration amplitude (ch. 4). The second approach uses local basis functions concentrated at the points of a rectangular grid to describe the static topography together with a global basis function that describes the time-dependent tidal elevation (ch. 5). At the end the final results are summarized, and an outlook for future work is given.

2 Introduction

An introduction to the scientific background, to the missions exploring Mercury, and the laser altimetry is given in the following sections.

2.1 Mercury

Mercury can only be seen in the twilight sky during dawn and dusk. Due to the tilt of its orbital plane with respect to the orbital plane of the Earth, Mercury's declination is sometimes lower than that of the Sun and sometimes larger. This limits the possibility for observing Mercury because it is not visible all the time. Furthermore, Mercury is "hurrying" along the sky because, as it is the inner-most planet of the solar system, it has an orbital period of only 88 Earth days. These two orbital peculiarities account for Mercury's elusiveness. Best observation conditions are in the equatorial region and at low latitudes of the Earth with dry climate and clear sky, respectively (Strom and Sprague 2003).

2.1.1 Mercury – mythology and first observations

The Northern cultures, such as Germans and Scandinavians, associated Mercury with their main deity, Wodan or Odin. These names are still in use and show the connection of the importance of Mercury for ancient cultures. "[...] *The connection lives on in our current use of English day of week Wednesday derived from "Wodan's day" and present-day Swedes and Danes use of "onsdag", directly derived from the old Norse "Odinsdag", and also in the French word "mercredi" coming from the Latin "Mercury dies". The ancient civilizations of the Middle East knew that the time between the reappearance of Mercury in the same configuration in the sky was shorter than for the other planets, and correctly reasoned that it, therefore, moved more rapidly. [...]*" (Strom and Sprague 2003). In 400 BC, Euxodus derived the time interval of 115 days between subsequent identical configurations in the morning or evening sky. Originally, Mercury was assumed to be an evening star, when observed with eastern elongation, and a morning star, when observed with western elongation (fig. 2.1, upper panel). Later it has been realized that it is the same star. Note, that elongation is the angular distance between a planet, here Mercury, and the Sun, seen from Earth. The largest angular distance between Mercury and the Sun, seen from Earth, is called greatest elongation (adopted from Strom and Sprague 2003).

In Mesopotamia, the first recorded observation was made on November 15th 265 BC. Mercury was named "Nebo" which was then used to denote geographical land forms (Mt. Nebo) and for certain people in the Old Testament. Mercury means passionate desire,

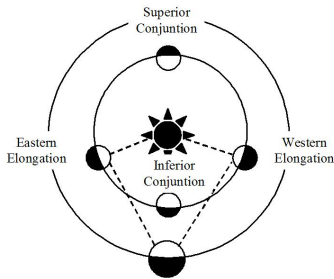


Figure 2.1: Left panel: Elongations and conjunctions of an inferior planet (planets interior to the orbit of Earth). If the inner planet (Venus or Mercury) is between Sun and Earth, it will be called inferior conjunction. In case the planet is on the far side of the Sun, it is called superior conjunction. The nodes of the orbital planes can sometimes be aligned. Then Mercury or Venus appear as dark spots crossing or transiting the Sun's disk (adopted from Strom and Sprague 2003). Right panel: Picture of Mercury, the ancient god at the Central Station, Mainz, Germany.

fertility, and rapid movement in original Greek dialects. Mercury was a Greek god, and even nowadays pictures can be found (fig. 2.1, lower panel, at the entrance of the central station in Mainz). The Greek god has the attributes of tireless, being a traveler, and the god of twilight (Strom and Sprague 2003).

With the invention of the telescope the modern era of astronomy started. The English scientist Thomas Harriot firstly used a telescope for observations in August 1609, and Galileo did so in the same year later. Mercury is an elusive object for observations, i.e. by telescope which were done by Galileo and Harriot, because its longitude in the sky never deviates more than 28 degrees from that of the Sun as seen from the Earth. As mentioned above, observations of Mercury are only possible in the twilight or during the day. Twilight has the great advantage that there is a good contrast for observations of the illuminated disk on the dark sky. However, disadvantage comes from the long optical path length in Earth's atmosphere which causes refractions. Additionally, atmospheric turbulence limits the observations. Observations at daytime have the advantage of shorter optical path lengths through the atmosphere, but the contrast of the illuminated disk to the sky is marginally small; Mercury is then hard to find. Computational tracking makes it somewhat easier to find and track Mercury. Mercury is only visible during about thirty or forty days a year. Mercury has different phases during which different fractions of its illuminated disk can be seen from Earth. This phenomenon is similar to the Moon phases. When Mercury has a crescent phase it is even more difficult to find it on the sky.

Mercury is in a 3 : 2 resonance between its orbital and rotational motion. One side-real period lasts approximately 87.969 Earth days, while Mercury's rotation period is two-thirds of that, approximately 58.64 days. Balogh et al. (2002), Murray and Dermott (1999), Strom and Sprague (2003) and Wieczorek (2007) give a more detailed overview of the rotational states of Mercury. The rotational resonance is related to the Mercury's

eccentric orbit around the Sun. Optimum observation conditions repeat after approximately three synodic periods. However, after that time period, one always observes the same part of the surface again. This is the reason for the original assumption that Mercury has a bound rotation with the Earth and, therefore, always faces the same side to Earth as does the Moon. Using the Arecibo radar facility in Puerto Rico, Gordon Pettengill and Rolf Buchanan Dyce discovered in 1965 that Mercury has an eigenrotation with a period of around 58 days. "[...] *The finding of a value for the rotational period of Mercury which differs from the orbital period is unexpected and has interesting theoretical implications [...]*" (Pettengill and Dyce 1965). Astronomers could significantly improve their Earth-based investigations in the last decades due to the availability of CCD sensors. Furthermore, with imaging radio interferometry the rotational states and libration amplitudes of Mercury could be retrieved.

Naturally, most detailed information can be retrieved by orbiting Mercury with a spacecraft. One mission, Mariner 10 by NASA, has already investigated Mercury, NASA's MESSENGER spacecraft is currently on its way to Mercury and will be in orbit in 2011, and ESA plans to arrive at Mercury in 2020 with its BepiColombo mission. An overview of these missions is given in sec. 2.2.

Mercury is mostly observed and investigated by ground-based radar observations from which rotational parameters can be determined. Margot et al. (2007) observed the forced libration amplitude (sec. 2.4.2) of Mercury. This technique is generally used for creating maps of the surface reflectivity and the surface texture, because some fraction of the transmitted electromagnetic wave is absorbed. It also allows putting constraints on the chemical composition of the surface. Another technique widely used for observing Mercury is interferometry with different telescopes that observe the same body at the same time to achieve a better angular resolution.

2.1.2 Mercury – the planet, surface and parameters

Mariner 10 (sec. 2.2.1) mapped approximately 45 % of Mercury's surface. Characteristic features of Mercury's topography are plains such as the Tolstoj-basin shown in fig. 2.2, right panel. The pictures showed large plains and a heavily cratered surface indicating that Mercury's surface is geologically old. Half of the surface of Mercury viewed by Mariner 10 shows intercrater plains which must be the result of the time of the heavy bombardment. Furthermore, the whole surface shows scarps. These scarps are assumed to be the result of the shrinking of Mercury during its thermal evolution. Mercury's radius probably has decreased by 3-4 km since formation of the planet. A scarp seen by Mariner 10 is shown in fig. 2.2, left panel. Strom and Sprague (2003) and Zuber et al. (2007) describe in more detail the geological history of Mercury. Furthermore, Mercury has irregularly formed hills up to 1 km altitude within the plains. These hills are assumed to be the result of a large impact. Laser altimetry and stereo imaging can answer how these hills are formed and allow putting constraints on the time of heavy bombardment at the end of the planetary formation process.

The topography of terrestrial planetary bodies is usually dominated by features such as craters and slopes. Mercury is the terrestrial planet in the solar system for which the topography is least studied. Considerably more information is available for the Moon and for Mars. In the past decade, Mars has been mapped by the Mars Orbiter Laser Al-

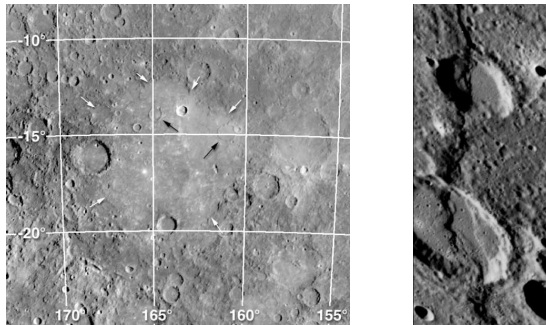


Figure 2.2: Left panel: Smooth plains fill the center of the 510-km-diameter Tolstoj Basin (unit boundaries shown as white arrows) and partially fill smaller craters (black arrows) on the basin floor. These superposition relationships indicate that this region of smooth plains cannot be impact melt generated at the time of formation of the Tolstoj Basin. The image is a portion of a hemispheric mosaic with a resolution of 1 km/pixel (Solomon et al. 2001). Right panel: A Mariner 10 image of Discovery Rupes, one of the longest and most prominent scarps imaged by Mariner 10 with a resolution of 240 m/pixel (Solomon et al. 2001).

timeter (MOLA) which is briefly described in sec. 2.3.3. Aharonson et al. (1998, 2001) have analyzed MOLA data in more detail to derive the slope distribution and topography properties for Mars, while McEwen and Robinson (1997) have thoroughly evaluated mapping data taken during the Clementine mission to the Moon. Kreslavsky and Head (1999, 2003) identify the difference in geological properties of the Northern and Southern hemisphere of Mars and show that different kinds of geological features of Mars have typical kilometer-scale slopes. Based on current knowledge, Kreslavsky et al. (2008) compare the different surfaces of terrestrial planets and find that Mercury is similar to the Southern hemisphere of Mars and not very different from the Moon's topography. Further investigations and comparisons for the terrestrial planets are performed by Rummel (2005). Smith et al. (1998, 1999, 2001a) and Zuber et al. (1992) have analyzed the Martian topography as well. Helfenstein and Shepard (1999) have studied the topography of the Moon for very short wavelengths in the sub-millimeter range and its relations to the Lunar Regolith.

Mercury's surface is heavily cratered indicating that the surface is geologically very old similar to the Southern highlands of Mars. Aharonson et al. (2001) have analyzed the spatial frequency distribution of the surface topography of Mars using MOLA data. The resulting power spectral density is shown in fig. 2.3 for two typical areas of Mars. Region B belongs to the Northern hemisphere and is geologically young, while Region A belongs to the Southern hemisphere and is geologically old and heavily cratered. Figure 2.3 shows the power spectrum which is used for the synthesis of the yet unknown Hermean topography in the simulations presented in sec. 3. This hypothetical topography has a degree power following a power law with an exponent (β in fig. 2.3) of -2 and resembles the lunar topography at large scales.

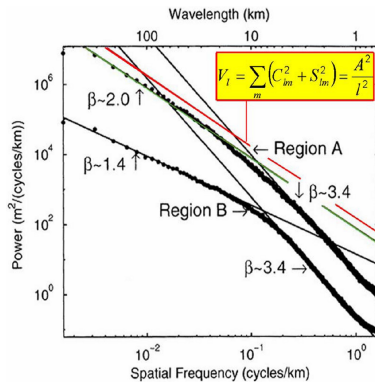


Figure 2.3: Power spectral density of the topography of two types of regions on the Martian surface (Aharonson et al. 2001). Region A belongs to the Southern hemisphere, which is geologically old and heavily cratered. Region B belongs to the Northern hemisphere which is geologically young. The topography is described as a power law with an exponent of β . For comparison, the power spectral density corresponding to the degree power V_l of the spherical harmonic expansion which is used in the simulations by Koch et al. (2008, 2009a) is shown as red line.

Astronomical observations revealed that Mercury is a spherical body with marginally small differences between the mean equatorial and polar radius. Mercury is assumed to be a sphere in the simulations, as the polar and equatorial radius is nearly identical. Furthermore, the angular deviation between Mercury's rotational and figure axis is marginally small. This effect has an important role for the time-dependent parameters of the topography which will be discussed in sec. 2.4. With more than 250,000 years, Mercury's precession is quite long (e.g. Bois and Rambaux 2007, Peale 2005) as compared to the Earth where the precession period is roughly 25,600 years.

As Mercury is the innermost planet of the solar system, it is a planet of extremes. Temperature gradients on the surface are quite large. The lowest approximated temperature is 100 K (-173 °C) during night in Mercury's apohel. The maximum temperature of about 700 K (+427 °C) is reached on parts of the surface directly pointing to the Sun in Mercury's perihel. The mean temperature is 440 K (+167 °C). Due to Mercury's resonant orbit, the areas of largest temperature gradient can easily be determined. The large temperature gradients have also implications for the design of space instrumentation on spacecraft orbiting Mercury. Instruments have to operate in a large temperature range if not controlled within a specific temperature range by external heating and cooling systems. Table 2.1 lists the parameters of Mercury which are needed and used for the simulations. The planetary radius is only 40 % of Earth's planetary radius.

Another extreme is Mercury's density. Mercury has a mean density of 5.3 g/cm³. This is an unusually large uncompressed density. When the uncompressed densities of the terrestrial planets and the Moon are plotted versus the planetary diameter, the densities fit in a line except for that of Mercury. This can be explained by a large content of

Table 2.1: Mercury parameters

Parameter	Symbol	Value
Mass ratio	$M_{\text{Sun}}/M_{\text{Merc}}$	6023700.0
Mean radius	a	2439.7 km
Distance Mercury to Sun	R	57.909×10^6 km
Eccentricity	e	0.20563
Orbital period	T_{Merc}	87.969 days

heavy elements such as iron. The geophysics of Mercury are analyzed in more detail by Anderson et al. (1987) and Zuber et al. (2007). Furthermore, the existence of a magnetic field suggests that Mercury has a liquid outer core. Mercury is assumed to have a large inner, solid core and small liquid outer core shell. Due to Mercury's large density, the core is assumed to be made of nearly pure iron with a marginal amount of light elements; the most promising candidate is sulfur. The core size is derived to be approximately 75 % of the planetary radius, i.e. about 1800 km. Around 70 % of the planetary mass is concentrated in the core. While the mantle of the Earth has 62 % of the planetary mass, for Mercury this part is only around 30 %. The mantle of Mercury has a thickness of about 600 km, and the crust has a thickness of only about 10 km. A better understanding of the interior structure of Mercury will be retrieved by the space missions MESSENGER (sec. 2.2.2) and BepiColombo (sec. 2.2.3). These missions will probably reveal why Mercury has such an unusually large amount of iron. The actual models for the origin of the large iron amount are not discussed, as they are beyond the scope of this work. Section 2.1.3 briefly describes the importance of a differentiated core into an inner solid and outer liquid part for generating Mercury's weak magnetic field.

Mercury's orbital plane is inclined by 7 degrees with respect to the ecliptic plane of the Earth. Mercury's perihel is at about ≈ 0.307 Astronomical Units (AU), and apohel ≈ 0.467 AU (e.g. Balogh et al. 2002, Strom and Sprague 2003). Mercury has a mean orbital velocity of 47.87 km/s. Mercury's rotation axis and figure axis are nearly parallel. Therefore, there are craters in the Polar Region which are in shade. There, the probability of detecting water ice is high. This shall be investigated by MESSENGER (sec. 2.2.2) and BepiColombo (sec. 2.2.3). Water ice in these craters probably dates back to the time of planet formation. If its composition could be determined, it would allow a more detailed investigation of the planet formation processes.

Mercury has an exosphere, which is not yet investigated in detail. This is a primary goal of the MESSENGER (sec. 2.2.2) and BepiColombo missions (sec. 2.2.3). The main constituents of the exosphere are hydrogen (22 %) and helium (6 %) which probably originate from the solar wind. Oxygen (42 %), sodium (29 %) and potassium (0.5 %) originate from Mercury's surface. The mean pressure of the exosphere is derived to be $\approx 10^{-15}$ bar. This means that Mercury's atmosphere has a mass of only 1000 kg. This is marginally small compared to the whole planet's mass.

2.1.3 Mercury – the interior structure

During its first flyby, Mariner 10 surprisingly detected a magnetic field which was investigated in more detail during its third flyby (sec. 2.2.1). The presence of the magnetic field may either be based on the external magnetic field generated by the Sun or on an internal dynamo. The strength of Mercury's magnetic field is only about 1 % of that of the Earth's magnetic field. The main result of Mariner 10's third flyby was that the magnetic field must be of internal origin. The magnetic field is explained, e.g. in Connerney and Ness (1988), Ness (1979) and Strom and Sprague (2003). The magnetic field is strong enough to form a bow-shock wave which deflects the solar wind, and is assumed to be stable. It was shown that Mercury has a dipolar field which is inclined by (14.5 ± 5) degrees from the rotation axis, similar to the Earth's magnetic field, i.e. Ness (1979). The equatorial field intensity is (330 ± 18) nT, with an equivalent dipole moment of (4.8×10^{22}) gauss cm^3 .

Margot et al. (2007) have found evidence that Mercury must have a molten outer core by observing Mercury's longitude libration (sec. 2.4.2) with ground-based radar interferometry. Rambaux et al. (2007) present a theoretical approach to the relation between the strength of core-mantle coupling and the libration amplitude of Mercury. Peale (1972, 1976a,b) has already hypothesized that Mercury must have a molten core by using observations made by Mariner 10.

The magnetic field of Mercury cannot entirely be induced by an interplanetary magnetic field generated by the Sun. Mercury's inner solid core presumably has a radius of approximately 70 % of the planetary radius, and it is presumably surrounded by a thin liquid layer. The thin liquid layer is the source of the weak magnetic field of Mercury. Due to its high density, Mercury has to have a solid inner core mainly consisting of iron. Lighter elements have then to be present in the outer liquid core so that a weak magnetic field can be generated by a dynamo driven by chemical convection. Current models on Mercury's interior have the outer core's sulfur content as crucial parameter for starting a dynamo (Harder and Schubert 2001). Several scientific groups explain the existence of the magnetic field by the presence of a dynamo generating the magnetic field in the outer core of the planet. Breuer et al. (2007) and Wicht et al. (2007) give comprehensive reviews of the current dynamo models that explain the observed strength of the dipolar magnetic field of Mercury. Spohn et al. (2001) summarize how Mercury is differentiated and what can be retrieved by the BepiColombo mission (sec. 2.2.3). Simulations by Christensen (2006) demonstrate that the magnetic field can be generated by a deep dynamo. Christensen and Wicht (2008) show that the magnetic field of Mercury can even be generated in cores which are partly stable.

The inner core radius can be derived from radio Doppler tracking data. Yoder et al. (2003) use this approach for determining the core radius of Mars to (1680 ± 160) km. Hauck et al. (2004) explains the internal and tectonic evolution of Mercury.

2.2 Missions for exploring Mercury

Mercury has yet only been visited by one satellite mission – Mariner 10 in 1974/1975. MESSENGER is currently on its way to Mercury and will be in orbit around Mercury

in 2011. It lasted more than 30 years for setting-up missions to Mercury again, as it is hard to reach Mercury and high technical efforts are needed for observing Mercury from orbit. BepiColombo will additionally investigate Mercury. Launch is planned for 2014. In the following all these missions will be described with emphasis on the BepiColombo mission. A comprehensive overview of all missions is given by Balogh (2007).

2.2.1 Mariner10

Mariner 10 was the first mission to visit Mercury. It also was the first mission to use a gravitational field of a planet (gravity assist at Venus) to reach a planetary body far from Earth with limited fuel reserves. In 1970 and 1973 there were optimums conditions for using a gravity assist to reach Mercury with the least amount of energy. The National Aeronautics and Space Administration (NASA) designed a mission to Mercury using a concept for the satellite which was previously used for other missions, *Mariner*. As it was the 10th Mariner satellite, the mission was named Mariner 10. Guiseppe Colombo (fig. 2.4, right panel) pointed out that Mariner 10 can pass by Mercury two or three times before the fuel runs out. NASA took his remark and launched Mariner 10 within the time window which allowed to use a gravity assist and to reach Mercury with a cruise time of less than 1 year.

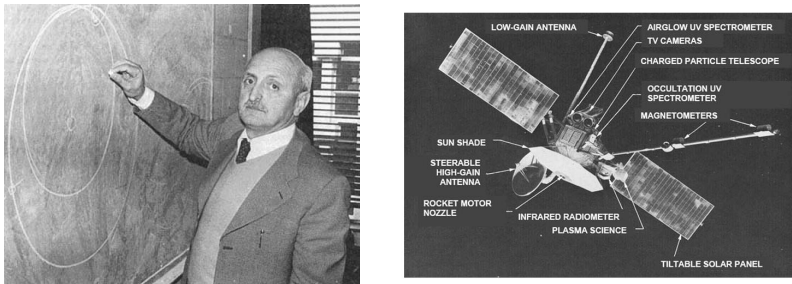


Figure 2.4: Left panel: Guiseppe Colombo (1920-1984), Italian scientist, who advised NASA to achieve three flybys of Mercury by Mariner 10. ESA and JAXA's joint two-spacecraft mission is named in his memory (Balogh 2007). Right panel: The Mariner 10 spacecraft and its scientific payload (Balogh 2007).

Mariner 10 carried several scientific instruments to observe Venus during the gravity assist. The payload included seven instruments: television imaging, infrared radiometry, ultraviolet spectroscopy, magnetic fields, plasma science, charged particles, and radio science (fig. 2.4, left panel).

During its first flyby, Mariner 10 observed a weak planetary magnetic field. After this surprise, it was decided to further map Mercury's surface only during its second flyby, while the origin of the magnetic field should be investigated in more detail during the third flyby.

2.2.2 MESSENGER

NASA also set up the second mission to Mercury. MESSENGER (MErcury Surface, Space ENvironment, GEochemistry and Ranging) was launched in August 3rd 2004. The spacecraft will be inserted into orbit around Mercury in 2011. The main goals of MESSENGER are the more detailed investigation of the planetary surface and Mercury's magnetic field and its interaction with its exosphere. Domingue and Russell (2008) and Gold et al. (2001) give an overview of the scientific objectives of the MESSENGER mission. The instruments adopted to the spacecraft are listed in tab. 2.2. MESSENGER is in a elliptical orbit with a periapsis altitude of around 60 degrees. The orbit will have an eccentricity of 0.7396 (Domingue and Russell 2008, Santo et al. 2001, Solomon et al. 2007). The orbit of MESSENGER is shown in fig. 2.5 (right panel) and the spacecraft and its instrumentation itself in fig. 2.5 (left panel).

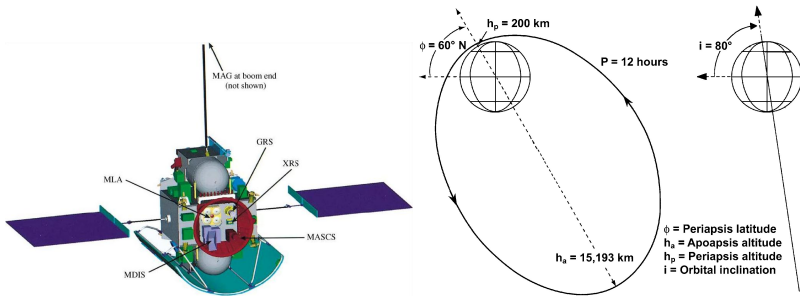


Figure 2.5: Left panel: MESSENGER spacecraft showing instrument accommodation (Gold et al. 2001); right panel: the operational orbit of MESSENGER (Balogh 2007).

The orbit is chosen to be highly elliptical to investigate Mercury's magnetosphere. Investigations of a planetary magnetosphere involve the visit of different regions of the magnetosphere at different distances to the planet in order to understand the full structure of the magnetic field and plasma flow. First results from the first flyby of MESSENGER in January 2008 are reported by Zuber et al. (2008). MESSENGER is set-up to map the Northern hemisphere by imaging and altimetry, as Mariner 10 already mapped the Southern hemisphere of Mercury. The MESSENGER laser altimeter (MLA) is described in more detail in sec. 2.3.4. The MLA instrument shall determine the libration amplitude. Together with the gravity field measurements this will lead to a better understanding of Mercury's interior structure. From this knowledge, models of the generation of Mercury's magnetic field (Christensen 2006, Christensen and Wicht 2008) can be tested (sec. 2.1.3).

2.2.3 BepiColombo

The European Space Agency (ESA) and Japanese Aerospace Exploration Agency (JAXA) are also setting-up a mission to Mercury. Erd et al. (2004) describe the whole mission in detail, while here only the main goals and features of the mission are briefly described.

Table 2.2: Scientific payload of MESSENGER

Abbreviation	Instrument
MDIS	Dual imagers, narrow and wide angle FOV
GRNS	Gamma-Ray and Neutron Spectrometer
XRS	X-ray spectrometer, 1-10 keV
MAG	Fluxgate magnetometer +3.6 m boom
MLA	Laser altimeter, 1,200 km range
MASCS	UV/Visible spectrometer, visible/IR spectrograph
EPPS	Energetic particle spectrometer, fast imaging plasma spectrometer
DPU	Integrated electronics, power processing for instruments, MDIS electronics

The mission is named after the famous Italian scientist Bepi Colombo (fig. 2.4, left panel). It will be launched with an Ariane 5 rocket to take the payload into space in 2014 and will reach Mercury in 2020 after a six-year cruise. BepiColombo will investigate the following topics

- Mercury as a planet (form, *interior*, *geology*, composition),
- Origin of its magnetic field,
- Exosphere (composition and dynamics),
- Magnetosphere (structure, dynamics, interaction with the planet),
- Relativity and Gravitational physics.

The science topics of the BepiColombo laser altimeter (BELA) are set in *Italic style*.

Testing Einstein's theory of General Relativity seems promising as Mercury is close to the Sun which contains the vast majority of mass of the solar system. One of the classical tests is the measurement of the perihelion shift of Mercury which is already proven, but higher accuracy is required to test alternative theories to Einstein's theory of General Relativity. In fig. 2.6 the planned cruise for BepiColombo to Mercury is sketched. Figure fig. 2.7 (left panel) shows the spacecraft of the BepiColombo mission on its cruise to Mercury how it presumably will look like.

BepiColombo includes two spacecraft, the Mercury Magnetospheric Orbiter (MMO) set up by JAXA and the Mercury Planetary Orbiter (MPO) set-up by ESA. MMO's orbit has peri- and apoherm distances of 400 – 16,000 km, respectively, while these distances are 400 km and 1,500 km, respectively, for MPO's orbit. The two spacecraft have a 4 : 1 resonance between their orbits which are sketched in fig. 2.7 (right panel). MMO will investigate the magnetosphere. In combination with observations of MESSENGER (sec. 2.2.2) a better understanding of the magnetosphere of Mercury and its interaction with the solar wind will be achieved.

MPO is described in more detail, as the laser altimeter is adapted to this spacecraft. The payload of both spacecraft are listed in tab. 2.3. On MMO five instruments will be installed, while MPO is much larger and includes nine instruments. The radio science

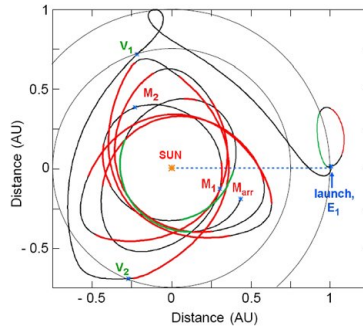


Figure 2.6: The cruise trajectory of BepiColombo in an elliptic projection, in a coordinate system with the Sun-Earth line fixed. The gravity-assist flyby encounters with the Earth (E_1), Venus (V_1 and V_2), and Mercury (M_1 and M_2) are indicated as is the final arrival to Mercury (M_{arr}). Solar electric propulsion (SEP) thrust arcs are shown in red and green; coasting arcs are shown in black (Balogh 2007).

experiment (MORE, Milani et al., 2001), the camera (SIMBIO-SYS, Capaccioni et al., 2005), and the laser altimeter (BELA, Thomas et al., 2007) are of main interest here, where BELA is described in more detail in sec. 2.3.5.

Table 2.3: Scientific payload of BepiColombo

S/C	Abbreviation	Instrument
MPO	BELA	Laser Altimeter
	ISA	Radio Science: Accelerometer
	MERMAG	Magnetometer
	MERTIS	Gamma Ray and Neutron Spectrometer
	MGNS	X-ray Spectrometer and Solar Monitor
	MORE	Radio Science: Ka-band Transponder
	PHEBUS	UV Spectrometer
	SERENA	Neutral Particle Analyser / Ion Spectrometer
	SIMBIO-SYS	High Resolution and stereo cameras / Visual and NIR Spectrometer
MMO	MGF	Magnetic Field Investigation
	MPPE	Mercury Plasma Particle Investigation
	PWI	Plasma Wave Investigation
	MSASI	Mercury Sodium Atmosphere Spectral Imager
	MDM	Mercury Dust Monitor

A precise extraction of the static and the time-dependent topography requires knowledge of the spacecraft position from the radio science experiment MORE with a precision of about 10 cm. This high precision will probably be achieved by the radio science exper-

iment (MORE) and the Italian spring accelerometer (ISA) onboard the spacecraft (Lucchesi and Iafolla 2006, Milani et al. 2001). The radio science experiment (MORE) will use two different wavelengths for increasing the precision. Joint analyses of SIMBIO-SYS and BELA data sets will further improve the understanding of Mercury’s topography. MPO is in a slightly elliptical orbit with an eccentricity of 0.162, and needs approximately 2.3 hours for completing one orbit. The orbit is a nominally polar one. Due to the non-spherical gravity field of Mercury the orbital parameters will slightly vary. An orbit with 89.9 degrees inclination is assumed.

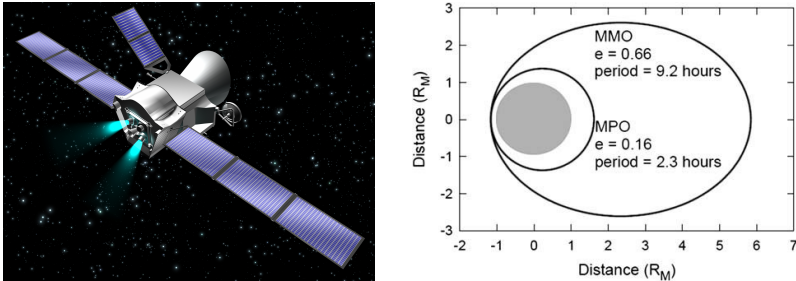


Figure 2.7: Left panel: BepiColombo spacecraft (credits to ESA); right panel: the operational orbits of the Mercury Planetary and Magnetospheric Orbiter (Balogh 2007).

Mercury’s rotational period and the chosen MPO orbit define the separation between the satellite ground tracks. This limits the precision of the extraction of the topography, especially in the equatorial region. For the nominal mission duration of 1 Earth year (approximately 4 Mercury years) and approximately 910 MPO orbits within 1 Mercury year gives a separation of the tracks of approximately 2 km in the equatorial region. This limits the resolution of the surface map as discussed in ch. 5. The surface will always be mapped with high accuracy along the laser tracks in latitudinal direction. The spacing of laser shots is of order 0.3 km for a repetition frequency of 5 Hz of the laser.

2.3 Laser altimetry

Laser altimetry is a specific observation technique for point measurements of the topography of a surface. It is a well known tool for mapping the global topography of a planet, and already had large impact on planetary science.

2.3.1 Introduction to laser altimetry

Laser altimetry uses visible light or near-infrared radiation, and is based on a time measurement. A laser pulse is transmitted from the spacecraft to the planetary surface. A small fraction of the laser light scattered by the planetary surface is transmitted back to a detector on board the spacecraft. The time difference between transmission of the laser pulse and detection of the returned fraction of light, Δt , is measured. The topographic

height T at the laser shot can then be determined to

$$T = R_{SC} - r - c \frac{\Delta t}{2}, \quad (2.1)$$

where c is the speed of light, and R_{SC} the radial distance of the spacecraft from the center of mass of the planet. The radius r is the radius of a reference body for the planet, which is here chosen as a sphere. Equation (2.1) assumes that the instrument points nadir. This is the simplest case for the determination of topographic height. The observation principle is schematically shown in fig. 2.8. Gardner (1982, 1992) analyses in detail the effect of specific instrumental uncertainties, e.g. beam divergence of the laser, off-nadir angle of the instrument, or the surface slope within the laser foot print of which the size mainly depends on the beam divergence and the spacecraft altitude. He summarizes the effect for each of the limiting parameters on the laser pulse propagation time and on the width of the returned pulse. Furthermore, he gives simplifications for the equations from which the propagation time and its uncertainty are calculated. It turns out that the surface slope and the beam divergence usually have the largest effect on the uncertainty distribution. Another important limitation is usually also given by the timing resolution of the receiver or by the initial pulse length of the laser shot. An uncertainty in the receiver timing of in the centroid of the initial laser pulse of 1 ns corresponds to an uncertainty of 30 cm in the altitude measurement.

The analysis of the measurements needs the accurate knowledge of the spacecraft position. The position of the spacecraft is determined by radio tracking experiments, while stellar cameras are used for the exact orientation within the celestial reference frame and for the pointing adjustment of the instruments. Montenbruck and Gill (2005) give an overview on this topic. The orbit and pointing of the spacecraft are affected by the gravity field of the central planetary body and by the solar gravity field. Additionally, the solar radiation pressure can be important, as well as the atmospheric drag, although not in the case of an orbit around Mercury.

Most laser altimeters (LA) operate either at a wavelength of 532 nm, of 1064 nm or of 1500 nm. This specific wavelength is given by the most commonly used laser-active crystal, the Nd:YAG crystal. The wavelength of 1064 nm is well applicable because there are no prominent absorption features in this wavelength. In particular, it works in the Earth's atmosphere and allows mapping of the surface depending on the amount of water in the atmosphere. Observations can in principle be made in all wavelengths. Radar is often used for Earth observations due to the Earth's atmosphere absorption window in the near-infrared.

Laser altimeter data significantly depend on the slope and roughness of the analyzed terrain. The shape of the returned optical pulse varies due to the different topographic features and is additionally a function of the used wavelength. The returned signal is large in the case of observing water or an ice sheet, for which the specular surface reflectivity is largest. Generally, some fraction of laser light is absorbed, some fraction is reflected specularly, and some fraction is reflected diffusively.

In general, the best orbit to be chosen for a laser altimeter experiment is a circular one. Then, the quality of the returned signal does not vary much for different measurement locations. MESSENGER (sec. 2.2.2) and BepiColombo (sec. 2.2.3), however, are in elliptical orbits around Mercury. This directly results in a measurement uncertainty that

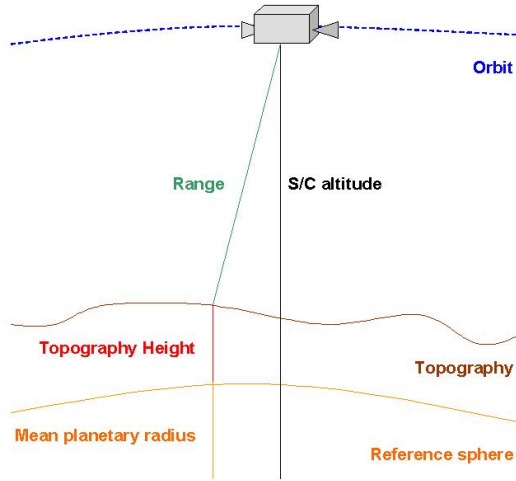


Figure 2.8: Scheme of laser altimeter measurements. The mean planetary radius and the reference sphere are shown in orange, the orbit of the spacecraft in blue, the spacecraft altitude above the center of mass in black, the surface topography in brown, the observation or range in green, and the unknown topographic altitude above the mean planetary radius in red.

is unevenly distributed over the planetary surface. Parts of the surface are more densely covered with measurements, but these measurements have larger uncertainty because the spacecraft is at higher altitude, while some parts are less densely covered with laser shots, but these measurements have higher precision. The analysis of the data sets which are generated in the course of a mission and the results being retrieved from them very much depend on the chosen orbit.

Laser altimetry has already been used quite often in Earth observation, while it is a rather new technique in planetary science. In the following two laser altimeters will be briefly described, where one mapped the Earth and one Mars. The MOLA laser altimeter has already returned results with very high quality from Mars. Figure 2.9 shows the global topography of Mars as accurately mapped by MOLA. Together with the Geoscience Laser Altimeter System GLAS, MOLA provides the basis for the laser altimeters which are either sent or planned to be sent to Mercury. These laser altimeters are described below, where the BepiColombo laser altimeter is described in more detail.

2.3.2 Geoscience Laser Altimeter System (GLAS)

The Geoscience Laser Altimeter System (GLAS) is one of the instruments of the ICESat mission to investigate ice elevation changes which indicate variations of the ice volume

(mass volume). ICESat was launched in January 2003 and is in a circular orbit 600 km above Earth's surface. Abshire et al. (1998) give a general overview about GLAS, while the data analysis procedure for the derivation of a topographic measurement from a single laser shot is described by Brenner et al. (2003). This analysis mainly concentrates on the derivation of the elevation and the slope of the surface. Phillips et al. (1999) made first investigations for correcting the laser altimeter record for tidal variations of the ocean. The laser altimeter data record of GLAS has additionally to be corrected for the atmospheric delay, which has been investigated in more detail by Herring and Quinn (1999).

Table 2.4: Laser altimeter instrument parameters

Parameter	GLAS	MOLA	MLA	BELA
	<i>S/C</i>			
Destination	Earth	Mars	Mercury	
Altitude [km]	600	400	200–15,000	400–1500
Pointing uncertainty [μ rad]	6		15	25
	<i>Laser transmitter</i>			
Pulse energy [mJ]	70-80	42	20	50
Pulse width [ns]	2.5	3.4	2.5	3.4
Wavelength [nm]			1064	
$1/e^2$ beam divergence [μ rad]	54	185	40	25
Repetition rate [Hz]	40	10	8	10
	<i>Receiver optics</i>			
Aperture radius [mm]	500	250	53×4	125
Focal length [mm]		740	1750	1250
Field of view [μ rad]		425	200	200

GLAS operates in the 1064 nm wavelength, but it has the possibility to also measure at a wavelength of 532 nm. Until March 2009, GLAS made more than 1,000,000,000 observations. The main instrumental parameters are listed in tab. 2.4. The accuracy of each laser shot is less than 15 cm. GLAS was important for the setting-up of the laser altimeters described below. The main scientific objective of GLAS is the exploration of the cyrosphere: a) the determination of the mass balance of the polar ice sheets and their contribution to the global sea level changes, and b) to obtain a data set for further predictions of the sea level changes. Furthermore, GLAS investigates the atmosphere and the land areas. In this respect, the scientific objectives are: a) to measure cloud heights and to extract vertical profiles of the clouds, b) to map the solid surface topography, and c) to obtain data of the surface roughness, vegetation heights, snow-cover, and sea-ice surface characteristics. Brenner et al. (2003) give a more detailed overview. GLAS was a very important precursor project where most of the analysis techniques were developed in detail. These techniques can be applied to altimetry in space.

2.3.3 Mars Orbiter Laser Altimeter (MOLA)

The Mars Orbiter Laser Altimeter (MOLA) was included to the scientific payload of the spacecraft of the Mars Global Surveyor (MGS) mission which was launched November 7th 1996, and observed Mars from September 1998 to November 2006, when the communication with the satellite broke down. The design of the laser altimeter is described in detail by Afzal (1994). The instrument transmits laser pulses with 1064 nm wavelength. A more detailed summary of the instrumental parameters in comparison with the other presented laser altimeters is given in tab. 2.4.

The main goal of MOLA is to map the surface of Mars for a better understanding of its geology, geophysics, and atmospheric circulations. The laser altimeter has a relative uncertainty of approximately 30 cm for a single laser shot. Figure 2.9 shows a global map of Mars retrieved after analyzing the laser altimeter data set. The observation of the reflection within the Martian atmosphere was a secondary goal of the mission and the instrument.

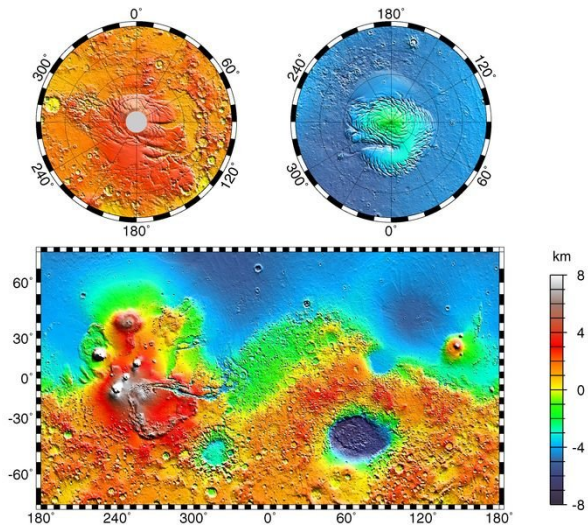


Figure 2.9: Maps of Mars' global topography. The projections are Mercator to 70 degrees latitude and stereographic at the poles with the South pole at left and North pole at right. Note the elevation difference between the Northern and Southern hemispheres. The Tharsis volcano-tectonic province is centered near the equator in the longitude range 220 degrees E to 300 degrees E and contains the vast east-west trending Valles Marineris canyon system and several major volcanic shields including Olympus Mons (18 degrees N, 225 degrees E), Alba Patera (42 degrees N, 252 degrees E), Ascraeus Mons (12 degrees N, 248 degrees E), Pavonis Mons (0 degree, 247 degrees E), and Arsia Mons (9 degrees S, 239 degrees E). Here an areocentric coordinate convention with east longitude positive is used (taken from www.wikipedia.de).

The analysis of the MOLA data was mainly carried out by using interpolation techniques described by Abramov and McEwen (2004) and Neumann (2001). The characteristics of the Martian topography are not evenly distributed over the surface. The Northern hemisphere is geologically young compared to the Southern hemisphere. Aharonson et al. (2001, 1998), Kreslavsky and Head (1999, 2003) and Smith et al. (1998) investigated the surface slope and elevation distribution of the Martian topography in detail. They found that the power spectral density of the topography follows a power law where the Northern and Southern hemisphere have to be described by different laws (Aharonson et al. (2001) and fig. 2.3). Smith et al. (1999, 2001b) presented the results which were retrieved by analyzing the MOLA data. Neumann et al. (2004) additionally investigated the crustal structure of Mars by using the laser altimeter observations and gravity data of Mars. MOLA was adopted for the environment of Mercury and then launched as MLA for investigating Mercury.

2.3.4 Mercury Laser Altimeter (MLA)

The Mercury Laser Altimeter (MLA) is included in the scientific payload of the MESSENGER mission (sec. 2.2.2) for exploring Mercury. MLA operates at 1064 nm wavelength. The first flyby in January 2008 gave first results which were published by Solomon et al. (2008) and Zuber et al. (2008). Cavanaugh et al. (2007) and Krebs et al. (2005) describe the instrumental properties in more detail. The most important properties related to the transmitter and receiver and the spacecraft itself are listed in tab. 2.4.

MLA is designed to map the topography up to spacecraft altitudes of 1000 km above the mean surface. The MESSENGER spacecraft is in a highly elliptical orbit around Mercury. With the chosen orbit which has an argument of periapsis which is close to the North pole, MLA will only map the Northern hemisphere. However, in combination with the data of the camera of the spacecraft and the picture data of the Mariner 10 mission (sec. 2.2.1) a global topographic map of Mercury will be retrieved. Due to the high density of laser data records along the orbit tracks of MESSENGER, craters can be analyzed in more detail. Furthermore, the altimeter shall investigate the time-dependent variations, described as forced libration amplitude (sec. 2.4.2). The combination with the data of the magnetometer shall provide an explanation for the magnetic field generation on Mercury.

MLA shall also support a more precise extraction of the topographic features. In combination with stereo imaging and radio occultation, their shape shall be retrieved. Analyzing the whole data set shall also give an answer to the question whether the complete surface of Mercury is heavily cratered as observed by Mariner 10, and whether the "scarps" are a local or global feature on Mercury.

2.3.5 BepiColombo Laser Altimeter (BELA)

The BepiColombo Laser Altimeter (BELA) is one of the main instruments of the Mercury Planetary Orbiter (MPO) in the frame of the BepiColombo mission (sec. 2.2.3) exploring Mercury. BELA is built by a cooperation project of the German Space Agency (DLR), the University of Bern (UBE), the Instituto de Astrofísica de Andalucía (IAA), industrial partners, and the Max-Planck-Institut für Sonnensystemforschung (MPS).

The main scientific objectives of BELA are the extraction of the long-wavelength topography, the generation of Digital Terrain Models (DTM) for special regions, deriving the shape of Mercury expressed as an ellipsoid, the extraction of the time-dependent variations of the topography expressed as tidal Love number h_2 (sec. 2.4.1) and forced libration amplitude Φ_{lib} (sec. 2.4.2). Oberst (2007) summarizes all scientific goals. Only the primary goals of the mission are listed here. The BELA data can be analyzed together with observations of the radio science experiment (MORE, Milani et al., 2001) to correlate the long-wavelength topography and gravity field.

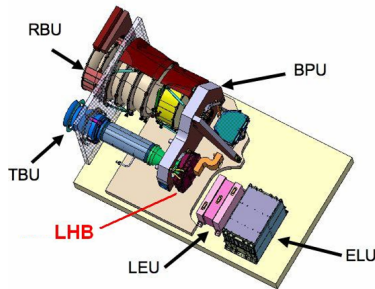


Figure 2.10: Scheme of BELA containing labels of the different units of the instrument: RBU (Receiver Baffle Unit), TBU (Transmitter Baffle Unit), LHB (Laser Head Box), LEU (Laser Electronics Unit), BPU (Base Plate Unit), and ELU (ELectronics Unit).

BELA is designed to have a relative range uncertainty of 1 m (e.g. Gunderson et al. 2006). Gunderson et al. (2006) have modeled the link budget of BELA and have found that the receiver will be sufficiently sensitive to detect enough return photons up to a spacecraft altitude of up to 1000 km. If the argument of periapsis is at the equator, this will result in a double coverage of the Polar Regions. First investigations showed that the argument of periapsis will change. The amount depends on the gravity field coefficient C_{22} . The argument of periapsis will probably change up to 30 degrees. Then the South Polar Region is only observed within the first Mercury years. This will to some extent limit the precision of the analysis of the global topography.

Thomas et al. (2007) summarize the instrument properties in more detail. Figure 2.10 shows the complete BELA instrument, the way how it will presumably look like. The instrument is designed to map the surface of Mercury with at most 10 Hz repetition rate and a range uncertainty of 1–2 m.

Furthermore, simulations are performed for the case that it shall be possible to take measurements at all spacecraft altitudes as well as for the more realistic case of restricting the altitude for observations. It may turn out that the final BELA flight instrument can take data at spacecraft altitudes much higher than 1000 km.

2.4 Time-dependent variations of the topography

Time-dependent variations of the topography can be divided into radial (vertical) and horizontal components, where the latter can be decomposed into longitudinal and latitudinal variations. Variations in latitude direction will not be discussed in the context of Mercury because they can only occur for planets of which the rotational axis is inclined with respect to the normal of their orbital plane. Mercury's rotation axis, however, is nearly perpendicular to its orbital plane. The radial elevation changes due to solar gravitation are called tidal elevations. Longitudinal variations of the topography due to solar torques on the non-spherical mass distribution of Mercury are called librations. Both the radial tidal elevation and the libration caused by solar gravitation depend on the interior structure of the planet, i.e. on density models, elastic properties and equation of state of the planet. The interior structure of planets has been described in more detail by Hofmann-Wellenhof and Moritz (2005), Murray and Dermott (1999), Torge (2003) and in sec. 2.1.2.

Both parameters of interest of this study, the tidal Love number h_2 and the forced libration amplitude Φ_{lib} , depend on the elasticity of a body. Elasticity depends on the interior structure. Planets can be differentiated into a mantle which mainly consists of rocks, and a core which mainly contains iron. Core and mantle are separated by a boundary. If the inner core were completely solid or frozen out, the planetary body would marginally react on solar forces. The mantle could only marginally slip with respect to the core; the libration amplitude would then hardly be detected by laser altimetry. In the case of a frozen core, the tidal amplitude would significantly decrease. A completely liquid Mercury would have a large tidal amplitude. Mercury, however, is certainly not completely liquid; it has a solid mantle and presumably a differentiated core. A differentiation of the core into an inner solid and an outer liquid core gives libration amplitudes as observed by Margot et al. (2007), and a tidal amplitude as theoretically derived by Van Hoolst and Jacobs (2003). The exact quantities of the tidal amplitude and the libration amplitude depend on the size of the inner and outer core.

Mercury is probably differentiated into an inner (solid) and an outer (liquid) core. Recent models on Mercury's interior can be found in Bois and Rambaux (2007), Rambaux et al. (2007) and Van Hoolst and Jacobs (2003). Due to its larger inner core and its thin outer liquid core, the tidal Love number h_2 can be estimated to be approximately 0.7 (Van Hoolst and Jacobs 2003). Zuber et al. (2007) discuss what can possibly be derived from MESSENGER (sec. 2.2.2) observations for the internal structure of Mercury. Margot et al. (2007) have already accurately measured the forced libration amplitude with ground-based radar interferometry to (35.8 ± 2.0) arcsec. From that it can be concluded that Mercury is very likely to have a liquid outer core.

2.4.1 Tidal elevation

Forces on a planet can be described by Newton's Gravitation law. In the center frame of Mercury the force $\mathbf{F}_{1\odot}$ between the Sun (\odot) and a mass element m_1 on Mercury's surface

$$\mathbf{F}_{1\odot} = -\frac{Gm_1M_{\text{Sun}}}{r_{1\odot}^2} \frac{\mathbf{r}_{1\odot}}{r_{1\odot}}, \quad (2.2)$$

where G is the gravitational constant, M_{Sun} the solar mass, and $\mathbf{r}_{1\odot} = \mathbf{R} - \mathbf{r}_1$ the vector from surface point 1 to the distant Sun with \mathbf{r}_1 the position of surface point 1 in Mercury's center frame. If Ψ is the angle between the general position vector \mathbf{r} and \mathbf{R} the vector pointing from Mercury's center to the Sun, the gravitational potential at a point P on Mercury's surface can be written as

$$V(\mathbf{r}) = -\frac{GM_{\text{Sun}}}{|\mathbf{R} - \mathbf{r}|} = -\frac{GM_{\text{Sun}}}{\sqrt{R^2 + r^2 - 2rR \cos \Psi}}. \quad (2.3)$$

Ψ depends on the co-latitude θ , the longitude λ and the time t . This potential can be expanded. Besides the mean gravitational potential in which Mercury moves on a Keplerian orbit, one obtains the tidal potential

$$V_{\text{tide}}(\mathbf{r}) = -\frac{GM_{\text{Sun}}}{R} \sum_{n=2}^{\infty} \left(\frac{r}{R}\right)^n P_n(\cos \Psi), \quad (2.4)$$

where P_n are the Legendre polynomials of degree n . As the ratio between r and R is only of order 4×10^{-5} , usually only degrees $n = 2$ and $n = 3$ are used (Van Hoolst and Jacobs 2003):

$$V_{\text{tide}}(\mathbf{r}) = -\frac{GM_{\text{Sun}}}{2} \frac{r^2}{R^3} \left[3 \cos^2 \Psi - 1 + \frac{r}{R} (5 \cos^3 \Psi - 3 \cos \Psi) \right]. \quad (2.5)$$

This tidal potential leads to a deformation of Mercury's geoid. The Love number h is a dimensionless number which gives the ratio between the actual tidal elevation of the planetary surface with respect to the tidal elevation of the geoid. The unperturbed geoid of Mercury is assumed to be a sphere. Mercury is slowly rotating which causes a small flattening

$$f = \frac{r_{\text{equatorial}} - r_{\text{pole}}}{r_{\text{equatorial}}}, \quad (2.6)$$

where $r_{\text{equatorial}}$ is the mean equatorial radius from center of mass, and r_{pole} the mean polar radius. At present, only an upper limit of $f < 10^{-6}$ can be given, because until now the equatorial and polar radiuses are known with the same value.

In general, there are different kinds of Love numbers which have to be distinguished from each other. The Love numbers h and l describe respectively radial and horizontal variations of the topography, while k describes changes of Mercury's gravitational potential due to mass displaced by tidal interaction. Extracting k is one of the primary goals of the radio science experiment MORE on board BepiColombo which will additionally provide the spacecraft position with less than 1 m after post-processing (Milani et al. 2001). The gravitational Love number is not directly seen by laser altimeter records. A suggestion how to extract the tidal Love number k_2 from laser altimeter records will be provided in ch. 8.

In the following the general equations will be developed and analyzed before going into detail for the tidal Love number h_2 which is of main interest here. The potential for the second and third power which generate tides can be described as Van Hoolst and Jacobs (2003):

$$V(r) = -\sum_{n=2}^3 \left(\frac{r}{a}\right)^2 \sum_{m=0}^n C_n^m(\cos \theta) \mathcal{R}_{n,m}(X, Y, Z, \chi), \quad (2.7)$$

where \bar{a} is the mean equatorial radius of Mercury with 2440 km, G_n^m depends on the latitude of surface point P , χ is the mean Mercurian sidereal time, which can be expressed as $\chi = H - \alpha - 180^\circ$. H is the local hour angle of the Sun and α the right ascension. Therefore χ is time-dependent. $\mathcal{R}_{n,m}$ contains the complete potential

$$\mathcal{R}_{n,m} = \frac{3}{4} GM \frac{a^n}{R^{n+1}} H_{n,m}, \quad (2.8)$$

with

$$H_{2,0} = \frac{1}{3} - \frac{Z^2}{R^2}, \quad (2.9)$$

$$H_{2,1} = -2 \frac{XZ}{R^2} \cos \chi - 2 \frac{YZ}{R^2} \sin \chi, \quad (2.10)$$

$$H_{2,2} = \frac{X^2 - Y^2}{R^2} \cos 2\chi + 2 \frac{XY}{R^2} \sin 2\chi, \quad (2.11)$$

$$H_{3,0} = \frac{1}{3} \frac{Z}{R} \left(3 - 5 \frac{Z^2}{R^2} \right), \quad (2.12)$$

$$H_{3,1} = \frac{1}{2} \left[\frac{X}{R} \left(5 \frac{Z^2}{R^2} - 1 \right) \cos \chi + \frac{Y}{R} \left(5 \frac{Z^2}{R^2} - 1 \right) \sin \chi \right], \quad (2.13)$$

$$H_{3,2} = 5 \left[\frac{(X^2 - Y^2)Z}{R^3} \cos 2\chi + 2 \frac{XYZ}{R^3} \sin 2\chi \right], \quad (2.14)$$

$$H_{3,3} = -\frac{5}{6} \left[\frac{X}{R^3} (X^2 - 3Y^2) \cos 3\chi + \frac{Y}{R^3} (3X^2 - Y^2) \sin 3\chi \right], \quad (2.15)$$

where X , Y , and Z are rectangular coordinates with the origin in the center of mass of Mercury, and the equatorial plane is the (X, Y) -plane. These coordinates are given by

$$X = R \cos \delta \cos \alpha, \quad Y = R \cos \delta \sin \alpha, \quad Z = R \sin \delta, \quad (2.16)$$

where δ is the declination of the Sun. The surface displacement $\Delta \mathbf{x}$ can then be written as

$$\Delta x_r = -\frac{1}{g} (h_2 V_2 + h_3 V_3), \quad (2.17)$$

$$\Delta x_\theta = -\frac{1}{g} \left(l_2 \frac{\partial V_2}{\partial \theta} + l_3 \frac{\partial V_3}{\partial \theta} \right), \quad (2.18)$$

$$\Delta x_\lambda = -\frac{1}{g} \left(l_2 \frac{\partial V_2}{\sin \theta \partial \theta} + l_3 \frac{\partial V_3}{\sin \theta \partial \lambda} \right), \quad (2.19)$$

where V_n is the potential which generates the tides up to degree n and can be derived with eq. (2.7) (Van Hoolst and Jacobs 2003). h_3 is almost two times smaller than h_2 . The horizontal Love numbers l_2 and l_3 are 5 and 50 times smaller. The horizontal Love numbers can be neglected, as their size is significantly smaller than the laser footprint size. The uncertainty of a laser shot is approximately 1 m which is the size of h_2 . Retrieving h_3 will not be possible with BELA, as the tidal potential at $h = 3$ is much smaller than the relative uncertainty of BELA, too.

The radial tidal displacement of Mercury's surface described with the tidal Love number h_2 is approximately given by

$$\delta r = h_2 F_{\text{tide}}(\Psi, R) = h_2 \frac{M_{\text{Sun}} a^4}{M_{\text{Merc}} R^3} \left[\frac{3}{2} \cos^2(\Psi - \delta_{\text{tide}}) - \frac{1}{2} \right], \quad (2.20)$$

where δ_{tide} is the tidal phase lag (e.g. Van Hoolst and Jacobs 2003). The tidal phase lag is supposedly small and is set to zero here. For a given solar hour angle Λ at zero longitude in Mercury's rest frame, one has

$$\cos \Psi = \sin \theta \cos \delta \cos(\Lambda + \lambda) + \cos \theta \sin \delta. \quad (2.21)$$

The declination never exceeds the obliquity $\delta_{\text{obl}} \approx (2.11 \pm 0.1)$ arcmin (Margot et al. 2007), which is so small that δ_{obl} is set to zero. The angular dependence of the tidal potential can then be written

$$\frac{3}{2} \cos^2 \Psi - \frac{1}{2} \approx -\frac{1}{4} (3 \cos^2 \theta - 1) + \frac{3}{4} \sin^2 \theta \cos 2(\Lambda + \lambda). \quad (2.22)$$

The first term on the right side is the long-period (zonal) tide and the second term represents the semi-diurnal (sectorial) tide. The terminology is not fully appropriate, because of Mercury's long sidereal rotation period of 58.65 days and the 3 : 2 spin-orbit resonance, both tides have a fundamental period of one Mercury year (88 days), which equals half a solar day on Mercury. For a Love number $h_2 = 0.74$, the zonal tides have a peak-to-peak amplitude of 60 cm at the poles (Van Hoolst and Jacobs 2003) due to the distance variations to the sun in Mercury's eccentric orbit. The sectorial tides have a peak-to-peak amplitude of up to 180 cm on Mercury's equator at zero longitude.

2.4.2 Libration amplitudes

Mercury is slightly elongated in the equatorial plane with the major axis at longitudes $\lambda = 0$, $\lambda = \pi$ pointing towards the Sun at perihelion. The solar torque acting on this permanent bulge causes the forced libration. The torque is proportional to $(B - A) \sin 2\Lambda$ (Murray and Dermott 1999), where A and B are the two equatorial components of the moment-of-inertia tensor. The libration angle δ_{lib} is defined as the difference between Mercury's sidereal rotation angle and the angle $3M/2$ obtained for uniform rotation, where M is the mean anomaly. The libration angle δ_{lib} can be written as a series of sine terms in M

$$\delta_{\text{lib}} = \Phi_{\text{lib}} f_{\text{lib}}(M) = \Phi_{\text{lib}} \left[\sin M + \sum_{n=2}^{\infty} a_n \sin(nM) \right], \quad (2.23)$$

where Φ_{lib} is called the libration amplitude. The coefficients a_n decrease rapidly with n , a_2 being -0.105 (Jehn et al. 2004). Φ_{lib} is proportional to $(B - A)/C_m$, where C_m is the moment of inertia of that part of the planet that contributes to the librational motion. If the solid mantle can slip at the core mantle boundary, C_m is the moment of inertia of the mantle plus crust, otherwise C_m is equal to the moment of inertia C of the entire planet (Peale 1976a)

$$\frac{C_m}{C} = \frac{C_m}{B - A} \times \frac{B - A}{Ma^2} \times \frac{Ma^2}{C}. \quad (2.24)$$

The first term on the right side is obtained from the libration amplitude, the second equals four times the quadrupole gravity coefficient C_{22} , and the third term is related to the gravity coefficients C_{20} , C_{22} and to δ_{obl} , if Mercury is in Cassini state. A planet is in Cassini state, when the planet has an evolved rotational state where the spin axis, orbit normal, and normal to the Laplace plane are coplanar while the obliquity remains constant, and a Laplace plane is defined as the plane about which a planet's orbit precesses with constant inclination to the equatorial and ecliptic planes (Yseboodt and Margot 2006). Margot et al. (2007) have determined the value of $(B - A)/C_m$ from ground-based measurements of the libration amplitude to $(2.03 \pm 0.04) \times 10^{-4}$. Using the value $C_{22} = (1.0 \pm 0.5) \times 10^{-5}$ from Mariner 10 observations (Anderson et al. 1987), they have determined the ratio C_m/C to be approximately 0.5 with a large uncertainty of ≈ 0.3 primarily due to the large uncertainty of C_{22} . For a typical structural model of Mercury, $C_{\text{mantle}}/C \approx 0.5$. Therefore, Margot et al. (2007) conclude from their results that Mercury's solid mantle slips at the core-mantle boundary, which suggests that Mercury has a liquid outer core.

In general, the Sun causes a torque T on Mercury's spin axis

$$T = -\frac{3GM_{\text{Sun}}}{2r^3} (B - A) \sin 2\Psi. \quad (2.25)$$

Figure 2.11 shows this relation, it is taken from Balogh et al. (2002). Additionally θ and f are introduced, where θ is the rotation angle in inertial space, and f the true anomaly of the planet around the Sun. A general introduction is given, e.g., in Balogh et al. (2002) and Jehn et al. (2004). The order of the different libration amplitudes are even much smaller than the 88 day libration amplitude which is based on Mercury's 3 : 2 resonance. The tidal reaction of the planet has additionally to be taken into account for retrieving the forced libration amplitude. As the libration amplitude is, furthermore, related to the tidal Love number h_2 , h_2 has to be included in the analysis and determined in a first step.

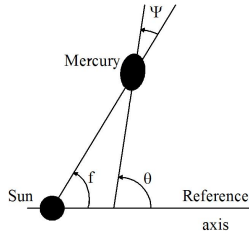


Figure 2.11: Geometry of the torque for Mercury's spin axis. θ is the angle of Mercury's long axis with the inertial reference axis, and Ψ the angle in the direction to the Sun. The true anomaly of Mercury can then be described as $f = \theta - \Psi$ (Balogh et al. 2002).

Balogh et al. (2002) describe the libration amplitude as a series of sine-terms which depend on the eccentricity of the planet. The linearization of the series leads to an approximation which is based on the zonal coefficients of a spherical harmonic expansion. Extracting the 88 day libration amplitude is one of the scientific goals of the BepiColombo

mission. It is possible with the camera (Capaccioni et al 2005) and the BepiColombo laser altimeter BELA (Oberst 2007). Margot et al. (2007) use ground-based observations of the libration amplitudes, and achieve results with an uncertainty of (35.8 ± 2.0) arcsec.

In this study the error budget for the libration amplitude is overwhelmingly dominated by the uncertainty in C_{22} at the present stage. The upcoming space missions with orbiting spacecraft will determine the gravity coefficients and the obliquity with high precision. The uncertainty in the libration amplitude may then be dominant and it is worthwhile to study how well it can be constrained by laser altimeter data.

3 Forward modelling of synthetic laser altimeter data

A synthetic topography model and a set of laser shots for the nominal orbit of MPO are synthetically generated for investigating whether the tidal Love number, libration amplitude, and global topography can precisely be extracted. A synthetic topography model has the main advantage that the topography which shall be extracted is accurately known. The generated topography is expressed as a spherical harmonic expansion where the total power of the coefficients for a certain harmonic degree l can be expressed by a power law of the form

$$V_l = \sum_m (C_{lm}^2 + S_{lm}^2) = \frac{A^2}{l^k}. \quad (3.1)$$

The coefficients of the topography are randomly synthesized up to a maximum degree l_{max} . Integrating the power of the small-scale topography which is not modeled up to infinity results in an error of 62.5 m. As this uncertainty is assumed to have a normal distribution, the measurement uncertainty of one laser shot is modeled by a random number with a normal distribution of zero mean and a standard deviation of 62.5 m. The chosen power law is described in more detail in sec. 2.1.2 and shown in fig. 2.3.

A laser shot has several uncertainties, where the main components are the spacecraft positioning uncertainty, instrumental uncertainties, surface properties, and systematic uncertainties. The spacecraft position is provided by the MORE experiment on board the Mercury Planetary Orbiter (MPO) of the BepiColombo mission (Milani et al. 2001). The position will be provided with a precision of about 0.1 m (personal communication with Milani, 2006). Instrumental uncertainties of the laser altimeter are, e.g., pointing uncertainties, beam divergence, range uncertainty, and surface slope within the laser footprint. Gardner (1982, 1992) carried out analyses of the importance of the specific uncertainties of laser altimeter records.

The spacecraft altitude is known with 1 m uncertainty, and the footprint sizes which depend on the beam divergence are marginally small in comparison to the longitudinal surface coverage of the laser altimeter which depends on the chosen orbit. The orbit restricts the extraction of global topographic features, as the longitudinal coverage is limited. Systematic errors are assumed to be marginally small so that they can be neglected. They have to be analyzed, but this is beyond the scope of this work. Chapter 8 will analyze this in more detail. To simplify the analyses, a general value of 5 m for positioning and instrumental uncertainties is assumed. The largest uncertainty is based on the topography that is not modeled.

This approach for generating the synthetic topography model and synthetic laser al-

timer measurements is used for both analysis methods a) using global basis functions i.e. a spherical harmonic expansion and b) using local basis functions i.e. different trial functions for the data points within a rectangular grid. The results for the method with the global basis functions are presented in ch. 4, and the results for the method with local basis functions are summarized in ch. 5.

3.1 Deterministic topography model of Mercury

The deterministic time-invariant part of the input topography model is given by

$$T(\theta, \lambda) = \sum_{l=0}^{l_{max}} \sum_{m=0}^l P_l^m(\cos \theta) \{C_{lm} \cos(m\lambda) + S_{lm} \sin(m\lambda)\}, \quad (3.2)$$

where the P_l^m ($m \leq l$) are normalized associated Legendre functions of degree l and order m . To synthesize Mercury's topography, the input values for the spherical harmonic coefficients C_{lm} and S_{lm} need to be determined first. For the method using global basis functions, the coefficients up to degree $l = 16$ have been taken from the lunar topography model. This gives the model some resemblance of a real planet, although Mercury certainly looks different. Random values are assigned to the coefficients from $l = 17$ to 1024, assuming a Gaussian distribution around a zero mean. For the method using local basis functions, all input coefficients from $l = 1$ to $l_{max} + 1$ are generated by a random number generator. The standard variation of the input coefficients is such that the degree power V_l varies with l as

$$V_l = \sum_m (C_{lm}^2 + S_{lm}^2) = \frac{A^2}{l^k}. \quad (3.3)$$

A slope of $k = 2.0$ is appropriate for terrestrial planets (Vening Meinesz 1950, Neumann et al. 2004), and A is set to 2000 m, which gives a smooth match with the lunar topography for the long-wavelength part of the model. Aharonson et al. (2001) determined the power spectral density for the Mars southern hemisphere which is in fairly good agreement with the chosen model, although this power spectral density has a lower level by about factor 2 (fig. 2.3). Mercury can be assumed to be more subdued than the Moon for the larger wavelengths. Therefore, the assumptions for the analysis are conservative. A more damped topography would lead to a better determination of the tidal Love number and the topography.

Using a single topography model in the inversion may result in a fortuitously high level of accuracy for the recovery of the Love number. Therefore the inversion was done for 20 topography models that differed in their coefficients for $l > 16$ for the global basis functions (ch. 4). For the case when local basis functions (ch. 5) are used, the accuracy for extracting the tidal Love number depends on the chosen, synthetic input topography. Therefore, 22 different topography models are analyzed with 20 different noise realizations. The mean accuracy of the topography for the whole surface does not depend on the input topography. More important is the chosen topography grid which is used for the analysis.

Evaluating the spherical harmonic expansion (eq. 3.2) for each of the simulated shot points would be far too time-consuming, because the number of shot points is of the

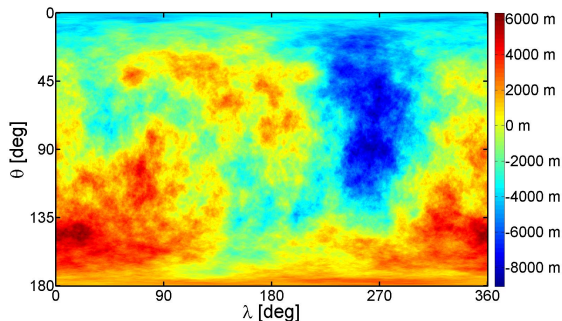


Figure 3.1: Simulated input topography for one specific random number where the coefficients of the spherical harmonic expansion from $l = 1$ to l_{max} are generated by a random number generator.

order 10^8 and they are not regularly distributed in (θ, λ) . Therefore, the topography is first calculated for a regular 3072×1536 longitude-latitude grid on Mercury's surface. Figure 3.1 shows one example of a transformed input topography for one random number for initializing the random number generator and where the coefficients of the spherical harmonic expansion are randomly computed except the coefficient C_{00} . The topography at the actual position of the laser foot points is determined by a third-order Lagrangian interpolation using the 16 surrounding grid points.

For each shot point the position of the MPO relative to Mercury's centre of mass is first determined in an inertial reference frame (sec. 3.2). Longitude and latitude of the laser footprint on the rotating planet are then calculated by taking into account the libration according to eq. (2.23). A libration amplitude of $\Phi_{lib} = 40$ arcsec is assumed.

Furthermore tidal elevation is added to the static height at each shot point, which depends on R , Λ , λ , θ and h_2 according to eqs. (2.20) and (2.22). An input value of $h_2 = 0.7000$ and values listed in tab. 2.1 for the orbital and other relevant parameters of Mercury are assumed.

3.2 Distribution of laser shot points

For simplicity a strictly Keplerian orbit of the MPO around Mercury's center of mass is assumed. Such an assumption does not limit the feasibility study, given that the spacecraft position will be properly tracked by the Radio Science Experiment MORE onboard MPO (Milani et al. 2001). The Keplerian elements are listed in tab. 3.1 in accordance with the nominal orbit of the MPO. Two slightly different orbits are used for the analysis. The first is a resonant orbit, meaning that Mercury's rotation period is an integer multiple of the spacecraft orbital period T_{MPO} . After two Mercury years the ground track will repeat exactly as before. The second orbit does not include any resonance. The orbital parameters of MPO which are used for the simulations are listed in tab. 3.1. As a first approach in the simulations of BELA data, the argument of periapsis of MPO has been

Table 3.1: MPO parameters

Parameter	Symbol	Value		
		Resonance		No Resonance
Number of MPO cycles		910.000	909.750	909.234
Semi-major axis	R_{Merc} [km]	3389.218	3389.839	3391.121
Eccentricity	e		0.162	
Inclination	i [degree]		89.9	
Period	T_{MPO} [hr]	2.320	2.321	2.322
Min./max. altitude	[km]		400/1500	
Longitude of node	Ω [degree]		0.0	
Argument of periherm	ω [degree]		0.0	

chosen to be constant at zero latitude. MPO's orbit is mainly chosen to be elliptical for minimizing the time which MPO is directly illuminated by the Sun. Then the temperature variation can not reach high values and the mission has a longer life time. The orbit is almost polar, the orbital plane aligns with the apsides of Mercury's orbit and the periherm lies on the equator. The periherm will actually move to higher latitude during the mission, which is ignored here. For this study, the position of the spacecraft, in particular its distance from Mercury's center of mass is assumed to be precisely known.

A shot frequency of 5 Hz is taken for the laser altimeter, although a higher frequency will be possible. This means that shot points along the ground track are 300 m apart at periherm and more closely spaced in other parts of the orbit. Because of Mercury's slow rotation, consecutive ground tracks will be separated by approximately 26 km at the equator. Observations are chosen to be available for at least four Mercury years or six sidereal days, after which the average longitudinal spacing of ground tracks is 2 km at low latitudes, provided that measurements can be performed over the entire orbit including at apoherm. All longitudes on the planet will then have been visited six times, at different stages of the tidal cycle, which is a condition for detecting the signal of the sectorial tide in the altimeter measurements. The laser is assumed to be exactly nadir-pointing. The pointing uncertainty of 5 arcsec does not affect the distance measurement by more than 1 cm. The horizontal displacement can reach approximately 25 m which is smaller than the footprint size. Resolving the surface roughness within the laser footprint is a difficult task which can hardly be solved.

A basic requirement for the BELA instrument is that it can reliably determine the distance for a spacecraft altitude up to 1000 km. This covers an angular range in the orbit of approximately 207 degrees. Measurements from higher altitudes may be possible, but would suffer from an increasing rate of missed return signals or false detections (Gundersen et al. 2006). Here, it will first be assumed that height data are obtained over the whole orbit, including at apoherm. In a further step, only a data set where measurements are limited to a maximum spacecraft altitude of 1000 km will be used. Additional limitations for the analyses are based on incomplete coverage. Two main restrictions of the data set are present which will be investigated: a) latitudinal restrictions, i.e. due to limitations of instrumental parameters which are described in sec. 2.3.5, and b) longitudinal restrictions,

e.g. the mission duration or simulation time.

3.3 Noise sources

A stochastic noise contribution N_k is added to the deterministic static topography T and the tidal displacement δr_{tide} at each shot point k to obtain the simulated topographic measurement T_k :

$$T_k = T(\theta_k, \lambda_k + \Delta\lambda_{\text{lib}}) + \delta r_{\text{tide}}(\Psi_k) + N_k. \quad (3.4)$$

The noise has a Gaussian distribution with a standard deviation of 62 m. Only a small fraction of this represents measurement errors or errors in the spacecraft position. Most of it accounts for the topographic roughness at scales smaller than the cutoff in harmonic degree of the input topographic model, i.e. $l_{\text{max}} = 1024$, corresponding to a wavelength of 15 km. To estimate the topographic variance at small scales the validity of the power law (eq. 3.3) to $l \rightarrow \infty$ is assumed. Summing up from l_{max} to ∞ gives a total small-scale variance of 3900 m², or a standard deviation of 62.5 m. Of course, this is the average roughness and occasionally much larger deviations occur, e.g., more than 200 m for 1% of the points.

This treatment of small-scale roughness in the model may be overly pessimistic. On Mars, 1-D spectra of roughness obtained along MOLA tracks suggest that the spectral slope steepens to values $k > 2$ at wavelengths smaller than about 10 km (Aharonson et al. 2001). Also, assigning to each shot point a noise value that is uncorrelated to that of neighboring points is a worst case assumption and certainly not realistic for the small-scale topography. Moon's regolith includes huge variations of the sub-millimeter scale shown by Helfenstein and Shepard (1999). This is far beyond the resolution which can be retrieved by laser altimetry. Longer scales in the range half of the shot point distance is hardly to be resolved. In general the analysis is dominated by the longer scales of the topography. A standard deviation of 62 m can be assumed to be the worst case for the chosen case. The effect of the small-scale variation is expected to be smaller. Especially in post-processing, the uncertainty can be assumed to be even much smaller.

However, a critical assumption is that the distribution of the noise is purely random. This is an essential prerequisite for reducing the error by the large number of measurements to the decimeter level that is required for retrieving the Love number. Systematic errors, in particular if they have a periodic component with the same period as the tide (for example in the determination of the orbit) would seriously compromise the method for determining h_2 .

4 Extraction of the static and time-dependent topography by a spherical harmonic expansion

A primary goal of the BepiColombo laser altimeter (sec. 2.3.5) is the extraction of the time-dependent parameters of the static topography expressed as tidal Love number and forced libration amplitude and the long-wavelength topography expressed as a spherical harmonic expansion. The closest approach is to extract the long-wavelength topography directly. The extracted value of the tidal Love number is directly connected to the topography and can be extracted simultaneously with the static topography. The basis functions of the tidal Love number h_2 are expressed by coefficients of the static topography (Van Hoolst and Jacobs (2003) and sec. 2.4). Additionally basis functions of the tidal Love number include a time-dependency which can mainly be related to Mercury's orbit around the Sun. The effect of the second degree order coefficients for the tidal elevation can be expressed as a series of harmonic coefficients. Van Hoolst and Jacobs (2003) analyzed this in more detail. Extracting the libration amplitude Φ_{lib} does not linearly depend on the static topography and the tidal Love number. The dependency is weakly non-linear. For the extraction good approximations are needed for the static topography and the tidal Love number. The basis functions of the forced libration amplitude are also expressed by the coefficients of the spherical harmonic expansion of the static topography. Similar to the tidal elevation the effect of the libration amplitude is expressed by a series of coefficients which contains the time-dependency related to Mercury's orbit around the Sun.

The static topography, tidal Love number and libration amplitude shall be extracted simultaneously from a synthetic data set (sec. 3.2 and 3.3) based on a topography model as described in sec. 3.1. After introducing the topic in more detail and describing the methods for retrieving the spherical harmonic coefficients, the tidal Love number and forced libration amplitude (sec. 4.2), and investigations for different weighting schemes in order to retrieve a best possible fit of the parameters will be presented. The weighting scheme is adopted for using the orthogonality criteria of the spherical harmonic expansion. Changing the weights affects the structure of the inversion matrix where the off-diagonal elements are then decreased. This simplifies the inversion of the matrix. Furthermore, weighting-down the simulations results in an equal distribution of the laser shots over the entire surface. With the optimum weighting scheme the simulations are carried out with different realizations of noise (sec. 4.3), and afterwards with different realizations of the deterministic input topography and different orbits, but only one representation of noise

(sec. 4.4). At the end a regression for the uncertainties of the time-dependent variations is prepared, assuming that their uncertainties decrease as a power law with the maximum degree of inversion l_{inv} (sec. 4.5).

4.1 Introduction into the extraction by spherical harmonic analysis

It is first investigated whether the topography of a planet can be extracted from laser altimeter records where the topography is expressed as a spherical harmonic expansion. Spherical harmonic coefficients include the important information about scaling laws of a planet. Head et al. (2007) and Neumann et al. (2004) describe for example the topographies of Mars and Moon. The topography can be described for small scales with wavelengths of several kilometers. Here, it will be shown that the long-wavelength topography of Mercury (sec. 2.1.2) can accurately be extracted with a mean uncertainty of less than 10 cm. This is one of the main goals of the BepiColombo mission and in particular of the BepiColombo laser altimeter (sec. 2.2.3 and 2.3.5).

In the following sections, the mathematical approach will be presented, on which the simulations are based. It will then be analyzed in detail which parameters may play a major role. Different weighting schemes of the laser altimeter data records have a large effect. Results will be presented in sec. 4.3. The simulations are first approaches, to show which limitations arise. The limitations strongly depend on the time-dependent variations expressed as tidal Love number h_2 and the forced libration amplitude Φ_{lib} . On optimizing the weighting scheme the errors of the coefficients are approximately of the same order, while the accuracy of the tidal Love number and the retrieved value for the tidal elevation changes and the libration amplitude vary and show dependencies on the limitations.

An introduction is given in Koch et al. (2008), Margot et al. (2007), Peale (1972) and Van Hoolst and Jacobs (2003). The simulations are based on different representations of noise. It will be shown and investigated how the results of the time-dependent variations and the long-wavelength topography, expressed as spherical harmonic expression, depend on the different noises which are at least one magnitude larger than the presumable uncertainty of the laser altimeter measurement of the BepiColombo mission itself (Sec. 2.3.5), which is given as 1 m by Thomas et al. (2007).

In a first step, the effect of different weighting schemes and additionally the impact of an incomplete coverage of the surface with laser altimeter records is investigated. Incomplete coverage of the surface with observations can be assumed for each satellite mission, as in general restrictions due to temperature, orbit design, or other parameters arise. The simplest case is based on the use of a simulation time which is not a multiple of the tidal period. Furthermore, data gaps can be assumed. Data gaps are caused on the one hand by restrictions to the instrument, and on the other hand by restrictions from the environment. Restrictions due to the instrument can, e.g., be heating and cooling of the instrument. Another instrumental restriction is related to the background noise which is mainly solar radiation which is reflected by Mercury's surface (albedo).

Orbital parameters for example are specified as environmental restrictions. Laser altimeter observations in an elliptical orbit as for the BepiColombo mission (sec. 2.2.3) are not possible for spacecraft altitudes larger than 1000 km. This special case is analyzed

in more detail in sec. 4.3.2. Different weighting schemes affect the extraction of the tidal Love number h_2 and the forced libration amplitude Φ_{lib} .

After investigating different weighting schemes and retrieving the best one for the simulations, a closer look at different topographies is taken, where the power law of the input topography (sec. 3.1) varies for degrees and orders larger than 16, as the long-wavelength scales are taken from the long-wavelength topography of the Moon.

The uncertainties of the time-dependent variations decrease as a power law with larger maximum degrees of inversion for the spherical harmonic expansion. Regressions are computed for the time-dependent variations in sec. 4.5. It can be shown that the extraction of the libration amplitude has approximately the same exponent of the power law. The uncertainties decrease for a resonant orbit, and the decrease is slower for a non-resonant orbit. Restricting the data to spacecraft altitudes smaller than 1000 km hardly leads to different exponents in the power law. The uncertainty for the largest degree of inversion l_{inv} is about 12 %. The uncertainty can be assumed to be even much smaller for larger degrees of inversion.

4.2 Least-squares inversion

The generation of the deterministic input topography, of the laser shots, and of the noise are described in ch. 3. The laser shots are simulated for the complete orbit. The data are restricted within the simulations, either by varying the input parameter or taking data out of the simulation. The analysis method is based on a two-step inversion of the simulated data set of height measurements. In the first step, the low-order topography coefficients and the Love number are solved by a least-squares inversion simultaneously. Including the libration amplitude into the inversion changes the problem to a weakly nonlinear one and requires a second iteration step. The recovered values of the topography coefficients, Love number and libration are then compared to the input values.

4.2.1 Inversion for topography and Love number

In the first inversion, the libration amplitude is treated as given, but a value of 30 arcsec is assigned that does not agree with the input value of 40 arcsec taken to calculate the shot point position in Mercury coordinates. With this different initial value, the nominal longitude λ_k of the laser shot points is calculated by using in the first inversion step. The coefficients C_{lm}, S_{lm} of the static topography and for h_2 are simultaneously solved for by minimizing

$$\sum_k w_k \left[T_k - h_2 F_{\text{tide}}(\Psi_k) - \sum_{l,m=0}^{l_{inv},l} P_l^m(\cos \theta_k) \{ C_{lm} \cos m\lambda_k + S_{lm} \sin m\lambda_k \} \right]^2 \quad (4.1)$$

Here, l_{inv} is the maximum harmonic degree which is inverted and the w_k are weights assigned to each measurements. Ordering the unknown coefficients and h_2 into a $(N+1)$ -dimensional vector \mathbf{x} , where $N = (l_{inv} + 1)^2$, a normal matrix equation of the least-squares inversion process is needed to be solved

$$\mathbf{Ax} = \mathbf{b}, \quad (4.2)$$

where the elements of the $(N + 1) \times (N + 1)$ matrix \mathbf{A} and the right-hand side vector \mathbf{b} are given by

$$a_{ij} = \sum_k w_k F_i(\theta_k, \lambda_k, t_k) F_j(\theta_k, \lambda_k, t_k), \quad (4.3)$$

$$b_i = \sum_k w_k T_k F_i(\theta_k, \lambda_k, t_k). \quad (4.4)$$

For $i \leq N$ the basis functions $F_i(\theta, \lambda, t)$ are the spherical harmonic functions, which are independent of the time of observation t_k . For $i = N + 1$ the basis function depends explicitly on time, $F_{N+1}(\theta, \lambda, t) = F_{\text{tide}}(\Psi)$, where the relation between Ψ and (θ, λ, t) is obtained from eq. (2.22).

The most time-consuming part of the simulation is the calculation of the matrix elements because each of the $\approx 10^8$ measurements contributes to each element of the matrix. The number of matrix elements increases with the fourth power of l_{inv} and reaches 10^7 at $l_{\text{inv}} = 56$. Therefore, the maximum degree of the inversion model must be much smaller compared to that of the input model in a direct inversion for the spherical harmonic representation of the static topography. In this study, l_{inv} is limited to ≤ 64 . In order to reduce the workload for calculating the inversion matrix, a certain number of topography measurements (typically 25) are lumped along the ground track, i.e. their average is calculated and treated as if it were a single measurement located at the central footprint of the ensemble. A comparison has shown that the inversion results do not differ from the case of treating each shot separately. While normally weighting is used to account for variable data quality in an inversion problem, here the choice of weights w_k is governed by a different principle. As it will be discussed in detail in Sec. 4.3, it is advantageous to use the weights to simulate a uniform coverage of different surface regions with data points (and uniform temporal coverage for retrieving the time-dependent part of topography). In the polar orbit, high latitudes are more densely sampled, proportional to $\sin^{-1} \theta$. Furthermore, assuming a constant shot frequency of the altimeter, the density of points along-track varies with the inverse of the orbital angular velocity of the spacecraft, or proportional to the square of the distance r from the centre of Mercury. In the simplest case of continuous measurements from all parts of the orbit, a uniform coverage is obtained by choosing

$$w_k \sim r_k^{-2} \sin \theta_k. \quad (4.5)$$

If data gaps are present, the weighting scheme must be modified, as discussed below.

4.2.2 Inversion for the amplitude of forced libration

In a second step, the libration amplitude is treated as an additional unknown and inverted for simultaneously with the static topography and the Love number. Including libration makes the inversion nonlinear, although for $\Phi_{\text{lib}} \ll 1$ it is weak, therefore one iterative step is sufficient.

$\Delta\Phi_{\text{lib}}$ is called the correction of the libration amplitude compared to the initial value used in the first inversion step and set for the corrected longitude of the shot point $\lambda_k^* = \lambda_k + \Delta\Phi_{\text{lib}} f_{\text{lib}}(M_k)$. Denoting by a hat the topography coefficients obtained in the first inversion and linearizing the trigonometric terms containing λ_k^* , the following expression

is obtained to be minimized

$$\sum_k w_k \left[T_k - h_2 F_{\text{tide}}(\Psi_k) - \sum_{l,m=0}^{l_{\text{inv}},l} P_l^m(\cos \theta_k) \{C_{lm} \cos m\lambda_k + S_{lm} \sin m\lambda_k\} \right]^2 + w_k \left[\Delta\Phi_{\text{lib}} f_{\text{lib}}(M) \sum_{l,m=0}^{l_{\text{inv}},l} P_l^m(\cos \theta_k) \{m\hat{\delta}_{lm} \cos m\lambda_k - m\hat{c}_{lm} \sin m\lambda_k\} \right]^2. \quad (4.6)$$

The additional condition on the libration requires that one more row and one more column are added to the inversion matrix \mathbf{A} , with the rest of the matrix being unchanged. A further inversion step, using $F_{\text{tide}}(\Psi^*)$ instead of $F_{\text{tide}}(\Psi)$ does not alter the retrieved values of the topographic coefficients, the tidal Love number, and the libration amplitude significantly. The values converge directly for the carried out investigations.

4.3 Optimization of the weighting scheme

Two sets of numerical simulations have been implemented. In a first step an idealized data set is used to explore the impact of the weighting scheme (sec. 4.2.1) on the resulting accuracy of the inverted static and time-dependent topography which will be presented below. Here, the dependency of the weighting scheme on varying the spatial and temporal data coverage is investigated. In a second step, more realistic assumptions on the spacecraft orbit are investigated, like a non-resonant orbit related to Mercury's rotation (sec. 4.4), or data gaps caused by restrictions of the maximum spacecraft altitude from which data are obtained to 1000 km. The second case is important for optimizing the weighting scheme of the simulated laser shots.

In order to test different weighting schemes, a single synthetic topography model, i.e. only one realization of input coefficients C_{lm} and S_{lm} , is used. However, 26 different realizations of noise have been used with a standard deviation of 62.5 m (sec. 3.3) considering the influence of the not-modeled part of the input topography by adding a normal distributed value with zero mean and a standard deviation of the power from $l_{\text{max}} + 1$ to ∞ which is not modeled. Additionally a resonance between Mercury's rotation period and the spacecraft orbit is assumed, with 910 orbital periods corresponding exactly to one Mercury year. As first approach data for exactly two Mercury years are used to investigate restrictions. Afterwards the dependency on the temporal coverage is described. The retrieved results for the static topography as well as the results for the extracted tidal Love number h_2 and libration amplitude Φ_{lib} are presented.

4.3.1 Uniform surface coverage

The simplest assumption use equal weights for each simulated laser shot. The weighting scheme according to eq. (4.5) is closer on simulating a uniform surface coverage than using equal weights. The latter implies for example a down-weighting of the data in the Polar Regions, where the sampling is very dense. This is not related to differences in the data quality. In fig. 4.1, the spectra of the input topography and of the errors in the inverted static topography coefficients for both weighting schemes are shown as function

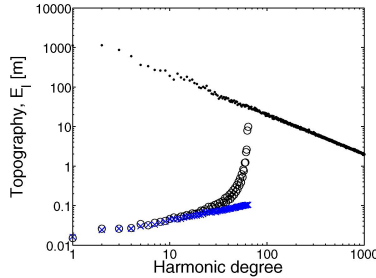


Figure 4.1: Harmonic degree power of static input topography (\cdot) and the harmonic degree errors E_l (eq. 4.7) of the inversion using constant weights (\circ) and weights simulating uniform surface coverage (blue \times).

of harmonic degree. The degree error is defined by

$$E_l = \sqrt{\sum_{m=0}^l (C_{lm}^{inv} - C_{lm})^2 + (S_{lm}^{inv} - S_{lm})^2}, \quad (4.7)$$

where the index inv indicates topography coefficients obtained in the inversions. The errors of the extracted topography coefficients remain at the centimeter level at low harmonic degrees where they increase smoothly with l . For uniform weighting the errors start to increase rapidly when the harmonic degree approaches the maximum degree of inversion, which is 64 in this case. With weighting that simulates a uniform surface coverage, the errors remain moderate up to the maximum inversion degree.

This improvement in accuracy can be understood for the hypothetical limit of infinitely dense data coverage. In this limit the summation over all measurement points in eq. (4.1) and (4.6) is turned into an integration over a spherical surface when weights according to eq. (4.5) are used. The inversion matrix becomes diagonal because of the orthogonality relation of the spherical harmonic basis functions $F_i(\theta, \lambda)$. Mathematically speaking, the inversion becomes in fact a projection of the topography on the basis functions, i.e. the non-diagonal elements of the inversion matrix described in eq. (4.3) vanish. The absolute uncertainty of each topographic coefficient is then roughly of the order of the uncertainty of a single topographic measurement divided by the square-root of the number of measurements. When using equal weights, the inversion matrix is non-diagonal even for arbitrarily dense coverage with measurement points. The uncertainties of all coefficients contribute to some extent to the errors of a particular coefficient, and to the errors of the retrieved tidal Love number and the retrieved libration amplitude. The numerical simulations yield that the weights simulating a uniform surface coverage are also the better choice for the inversion problem with finite density of data points. Additional investigations have then to be done on the effect of the laser shots and the weighting scheme, when real data are available.

The accuracy of the inversion for the tidal Love number and the libration amplitude has been analyzed in more detail. In particular, it has been studied whether there is a

correlation between the error of the inferred Love number and the maximum harmonic degree in the inversion for the static topography l_{inv} .

With uniform weighting, the errors are large for the inverted Love number, although they seem to decrease somewhat with the maximum degree of inversion for the static topography (fig. 4.2a). In contrast, when applying the weighting scheme simulating uniform surface coverage the Love number is determined much more accurately with a value close to 0.7 which is expected to be the real value and without an offset. The recovery of the libration amplitude is less sensitive to the weighting scheme than that of the Love number (Fig. 4.2b), although weighting for uniform surface coverage gives slightly better

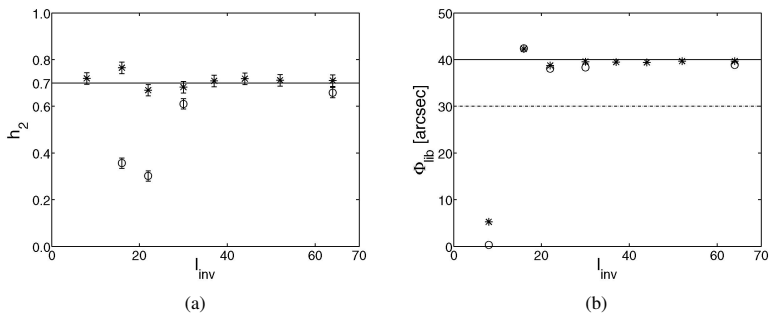


Figure 4.2: Extracted Love number (a) and extracted libration amplitude (b) vs. maximum harmonic degree for static topography. \circ are representing uniform weights and $*$ weights uniform surface coverage. Input values are indicated by horizontal lines. The dashed line in (b) indicates the initial value used in the first inversion step. The symbols indicate the mean value of the inverted Love number obtained for the 26 noise realizations. The error bars give the 1σ standard deviation for the different noise models. The inversion for the libration is prepared for a single noise model. The simulations are only carried out for special inversion degrees with equal weights (\circ), as the intermediate results show large offsets.

results. In any case, the accuracy of the extracted values of h_2 and Φ_{lib} increases with the maximum harmonic degree of the expansion of the static topography in the inversion. As the weighting scheme simulating a uniform surface coverage of measurements seems to be superior, all subsequent simulations are adopted like this.

The accuracy of the tidal Love number does not change with varying the maximum degree of the inversion for the static topography. The accuracy is related to the different noise realizations. The extracted value of the tidal Love number varies with the maximum degree of the inverted static topography expressed as spherical harmonic expansion. No direct correlation can be found. The value seems to oscillate around the expected value of 0.7000 which is further used as input value. Expressing the determined value of the tidal Love number as a function of the inversion degree l_{inv} is not possible due to two reasons: a) the deviation can be a random function which is not understood, b) the oscillation can not be expressed due to the restriction of the maximum degree of inversion. For a better and detailed analysis of this effect the inversion degree l_{inv} has marginally to be increased.

In general the basis function of the tidal Love number h_2 depends on the spherical harmonic coefficients of the static topography C_{20} , C_{22} and S_{22} . The more accurately these coefficients are determined as more precisely the tidal Love number is extracted. The simulations showed this dependency where no functional dependency can be found.

4.3.2 Data restrictions

Restrictions for the surface coverage by laser altimeter data records are simulated with time intervals of different lengths. Then the surface is not equally covered with simulations. It takes the MPO spacecraft 2 Mercury years to pass the same surface region at the same phase of the tidal cycle. If there is a fraction of a measurement period that exceeds an integral multiple of 2 Mercury years, it is necessary to adapt the weighting scheme such that not only uniform surface coverage is ensured, but also the different stages of the tidal cycle at a given location are equally covered after weighting. Simulations are prepared for this case and a maximum inversion degree of 16. Figure 4.3 shows the results for a uniform surface coverage (\square) and the adopted weighting scheme (+). The retrieved values of the tidal Love number show that the weighting scheme is optimized for data coverage of a factor of 2 Mercury years. The x-axis is labeled in Mercury days, 2 Mercury years can be expressed as 3 Mercury days due to Mercury's 3:2 spin rate. Four cases are chosen for a more detailed analysis: a) 3 Mercury days, as this is a direct factor of 2 Mercury years, b) 3.75 Mercury days, as the extracted value for h_2 is far away in the direction of 0, c) 4.5 Mercury days, as this is half of the tidal period and the extracted value is close to the one retrieved for a factor of 2 Mercury years, and d) 4.75 Mercury days, as the first result has a large offset and is much larger than 1. These cases are to some extent extremes and do not present all possible cases. These cases coincide with the libration amplitude (fig. 4.3b). For these chosen cases, the weighting scheme is generalized so that the distribution of simulations over the whole surface is uniform over a period of 2 Mercury years. The weights are multiplied by an additional factor for down-weighting areas which are observed more than others. The previously found optimum weighting scheme of uniform data coverage of the surface is further expanded. The four chosen cases are shown as + in fig. 4.3. The topography looks inferior and increases marginally up to the maximum degree of inversion if the weighting scheme is not adopted as described above (but is not shown, as the figure would equal fig. 4.2, when weights are assumed as 1). After adopting the weighting scheme, a similar result as shown in fig. 4.1 for equal weighting and a uniform surface coverage is obtained. As no new information can be distinguished from this graphic, it is not shown.

Simulations are also carried out for a simulation time of 2 Mercury years. Due to instrumental restrictions, observations of BELA will only be possible up to spacecraft altitudes of 1000 km (sec. 2.3.5). Restricting the simulations for spacecraft altitudes up to 1000 km leads to a more dense coverage of the Polar Regions. The areas which are observed twice in the Polar Region are weighted down by a factor of one half to cover the surface uniformly with observations. The mean errors of the static topography are twice larger than for the case where data from all over the orbit are used (fig. 4.4). The increase of the mean errors is due to limiting the data results on the bisection of the data set. Approximately only half of the simulations are used to build up the inversion matrix for the spherical harmonic coefficients and the time-dependent variations.

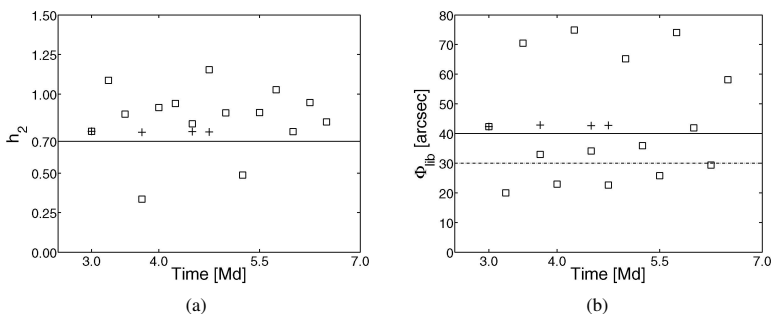


Figure 4.3: Extracted Love number (a) and extracted libration amplitude (b) vs. simulation time for a fixed maximum harmonic degree of inversion $l_{inv} = 16$. \square represent a uniform surface coverage for one Mercury sidereal rotation (Md) of approximately 58 Earth days, while $+$ indicate a uniform weighting over two rotational periods of Mercury (approximately 176 Earth days). Input values are shown by horizontal lines. The dashed line in (b) indicates the initial value used in the first inversion step. The symbols indicate the mean value of the inverted Love number obtained for the 26 noise realizations. The error bars are not shown for emphasizing the effect of the different weighting schemes. The inversion for the libration has been prepared for one single noise model.

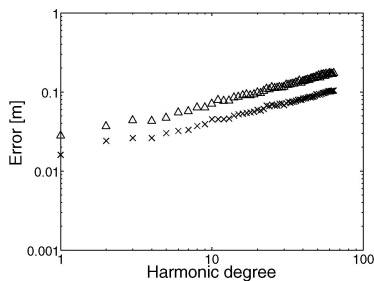


Figure 4.4: Mean errors of the static topography coefficients as a function of harmonic degree for data from all over the orbit (\times), and data limited to spacecraft altitudes up to 1000 km (Δ).

The tidal Love number is extracted with an offset of approximately 6 % and an increased uncertainty of the standard deviation for 26 different noise realizations of approximately a factor of 2. As only half of the data set is used than for all data over the orbit the number of simulation contributing and minimizing the uncertainty are only half. The libration amplitude is extracted with an offset of approximately 10 %. The offsets within the extraction of the time-dependent variations are based on the limitation of the extraction. The main effect of the solar force is present at the equator as Mercury's rotation axis

is perpendicular to its orbital plane. Each surface point is only observed three times after restricting the data to spacecraft altitudes up to 1000 km. The equatorial region is the region where the coefficient C_{20} , C_{22} , and S_{22} have the largest effect. These coefficients affect mostly the analyses of the tidal Love number.

The libration amplitude is extracted in a second step. As the coefficients of the static topography and the tidal Love number are inverted in the first inversion (sec. 4.2.1) and then used as approximated values for the determination of the libration amplitude, the

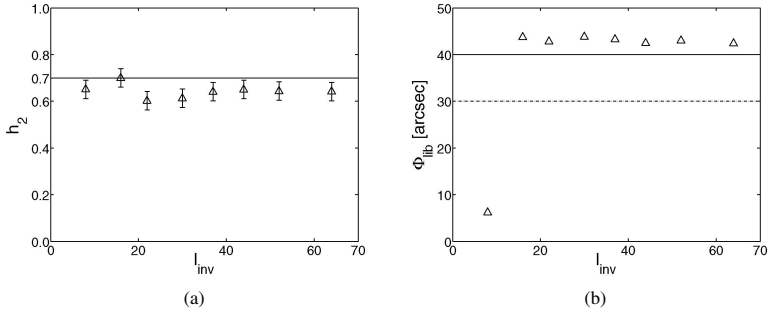


Figure 4.5: As fig.4.2 for data limited to spacecraft altitudes up to 1000 km.

uncertainties retrieved for the coefficients of topography and the tidal Love number affect directly the uncertainties of the libration amplitude. As the values for the coefficients, the tidal Love number, and the libration amplitude converge quickly, almost no improvement is possible in the second iteration.

The values of the time-dependent variations improve by multiplying with an additional factor. Then all regions of the surface are equally covered with simulations. Without weighting, the criteria of orthogonality are not true and the inversion matrix turns into a full matrix with correlations between the different coefficients. The correlations in general vanish due to the orthogonality of the different coefficients. The orthogonality of the spherical harmonic coefficients is realized by adopting the weighting scheme. The following simulations use the weighting scheme, where the surface is uniformly weighted over the tidal cycle of 2 Mercury years.

It has to be remarked that the optimum weighting scheme has only been computed for a single topography realization. In the following the improvements of the weighting scheme are used for the investigation of different topography models. Different topography models show that here only a special case was investigated. Thus it is improved in the following, where the optimized weighting scheme will be used. Optimizing the weighting scheme is done by:

- using a nearly uniform weight of the surface with observations.
- multiplying by an additional factor to simulate nearly uniform surface coverage of Mercury for a 2-years-cycle of Mercury.

- weighting down areas which are observed twice in order to simulate a nearly uniform surface coverage.

This leads in general to a *nearly uniform surface coverage of the surface over a complete 2-Mercury-years-cycle*.

4.4 Orbit selection and its effect on the retrieved topography

In a second set of simulations, the effect of the particular choice for the spacecraft orbit (hence the detailed distribution of laser foot points) and of data gaps on the precision of the inversion are tested. Data for 4 Mercury years, i.e. the nominal duration of the BepiColombo mission, have been used. As outlined in sec. 3.2, simulations for a resonant orbit with 910 orbital periods of the spacecraft corresponding to exactly one Mercury year are compared to simulations for a realistic non-resonant orbit. In the latter case, arbitrarily 909.234 orbital periods in one Mercury year are taken. In a third step, the restriction of a non-resonant orbit is augmented by the fact that no data are obtained from spacecraft altitudes above 1000 km (sec. 4.3.2). In the latter case, the density of measurements in two calottes around the North and South pole of Mercury is twice as high as in the equatorial regions. The latter applies for the idealized situation that the perihelion of MPO's orbit stays exactly above Mercury's equator during the whole mission duration (sec. 3.2). To simulate uniform spatial coverage, the weights for the measurements falling into these calottes have been reduced by a factor of 2. The results for 20 different synthetic models of Mercury's static topography are calculated as outlined in sec. 3.1 for all cases. A single noise realization has been used. The mean error for the recovered Love number and libration amplitude is then determined by

$$\Delta h_2 = \sqrt{N_{\text{sim}}^{-1} \sum_{i=1}^{N_{\text{sim}}} (h_{2,\text{inv}}^i - h_2)^2}, \quad (4.8)$$

where h_2 is the input value of the Love number and $h_{2,\text{inv}}^i$ is the extracted Love number for the i -th of the $N_{\text{sim}} = 20$ different topography models. The mean error of the libration amplitude $\Delta \Phi_{\text{lib}}$ is defined in the same way. The investigation are further extended to also analyze different realizations of the libration amplitude.

Figure 4.6 shows that the degree error eq. (4.7) of the topography coefficients up to degree 64 is at the level of 1-20 cm. The differences between the resonant and the non-resonant orbit with measurements restricted to 1000 km is larger by a factor of 2.

For a resonant orbit and full data coverage, it can be found that the mean error of the Love number h_2 at low inversion degrees for the static topography is larger considering the 20 different topography models (fig. 4.7a), compared to the results in sec. 4.3 for a single topography model (and only different noise realizations, fig. 4.2). Obviously, the topography model which was created before leads to a good agreement for the Love number. At high inversion degrees, the average error value becomes small. The slight offset of the error bars from $h_2 = 0.7$ indicates a weak bias of the inverted Love number towards lower values. For the libration amplitude, the error remains somewhat larger even

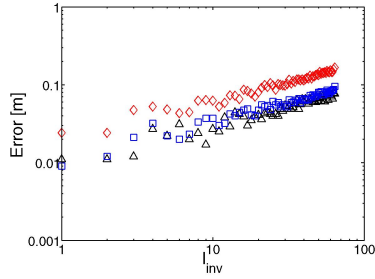


Figure 4.6: Mean errors of the static topography coefficients as a function of harmonic degree for a resonant spacecraft orbit (Δ), a non-resonant orbit (blue \square), and a non-resonant orbit with data limited to spacecraft altitudes up to 1000 km (red \diamond).

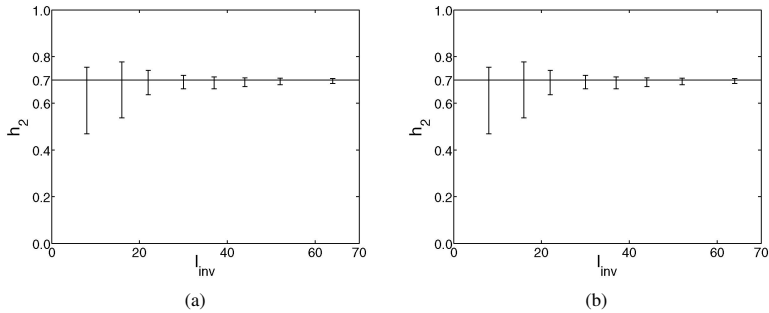


Figure 4.7: Results for the Love number (a) and libration amplitude (b) vs. maximum harmonic degree of inversion for a resonant spacecraft orbit and data returned from all altitudes. The size of the error bars indicates the 2σ deviation from the input value obtained for different topography models. The error bar is centered at the mean inverted value.

at high inversion degrees, but also here a trend of decreasing error with increasing degree of inversion can be found.

Compared to the case of a resonant orbit, the error in the Love number at high inversion degrees becomes larger for a non-resonant orbit (fig. 4.8a) and increases further when the data coverage is limited to those parts of the orbit where the spacecraft is less than 1000 km above the planet's surface (fig. 4.8b). In the last and most realistic case Δh_2 drops to 0.036 at $l_{inv} = 64$, meaning a 2σ -uncertainty of 10 %.

In contrast to the error of the Love number that for the libration amplitude is hardly dependent on the different scenarios for the orbit and the data coverage that have been studied (compare figs. 4.7b and 4.8c). Here the 2σ -error at the maximum applied inversion degree is approximately 5 arcsec.

The tidal Love number h_2 is determined with an uncertainty of less than 10 % at

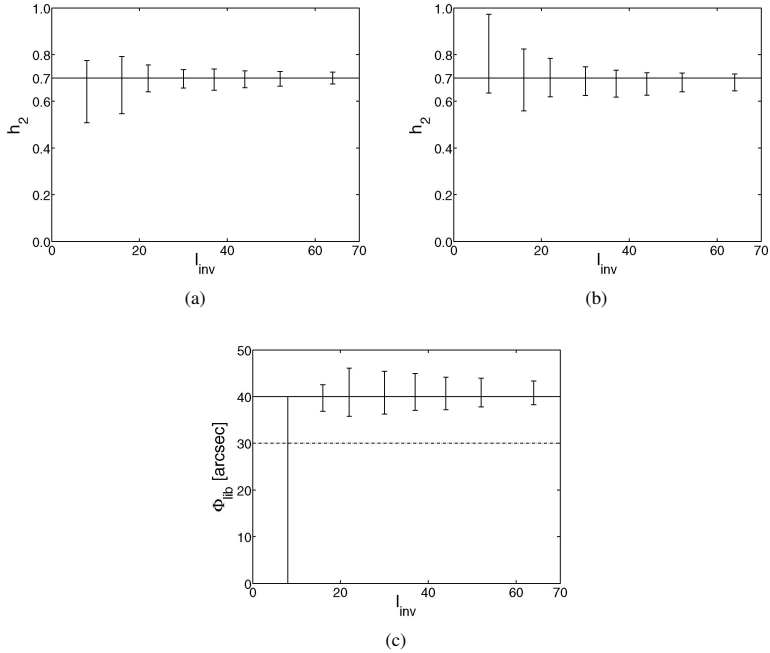


Figure 4.8: As Fig.4.7 for a non-resonant orbit. Error is shown in the Love number for full coverage (a) and when data are limited to a maximum spacecraft altitude of 1000 km (b). The error for the libration amplitude is shown in (c) with an altitude restriction to 1000 km.

the 2σ -level. If Mercury's core is partly liquid, this will allow to determine the core radius within 75 km according to the results by Van Hoolst and Jacobs (2003). The uncertainty of the determination of the libration amplitude of 5 arcsec (12 %) which is more than but still comparable to the measurement precision achieved with ground-based radar interferometry (Margot et al. 2007). The simulations suggest that the error in the Love number h_2 and the libration amplitude Φ_{lib} decreases roughly as $l_{inv}^{-2/3}$ if the maximum harmonic degree of inversion is increased roughly. A more accurate determination of the libration amplitude might be possible by tracking landmarks with an onboard camera (SYMBIO-SYS in case of the BepiColombo mission, Capaccioni et al (2005)), or an improvement might be possible by combining the imaging data with those from laser altimetry.

4.5 Precision of the extracted Love number and libration amplitude

Further a regression of the retrieved uncertainties of sec. 4.4 is computed, where different orbits and data restriction are analyzed. Section 4.4 showed that the uncertainty of the tidal Love number depends on the chosen orbit and the number of measurements. The number of simulated measurements decreased by about a factor of 2, when measurements are restricted up to 1000 km spacecraft altitude.

Plotting the errors in logarithmic scale for the inverted Love number and libration amplitude against the maximum degree of inversion of the static topography l_{inv} looked as there is a linear dependency between the errors for the time-dependent topography variations and l_{inv} (Fig. 4.9, symbols). The scaling seems to follow a power law with the maximum inversion degree, which can be described by

$$(\Delta h_2, \Delta \Phi_{lib}) = a l_{inv}^b. \quad (4.9)$$

Niemeier (2002) describes the computation of a regression in more detail. Only the main parts of the derivation will be summarized. The functional model is

$$(\Delta h_2, \Delta \Phi_{lib}) = a_0 + b l_{inv}, \quad (4.10)$$

where the more general equation is adopted to the used variable names. The transformation of Eq. (4.9) to (4.10) is easily done by computing in logarithmic space. $(\Delta \mathbf{h}_2, \Delta \Phi_{lib})$ are the observation vector, and \mathbf{l}_{inv} the parameter vector. The stochastic model is assumed to be uncorrelated and with an equal weight of one so that the stochastic matrix is the

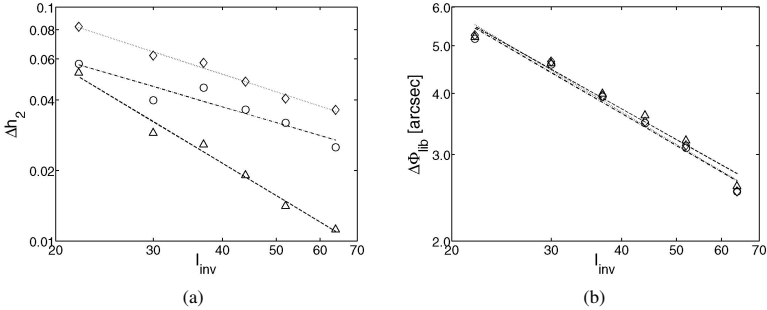


Figure 4.9: Errors of the tidal Love number (a) and the libration (b) according to eq. (4.8) vs. harmonic degree of inversion for a resonant spacecraft orbit (Δ), a non-resonant orbit (\circ), and a resonant orbit with data limited to spacecraft altitudes up to 1000 km (\diamond). The lines represent the results of linear regressions.

unity matrix. The design matrix A can be written as a two-dimensional vector containing the following values

$$A_i = [1 \quad (\Delta h_{2,i}, \Delta \Phi_{lib,i})]. \quad (4.11)$$

The normal equations are then

$$\mathbf{N} \hat{\mathbf{b}} = \mathbf{n}, \quad (4.12)$$

where $\mathbf{N} = (\mathbf{A}^T \mathbf{A})$ is the normal matrix and $\mathbf{n} = \mathbf{A}^T \mathbf{l}_{inv}$ the normal vector. A quantity for describing how well the retrieved parameters fit to the input values can be described by the regression coefficient which is determined as

$$B = \frac{\mathbf{b}^T \mathbf{n}}{(\Delta \mathbf{h}_2, \Delta \Phi_{lib})^T (\Delta \mathbf{h}_2, \Delta \Phi_{lib})}, \quad (4.13)$$

where B must be between 0 and 1. For a value of 1 the regression fits well to the defined model, while for $B = 0$ the model does not fit the data.

The retrieved functions are plotted as a straight line in logarithmic scale in fig. 4.9 for the inverted Love number and libration amplitude against the maximum degree of inversion of the static topography l_{inv} . In all studied scenarios for the orbit and data coverage, the value for the errors of the tidal Love number Δh_2 or the libration amplitude $\Delta \Phi_{lib}$, respectively, scale as a power law with the maximum inversion degree described in eq. (4.9). All regressions have a correlation coefficient larger than 0.99 for $l_{inv} > 22$. The limitation was included as the behavior for values of l_{inv} smaller than 22 is not completely understood..

The decrease of the error in the tidal Love number (fig. 4.9a) is strongest for the case of a resonant spacecraft orbit, with an exponent of $b = -1.42$, while for the non-resonant orbit the decrease is weaker, with an exponent $b = 00.69$ and -0.76 for the case of full data coverage and the case of data limited to spacecraft altitudes up to 1000 km, respectively. The error of the libration amplitude decreases with an exponent of about $b = -0.66$ for all scenarios (fig. 4.9b). These results suggest that even more precise information on the time-dependent topography can be retrieved if the inversion are prepared for harmonic degrees of the static topography larger than 64 (Koch et al. 2008). At present, the static topography cannot be described for larger degrees because the computational effort increases exponentially. A more detailed discussion is given in ch. 8.

5 Extraction of the static and time-dependent topography by a local basis function expansion

One of the primary goals of the BepiColombo laser altimeter (BELA, sec. 2.3.5) is the extraction of Mercury's tidal signal. For a precise determination of the tidal Love number h_2 , the time-dependent tidal elevation needs to be distinguished from the static topographic elevation. Therefore, Mercury's static topography always needs to be extracted simultaneously with high precision as a by-product of a precise determination of the tidal elevation due to solar gravitation.

In the previous section, the static topography was expressed as a spherical harmonic expansion. The normalized spherical harmonic functions are global basis functions. The extracted topography of Mercury is determined by a set of coefficients C_{lm} and S_{lm} (sec. 3.1). The computation of the design matrix is time-consuming because contributions to all design matrix elements must be calculated for each subsequent measurement location. This means, that for each of the 152 million measurements of order $(l_{inv} + 1) \times (l_{inv} + 1)$ corresponding calculations must be performed (sec. 4.2).

Therefore, an alternative approach with local basis functions is explored. The surface of Mercury is covered with a grid containing approximately 4.7 million cells. The extracted output topography grid either has the same grid resolution as the synthetic input topography or points are combined. On each cell, a set of local basis functions such as simple step functions, linear functions ("hat" function), or cubic splines are used. Step functions are localized to one particular cell, where the value is one, and zero otherwise. The linear and cubic functions are localized to only a few grid cells. The static topography is expanded into these local basis functions, i.e. each measured topography value is expressed as a linear combination of the local basis functions. For step functions, only a single coefficient describes a particular topography measurement because it can be associated with a particular grid cell. In case of the linear and cubic spline functions, only a few coefficients are needed to describe a measurement because only a few local basis functions are non-zero at the location of the measurement. The coefficients are determined by a least-squares inversion of the local basis function expansion to the measured topography values with the same algorithm for the inversion of the design matrix as used for the spherical harmonic expansion. The big advantage of the local basis function approach is that for each subsequent measurement point, only a small number of contributions to the small number of elements of the design matrix must be calculated. This significantly increases the computational speed of this method.

The synthetic data are simulated in the same way as for the method applying global basis functions (sec. 3.2 and 3.3) and the same deterministic topography model as described in sec. 3.1. The approach will be specified in more detail in the following sections. The mathematics which is used for building-up the inversion matrix are explained in more detail as well as the method to solve the inversion by a Gaussian elimination (sec. 5.2.2). With this approach, the tidal Love number is simultaneously extracted. Then the best resolution of the grid shall be investigated. This will be performed analytically, sec. 5.3.1. Analyses with global basis functions showed a large dependency on the weighting scheme and on data restrictions. Different weighting schemes are also tested for the approach with the local basis functions. Furthermore, the topography is transformed into a spherical harmonic expansion. For a simultaneous analysis of the long-wavelength topography and gravity field, both must be expressed by a spherical harmonic expansion to be correlated to each other. This gives deeper insight into the differentiated interior of Mercury.

5.1 Introduction into the extraction by local basis function expansion

The analysis methods for MOLA were provided and published by Abramov and McEwen (2004). They used a Delaunay triangulation for expressing the topography. Here, the analysis method uses a global rectangular grid as topography description, where the basis functions of the grid points are only locally non-zero around the grid points surrounding the laser shot. A Delaunay triangulation of the observations for the BELA data set would give a bad distribution of the triangles. Furthermore, the tidal elevation is included as an additional parameter which shall also be extracted accurately. The extraction of the tidal elevation has in fact higher priority. The static topography has to be extracted for a precise determination of the tidal elevation change, although it is rather a by-product. In the following, the topography will be expressed by a rectangular grid. The measured topography values at the locations of the different laser shots will determine the topography values at the grid points. Each measured topography value will be decomposed into a few coefficients belonging to the few non-zero local basis functions in the neighborhood of the measurement location. The set of basis functions are equivalent for all grid points, i.e. their coordinates are relative to one central grid point.

Here, it will be investigated how precise the tidal Love number h_2 and also the topography as a kind of by-product can be retrieved by using local basis functions. The majority of grid points are not affected by each subsequent laser altimeter measurement. Only the area close to the laser shot is affected. This is opposite for the global basis functions where the topography is expressed as a spherical harmonic expansion (ch. 4). For computing the influence of a laser shot onto the grid point, three functions are used: 1) step functions which can be described as the closest neighboring point, 2) linear functions, and 3) cubic spline functions. For the step functions, one could also use the natural neighbor, i.e. the neighbor which is closest in its topography value but not closest in distance (Abramov and McEwen 2004). However, this would need more effort and information to implement because several neighboring points have to be analyzed for each measurement, and an approximate topography model must be known as a priori information.

As a first approach simplifications are introduced. In latitudinal direction only step

functions are chosen. The laser shots are separated by at most 300 m in low latitudes if the shot frequency is 5 Hz. Therefore, many measurements fall into one grid cell and the corresponding coefficient can always be determined. The choice of step functions in latitudinal direction has the advantage that the design matrix has a band structure which facilitates the inversion. In longitudinal direction, the laser shots could be separated by several kilometers in the equatorial region of Mercury depending on the chosen orbit for the simulations. Therefore, linear and cubic spline basis functions are also implemented for the longitudinal direction with the aim to "bridge" badly covered areas. The three mentioned types of basis functions are described in more detail in sec. 5.2.1.

The algorithm of inversion is implemented as a Gaussian elimination of the inversion matrix (sec. 5.2.2). The inversion results in all coefficients for each grid point necessary to describe the static topography value of this grid point and in the tidal Love number h_2 . The triangulation of the inversion (design) matrix can be computed using arrays of the full matrix because of its band structure. Restrictions of the analysis due to using only step functions in latitude direction have not been found, but this has to be investigated in the future in more detail. Due to MPO's polar orbit around Mercury with limited number of orbits covering the surface and crossing the equator, restrictions arise for interpolating the laser shots on grid points in the equatorial region. In order not to include aliasing artifacts, the determination is limited to special cases (sec. 5.3.1).

The computation time mainly depends on the number of laser shots and the running-time of the program for generating the input topography. The setting-up of the input topography, generation of the laser shots itself, and the sources of noise are implemented in the same way as in ch. 4, and are explained in ch. 3. While the simulations based on global basis functions for the extraction used the long-wavelength coefficients of Moon's topography up to degree and orders 16, the coefficients of the synthetic topography for the method based on local basis functions are generated completely randomly for all spherical harmonic degrees.

Analytical investigations are prepared whether there is an ideal combination of the data for the output topography (sec. 5.3.1). The binning is expressed by factors describing the resolution of the input topography compared to the resolution of the output grid. If the number of grid points for the input topography is $ni = 1.5 l_{max}$ in latitudinal direction and $nj = 2 ni$ in longitudinal direction, and for the output topography it is $nlong$ in longitudinal direction $nlat$ in latitudinal direction, the factors are defined as

$$i_{long} = \frac{nj}{nlong}, \quad (5.1)$$

$$i_{lat} = \frac{ni}{nlat}. \quad (5.2)$$

5.2 Inversion method

The extraction of the coefficients which describe the decomposition of all the topography values at the different grid points into the local basis functions is obtained by a least-squares inversion to the measurement data. The design matrix elements are given by products of the local basis functions in a similar way as in the case of using global basis functions. However, the computation of the inversion matrix is much simpler as will be

seen in sec. 5.2.1. A similar normal equation

$$\mathbf{Ax} = \mathbf{b}, \quad (5.3)$$

has to be inverted where \mathbf{A} is the design matrix, \mathbf{b} the right-hand-side vector containing the measured topography values and the tidal Love number a priori, and \mathbf{x} is the result vector of the coefficients of the basis functions. These coefficients are the topographic values at the grid points itself for step functions and linear functions, while some simple calculation needs to be done in the case of the cubic spline functions to derive the measured topography values at the grid points (sec. 5.2.2). The inversion of the matrix is based on a triangulation and is described in sec. 5.2.2.

5.2.1 Local basis functions defined on topographic grid cells

The local basis functions are defined as functions of local coordinates relative to certain grid points. For each topographic measurement, the next neighboring grid point to the respective laser shot must be determined. The interval where the laser shot is located is computed in two steps. First the position in latitude direction is computed and secondly the position in longitude direction. In latitude direction only step functions are used due to the high density of laser shots along the spacecraft track. The width of an interval to which a laser shot has to be assigned is given by

$$\Delta\theta = \frac{\pi}{nlat}, \quad (5.4)$$

where $nlat$ is the number of grid points in latitude direction. The distance between longitudinal points can similarly be computed to

$$\Delta\lambda = \frac{2\pi}{nlong}, \quad (5.5)$$

where $nlong$ is the number of grid points in longitude direction. $nlong$ and $nlat$ are defined by equations (5.1) and (5.2), respectively.

The numbering of the grid in latitudinal direction is given by

$$i_k = INT\left(\frac{nlat}{\pi}\theta_k\right), \quad (5.6)$$

where θ_k is the co-latitude of the k th laser record. The determination of the longitudinal position has been separated into two parts. The first belongs to the step functions as longitudinal basis functions (eq. 5.7), where the second is used for the linear and cubic spline basis function (eq. 5.8)

$$j_k = INT\left(\frac{nlong}{2\pi}\lambda_k + 0.5\right) + 1, \quad (5.7)$$

$$j_k = INT\left(\frac{nlong}{2\pi}\lambda_k\right) + 1, \quad (5.8)$$

where λ_k is the longitude of laser record k . The position to which a laser shot is assigned in the design matrix is given by

$$n_k = j_k + nlong i_k. \quad (5.9)$$

This order results in a matrix with band structure if only step functions are used as basis functions in latitudinal direction. The band structure facilitates the triangulation and therefore the inversion of the normal equation. For the analysis of the tidal Love number, one row and one column have to be added.

Once the correct grid cell into which a laser shot falls is determined the values of the local basis functions at the location of the laser shot must be calculated to build-up the inversion matrix. In latitudinal direction only step functions are used, so that it is sufficient to know the correct interval into which the laser shot falls (eq. 5.6). The step function tr_{i_k} is simply 1, if the grid line i_k is the next latitudinal neighbor to the k th laser shot, all other latitudinal step functions are zero at the location of laser shot k :

$$tr_{step,i_k} = 1. \quad (5.10)$$

The same applies for the longitudinal step function:

$$tr_{step,j_k} = 1. \quad (5.11)$$

For the higher order basis functions (linear functions and cubic spline functions), the local coordinate in longitudinal direction is defined as

$$x_{j_k} = \frac{\delta\lambda_k}{2\Delta\lambda}, \quad (5.12)$$

with

$$\delta\lambda_k = \lambda_k - j_k \Delta\lambda, \quad (5.13)$$

where j_k is the integer such that $j_k \Delta\lambda$ denotes the location of that neighboring grid point to the laser measurement shot k which has smaller longitude than the laser shot k (eq. 5.8).

The linear trial functions used to build up the contribution of laser shot k to the design matrix can be expressed as

$$tr_{lin,j_k} = 1 - x_{j_k}, \quad (5.14)$$

$$tr_{lin,j_{k+1}} = x_{j_k}. \quad (5.15)$$

For all other j the linear trial functions are zero at the location of the laser shot k .

Each cubic spline function extends over four intervals in longitude bounded by five grid points:

$$x_{j_{k-2}} < x_{j_{k-1}} < x_{j_k} < x_{j_{k+1}} < x_{j_{k+2}}. \quad (5.16)$$

The local spline functions which are used to build up the design matrix are defined as

$$tr_{cub,j_{k-1}} = \frac{1}{4} \left(1 - 3x_{j_k} + 3x_{j_k}^2 - x_{j_k}^3 \right), \quad (5.17)$$

$$tr_{cub,j_k} = \frac{1}{4} \left(4 - 6x_{j_k}^2 + 3x_{j_k}^3 \right), \quad (5.18)$$

$$tr_{cub,j_{k+1}} = \frac{1}{4} \left(1 + 3x_{j_k} + 3x_{j_k}^2 - 3x_{j_k}^3 \right), \quad (5.19)$$

$$tr_{cub,j_{k+2}} = \frac{1}{4} x_{j_k}^3. \quad (5.20)$$

The contributions to the design matrix elements from measurements of which locations fall into a certain grid cell n and the respective contributions to the right-hand side vector are given by

$$a_{n,n'} = \sum_{k(n)} w_{k(n)} tr_{step/lin/cub,j_{k(n)}}(x_{k(n)}, t_{k(n)}) tr_{step/lin/cub,j'_{k(n)}}(x_k, t_k), \quad (5.21)$$

$$b_n = \sum_{k(n)} w_{k(n)} T_{k(n)} tr_{step/lin/cub,j_{k(n)}}(x_k, t_k). \quad (5.22)$$

For $n \leq N$ the basis functions $tr_{step/lin/cub,j_{k(n)}}(x_k, t_k)$ are the local basis functions, which are independent of the time of the observation t_k , and $j_{k(n)}$ is the index for the local basis function in longitude direction. The loop over $k(n)$ is limited to the sum over all laser measurements shots that fall within the same grid cell numbered by n . The n' and j' values are related in the same way as n and j . For step functions only one computation with $j' = j$ is required, for linear functions two computations for $j' = j$ and $j' = j + 1$ are needed, and for cubic functions j' runs from $j - 1$ to $j + 2$ which require four computations. The diagonal design matrix element $A_{n,n}$ is given by the above $a_{n,n}$ while for the off-diagonal design matrix elements $A_{n,n'}$ with $n' \neq n$ contributions from measurements of several grid cells have to be summed up. The band structure of the design matrix is obvious from the fact that n' only runs from $n - 1$ to $n + 2$. The design matrix is diagonal so that only the "upper" off-diagonals must be stored. Care must be taken about the so-called wrap-around in longitude. The design matrix has blocks which belong to a fixed latitude with index i . The wrap-around produces design matrix entries in the upper right and lower left corners of these blocks due to the overlap-region close to the 0^{th} meridian.

The design matrix elements with $n = N + 1$ or $n' = N + 1$ the basis function describes the global tidal signal and, therefore, depends explicitly on time, $F_{N+1}(\theta, \lambda, t) = F_{tide}(\Psi)$, where the relation between Ψ and (θ, λ, t) is obtained from eq. (2.22).

Most computational power is needed for generating the input topography models. The time-consuming part of the simulations is the computation of the design matrix and the identification of the exact position within the inversion matrix of the least-squares inversion (n_k). The matrix needs only $2j$ computations for the part of the inversion matrix containing the topography and $j + 1$ computations for the time-dependent part expressed as tidal Love number. This decreases the needed computational power significantly.

Some more explanation is needed for the cubic spline basis functions (Freund and Hoppe 2007). The cubic spline function "belonging" to a grid cell n in fact extends over four intervals. The cubic spline functions are identical for all latitudes so that n can be replaced by j in their numbering. Additionally, there is translational invariance in longitude for these spline functions, so that one can in principal skip the index j when numbering the four longitudinal intervals with index $j' = j - 1, \dots, j + 2$. The cubic spline function belonging to grid cell j can be written as

$$S_{j'}(x_{j'}) = a_{j'} + b_{j'} x_{j'} + c_{j'} x_{j'}^2 + d_{j'} x_{j'}^3. \quad (5.23)$$

These spline functions have to fulfill the following criteria:

- continuity $S_{j'}(1) = S_{j'+1}(0)$,
- twice continuous differentiable $S'_{j'}(1) = S'_{j'+1}(0)$ and $S''_{j'}(1) = S''_{j'+1}(0)$ for all three interval boundaries.

This gives nine conditions. Five more conditions are obtained by

1. $S''_{j-2}(0) = S_j + 2''(1) = 0$,
2. $S_{j-2}(0) = S_j + 2(1) = 0$,
3. $S_j(0) = 1$.

These yield

$$S_{j-1}(x) = \frac{1}{4}x^3, \quad (5.24)$$

$$S_j(x) = \frac{1}{4}(1 + 3x + 3x^2 - 3x^3), \quad (5.25)$$

$$S_{j+1}(x) = \frac{1}{4}(4 - 6x^2 + 3x^3), \quad (5.26)$$

$$S_{j+2}(x) = \frac{1}{4}(1 - 3x + 3x^2 - x^3). \quad (5.27)$$

(5.28)

One local cubic spline basis function assigned to longitudinal grid point j is given by the set of four functions $S_{j-1}(x) =: S_{j,j-1}(x)$, $S_j(x) =: S_{j,j}(x)$, $S_{j+1}(x) =: S_{j,j+1}(x)$, and $S_{j+2}(x) =: S_{j,j+2}(x)$ which are piecewise defined on the intervals $[x_{j-2}, x_{j-1}]$, $[x_{j-1}, x_j]$, $[x_j, x_{j+1}]$, and $[x_{j+1}, x_{j+2}]$, respectively.

If a laser shot falls into the interval between $x_j = 0$ and $x_j = 1$, there are four local cubic spline basis functions which are non-zero. These are given in eq. (5.17) to (5.20).

5.2.2 Gaussian elimination of the inversion matrix with band structure

The method of the Gaussian elimination is an efficient algorithm for solving a system of linear equations in algebra. The algorithm is named after Carl Friedrich Gauss who firstly investigated this method and published it in 1809. The main goal of the method is the transformation of a given matrix to an upper triangle matrix with similar changes of the right-hand side vector which contains here the topography values for the interpolated laser shots of the whole data set. The process can be divided in two parts. First the matrix is changed to an upper triangle matrix and the right-hand-side vector is adopted at the same time (*forward elimination*). Second the solutions are computed row by row (*backward substitution*). The forward modeling applies matrix decompositions by the three elementary row operations (multiplying rows, switching rows, and adding multiples of rows to other rows). Here, switching rows is neglected as the elements of each row are set to be a fixed point on the surface. The allocation after switching rows needs lot of effort as each row directly contains the information of the coordinates of the grid points.

Gaussian elimination solves n equations for n unknowns. This requires $n(n+1)/2$ divisions, $(2n^3 + 3n^2 - 5n)/6$ multiplications, and $(2n^3 + 3n^2 - 5n)/6$ subtractions for a total complexity of $2n^3/3$ operations. Its complexity is $O(n^3)$. Due to its simplicity, the algorithm can easily be implemented.

The inversion matrix which has to be transformed for the local basis functions is a band matrix where the majority of the matrix elements \mathbf{A} itself is zero. The building-up of the matrix for step functions gives a diagonal matrix, for linear interpolation a band matrix with one additional outer column and an additional element for the overlap in the longitudes at zero longitude, and for the cubic spline interpolation a band matrix with three additional outer columns and additional elements for the overlap at zero longitude. The matrix is stored band by band due to the interpolation in latitude direction. The elements in latitude direction do not affect each other. An adoption due to the usage of linear interpolation and cubic spline interpolation in latitude direction is not prepared right now. All cases contain an additional row and column considering the effect of the tidal Love number h_2 . The additional row has to be eliminated while the matrix is triangulated for the simultaneous analysis.

The topography values for the step functions and linear interpolation can be directly retrieved. The matrix contains the coefficients of the interpolation. This has to be taken into account for the cubic spline interpolation where the topographic values are derived by

$$T_{i,j} = \frac{1}{4} x_{i,j-1} + x_{i,j} + \frac{1}{4} x_{i,j+1}, \quad (5.29)$$

where \mathbf{x} is the result vector for the Gaussian elimination containing the coefficients after transformation, i the index for the latitude and j the index in longitude direction.

5.3 Optimization of data binning and weighting scheme

The spatial resolution of the BELA topography measurements is given by the distance $\Delta\lambda_{st}$ between laser tracks in longitudinal direction. Presumably it will not make much sense to choose the output grid cell dimension in longitudinal direction much smaller than the value $\Delta\lambda_{st}$. On the other hand, information will be lost, if the output grid cell dimensions are larger than $\Delta\lambda_{st}$.

The input grid cell sizes have been chosen to be somewhat smaller than $\Delta\lambda_{st}$. Therefore, the modeled input topography has more detail than can be measured by BELA. This ensures that the quality of data extraction can actually be verified by comparing the output topography with the input topography (sec. 5.3.1). In the following, it will be derived analytically that the optimum binning is achieved when the rectangular output grid cells have approximately the dimension $\Delta\lambda_{st}$.

It will further be shown that no improvement of the analysis can be achieved by using an optimized weighting scheme. This is in contrast to the analyses with global spherical harmonic basis functions, where the effect of different weighting schemes on the precision of topography extraction was large (sec. 4.3).

5.3.1 Analytical determination of the optimum combination of grid points

The analytical determination first needs the definition of some variables. The equator length U_M is computed from the planetary radius a of Mercury:

$$U_M = 2\pi a = 15,330.97 \text{ km}. \quad (5.30)$$

Using n_j and n_i for the number of input topography grid points in longitude and latitude, respectively, and n_{long} and n_{lat} for the respective number of output topography grid points, the size of grid cells in longitudinal and latitudinal direction can be calculated as

$$\Delta\lambda_l = \frac{U_M}{n_j}, \quad (5.31)$$

$$\Delta\lambda_o = \frac{U_M}{n_{long}} = i_{long} \frac{U_M}{n_j} = i_{long} \Delta\lambda_l \quad (5.32)$$

$$\Delta\theta_l = \frac{U_M}{2n_i}, \quad (5.33)$$

$$\Delta\theta_o = \frac{U_M}{2n_{lat}} = i_{lat} \frac{U_M}{2n_i} = i_{lat} \Delta\theta_l, \quad (5.34)$$

where $\Delta\lambda_l$ is the distance between grid points for the input topography in longitude direction and $\Delta\theta_l$ in latitude direction, while $\Delta\lambda_o$ and $\Delta\theta_o$ are the respective distances of the output topography.

The distance between laser tracks $\Delta\lambda_{st}$ is estimated from the number of satellite tracks (st) that the Mercury Planetary Orbiter (MPO) of the BepiColombo mission leaves on the planetary surface within 1 Mercury year on its near-polar orbit:

$$\Delta\lambda_{st} = \frac{U_M}{st}. \quad (5.35)$$

The realistic case is assumed that BELA measurements can only be taken at spacecraft altitudes below 1000 km. To facilitate the estimates it is assumed that only measurements can be taken on the tracks from South to North pole but not from North to South pole. This means that the number of laser tracks left on Mercury's surface approximately equals the number of orbits.

The distances $\Delta\lambda_{st}$ for three possible orbits which are investigated here are listed in tab. 5.1.

Table 5.1: List of distances between satellite tracks for different orbits according to eq. (5.35)

st	$\Delta\lambda_{st}$ [km]
909.234	16.861
909.750	16.852
910.000	16.847

The latitudinal spacing of laser shots is determined by the shot frequency (sf) which is assumed to be 5 Hz in average. This gives a latitudinal distance $\Delta\theta_{sf}$ in the equatorial region of Mercury between laser shots of

$$\Delta\theta_{sf} = 0.3 \text{ km}. \quad (5.36)$$

A general relation between i_{long} and i_{lat} can be derived from the requirement that the topographic grid should be suitable for transformations into spherical harmonic expansions.

According to the Nyquist theorem, it is necessary that $nlat \geq nlong/2$, if aliasing should be avoided for transformations to high degrees. For the input grid, we have $n_j = 2 n_i$. Consequently, it is required that

$$i_{lat} \leq i_{long}. \quad (5.37)$$

5.3.1.1 Input and output specifications

The input topography has 3072 grid points in longitude direction (n_j) which are separated by $\Delta\lambda_I \approx 4.991$ km, and 1536 grid points in latitude direction (n_i) which are separated by 4.991 km as well. The resolution of the output topography is given in tab. 5.2 for the longitudinal and latitudinal parameters.

Table 5.2: Specifications for the output topographic grid in longitude direction

$i_{long} = i_{lat}$	$nlong$	$nlat$	$\Delta\lambda_O$ [km]
1	3072	1536	4.991
2	1536	768	9.981
4	768	384	19.962
6	512	256	29.943
8	384	192	39.924

5.3.1.2 Longitudinal limitations

The output grid resolution will usually not be chosen to be higher than the input grid resolution. This is equivalent with the condition

$$i_{long} \geq 1. \quad (5.38)$$

For a precise extraction of the Love number, it can be advantageous not to apply any binning, i.e. $i_{long} = 1$. This leaves “white” areas in the output topography, but this leads to a more accurate extraction of the Love number h_2 . Then the grid points, which are not affected by laser shots, are not used for the analysis, but the other grid points contain more information. Furthermore, it is advantageous not to choose i_{long} larger than 4 because topographic information may be lost if the longitudinal output grid length is larger than the typical distance between laser tracks $\Delta\lambda_{st}$ (tab. 5.2)

$$\begin{aligned} \Delta\lambda_O &\leq \Delta\lambda_{st} \approx 4 \Delta\lambda_I \\ i_{long} &\leq 4. \end{aligned} \quad (5.39)$$

This limitation of the longitudinal coverage is based on the orbit of MPO.

5.3.1.3 Estimate of the optimum longitudinal binning

An additional parameter ν is introduced which describes how many output grid points are affected by a laser altimeter measurement at a certain location. ν is 1 for using step

functions in longitude, ν is 2 for linear functions, and $\nu = 6$ for cubic spline functions. The longitudinal distance L_O on the output topographic grid which is affected by a laser shot can be written as

$$L_O = \nu \Delta \lambda_O = \nu i_{long} \Delta \lambda_I. \quad (5.40)$$

If a measured topographic value should be assigned to each of the output grid points in longitudinal direction, the following relation must hold

$$\begin{aligned} \Delta \lambda_{st} &\approx \nu \Delta \lambda_O \\ i_{long} &\approx \frac{n j}{\nu st}. \end{aligned} \quad (5.41)$$

Then the next larger integer value for i_{long} in the case of step functions ($\nu = 1$) can be determined to

$$i_{long} \approx 4. \quad (5.42)$$

For the linear functions ($\nu = 2$) this leads to

$$i_{long} \approx 2, \quad (5.43)$$

and for the cubic spline functions ($\nu = 6$) to

$$i_{long} \approx 1. \quad (5.44)$$

5.3.1.4 Latitudinal limitations

The lower boundary of i_{lat} depends on the number of laser shots (eq. 5.36) in latitudinal direction which is large due to MPO's orbit and the high repetition frequency of the laser. The latitudinal resolution of the output topography should be equal or smaller than that of the chosen input topography. Therefore the first condition for i_{lat} can be written as

$$i_{lat} \geq 1. \quad (5.45)$$

The upper limit of i_{lat} can be derived from eq. (5.37) and eq. (5.39) to be

$$i_{lat} \leq 4. \quad (5.46)$$

5.3.1.5 Summary of the retrieved conditions

The retrieved conditions for the simulations (eq. 5.37, 5.38, 5.39, 5.45, and 5.46) can be summarized to

$$1 \leq i_{lat} \leq 4, \quad (5.47)$$

$$1 \leq i_{long} \leq 4, \quad (5.48)$$

$$i_{lat} \leq i_{long}. \quad (5.49)$$

Different combinations of the different factors can easily be found, because a combination of the grid points in latitudinal direction is not very critical due to the small shot point separation $\Delta \lambda_{sf}$. Therefore, only three cases are investigated in more detail where always $i_{lat} = 1$. The factors in longitudinal direction (i_{long}) are chosen to be 1, 2, or 4.

5.3.2 Optimizing the weighting scheme

The weighting scheme for the laser measurement shots took an important role in the direct inversion of the measured topography into global basis functions, i.e. into spherical harmonic functions (ch. 4). The effect of two different weighting schemes which are also used in ch. 4 will be investigated in detail in the following. First no additional weighting is added to the noise of the laser shots (sec. 3.3). Second the laser shots are weighted to simulate a uniform surface coverage over the entire orbit by eq. (4.5). The uncertainty of the tidal Love number (x_{mdim+1}) and the topographic grid points (x_k) for the 22 (N_{sim}) different synthetic topography representations is computed by

$$\Delta x_i = \sqrt{N_{sim}^{-1} \sum_{i=1}^{N_{sim}} (x_{k,inv}^i - x_{i,k})^2}, \quad (5.50)$$

where $x_{i,k}$ is the input value and $x_{k,inv}^i$ the extracted value for the i th topography representation and k th topography grid point. The tidal Love number is chosen to 0.7000.

Based on the analytical results of sec. 5.3.1, the tests are performed for the three cases where $i_{lat} = 1$ and $i_{long} = 1, 2, 4$. The variation of the parameter i_{long} is introduced because the analysis of the tidal Love number is only possible if the static topography is determined precisely. The mean uncertainty at the grid points is computed for all the grid points on which the topographic measurements have an effect. A single measurement may not only affect the central grid point but also neighboring grid points due to overlap of the linear and cubic local basis functions. When no data are available for a grid point, then it is not used for the calculation of the mean uncertainty. The standard deviations of the extracted topography values are determined with respect to the input topography values. This is, of course, only possible at those grid points where the input grid point coincides with an output grid point because the output grid has lower spatial resolution due to the binning by an integer value.

Figure 5.1 does not only show the results for different weighting schemes, but also the results for the restrictions described in sec. 5.4. Figure 5.1 shows eight cases where a non-resonant orbit (909.234 MPO cycles within 1 Mercury year) is used for A to G and a resonant orbit (909.750 MPO cycles within 1 Mercury years which has a resonance after 4 Mercury years) for H. The different cases can be briefly described as:

- analyses of the topographic altitudes at the grid points and of the tidal Love number without restrictions and equal weights (A);
- analysis with weighting uniform surface coverage (analogous to eq. 4.5) and without restrictions (B);
- analyses with altitude restriction where observations can only be taken up to a spacecraft altitude of 1000 km (C);
- similar to C, but with down-weighting the areas in the Polar Regions which are observed twice by a factor 2 (D);
- analyses using equal weights for all data over the orbit, but restricting the simulated mission time to 3.5 Mercury years (E);

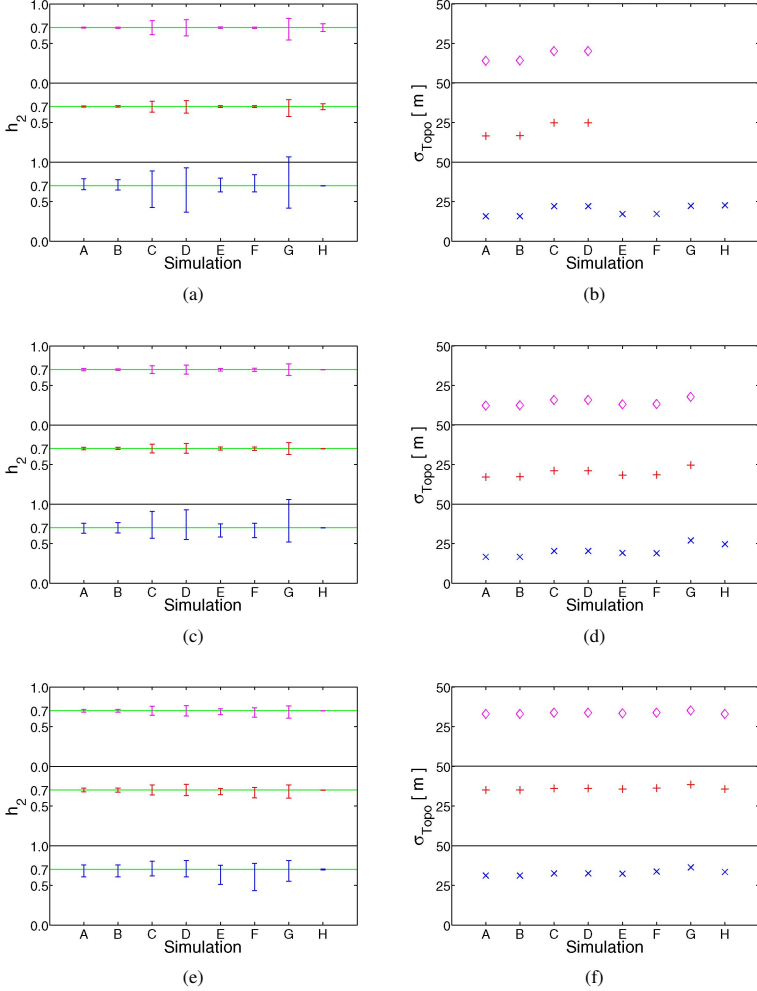


Figure 5.1: Extracted tidal Love numbers (left panels) and mean standard deviations of the topography (right panels) for different resolutions of the output topography: upper row for $i_{\text{long}} = 1$, middle row $i_{\text{long}} = 2$, and bottom row $i_{\text{long}} = 4$. Each panel contains the results of eight different test cases. A non-resonant orbit with 909.234 MPO orbits within 1 Mercury year is used except for case H where a resonant orbit with 909.75 MPO orbits within 1 Mercury year (resonance with 4 Mercury years) is chosen. The different cases A to H are described in the text. The green line in the left panels indicates the chosen input value of 0.7000 for the tidal Love number. The uncertainty is determined from 22 different topography models.

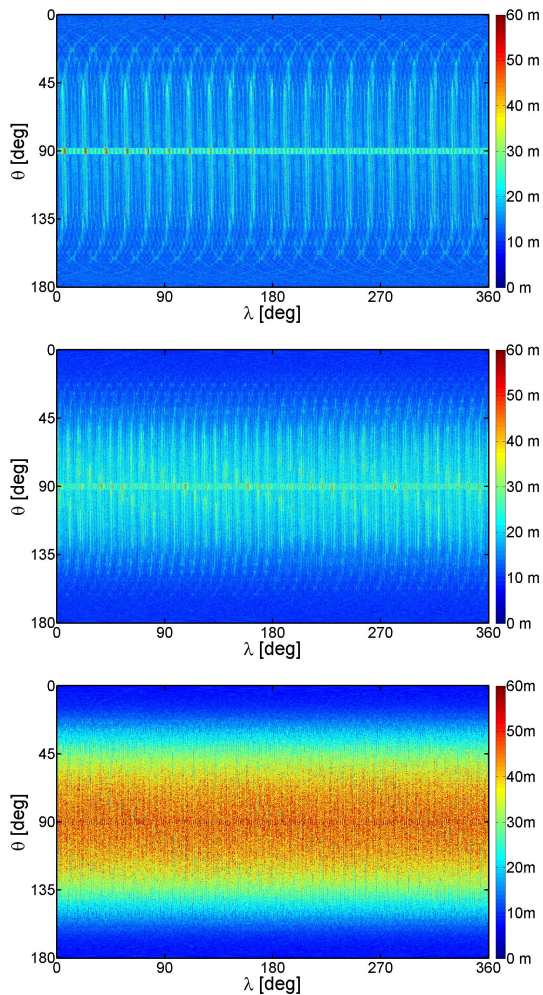


Figure 5.2: Standard deviations of the extracted topography with respect to the input topography for data over the entire orbit without any restrictions. Step functions are used in longitude and latitude direction as local basis functions. i_{long} is chosen to be 1 for the upper panel, 2 for the middle panel, and 4 for the bottom panel.

- similar to E, but using a weighting scheme simulating a uniform coverage of the tidal period of 2 Mercury years (F);
- analyses with an altitude restriction of observations up to 1000 km, data are only simulated up to 3.5 Mercury years, and equal weights are chosen (G);
- analyses for a resonant orbit over 4 Mercury years without including any data restriction (H).

Combining grid points in longitude direction causes an increase in the uncertainty of the tidal Love number. Best results can be obtained when the output and input topographic grid have the same number of grid points. Furthermore, cubic spline functions as local basis functions give marginally better results than the use of linear functions. Step functions have generally worse results compared to other basis functions in longitude direction.

Decreasing the number of grid points by increasing i_{long} causes smoothing of the topography in the equatorial region (fig. 5.2). Best results are obtained for $i_{long} = 2$. Only the plots of the results for step functions as local basis functions in longitude and latitude direction are shown because the results for linear and cubic spline functions look similar. If the input and output topography models are chosen with an equal number of grid points, the spacecraft tracks can be identified in the figures. Step functions in longitude direction have the main advantage that the plotted standard deviations of the grid points directly indicate which parts of the surface are observed or not. None of the used weighting scheme improves the uncertainty of the tidal Love number, neither does the mean uncertainty of the complete topography change (fig. 5.1a and b). The results when using different local basis functions in longitudinal direction did also not show any dependency on different weighting schemes. As the change of the weighting scheme does not result in an improvement of the results as it did in ch. 4, equal weights are chosen for the following tests (sec. 5.4).

The increase of the uncertainty due to the binning of more grid points in longitude direction is caused by the smoothing of the topography. MPO's orbit has a separation of 2 km for its tracks on Mercury's surface at maximum. Furthermore, when more tracks are combined, the tidal signal is also smoothed. It seems that the tidal Love number can only be retrieved precisely, when the topography is also accurately extracted.

The precision of the retrieved topography and the tidal Love number probably cannot be increased by a proper weighting scheme, because the local basis functions have only limited overlap with neighboring basis functions. The improvement in ch. 4 is the result of reducing the quantity of the off-diagonal elements of the design matrix. The weights simulating uniform surface coverage with measurements have the effect that the summation over the products of spherical harmonic functions becomes an approximation to the scalar product between two spherical harmonic functions. Therefore, the outer-diagonal elements of the design matrix tend to be close to zero the more densely the measurements cover the surface. The method using local basis functions does not require the application of such a weighting scheme because the inversion matrix has a band structure which already has very few off-diagonal elements, i.e. most off-diagonal elements are zero anyway. The weighting scheme is further explored with respect to properties other than uniform surface coverage for the cases C, D, E, F, and G, which is investigated in more detail in the following sections.

5.4 Simulations for temporal and spatial data restrictions

After having optimized the binning of the grid points for the output topography (sec. 5.3) and having evaluated different weighting schemes (sec. 5.3.2), the data shall be restricted to more realistic cases. Additionally the very special case of a resonant orbit has been simulated. Four different investigations are carried out: 1) restricting observations to spacecraft altitudes below 1000 km (sec. 5.4.1); 2) a limited observation time which is chosen to 3.5 Mercury years where observations are taken all over the orbit (sec. 5.4.2); 3) limiting the simulation time to 3.5 Mercury years and further including the restriction that observations are only possible for spacecraft altitudes less than 1000 km (sec. 5.4.3); and 4) using a resonant orbit instead of non-resonant orbits without limiting the temporal and spatial data coverage (sec. 5.4.4). The results for the tidal Love number and the mean standard deviation of the extracted topography values with respect to their input topography values are shown in fig. 5.1. There, the mean standard deviations are shown as an average over simulations with 22 different topography realizations. The plots of the standard deviation of the topography in this sec. 5.4 show the results for the case of using step functions and the highest resolution with $i_{long} = i_{lat} = 1$. In this case the areas which are less densely covered with data or even without data can easily be distinguished.

5.4.1 Altitude restriction

Restricting the data coverage to regions where the spacecraft orbit has altitudes less than 1000 km resulted in an increase of the uncertainty (sec. 4.4). An improvement was achieved by down-weighting the area close to the Polar Regions which are observed twice by a factor of 2. Two sets of simulations are performed where the Polar Regions are either down-weighted or not. The results for the tidal Love number are shown in fig. 5.1 in all panels labeled as C and D. The uncertainty of the tidal Love number increases by a factor of at least 10 when the number of grid points of the in- and output topography is equal. When grid points are binned, the increase gets less. For $i_{long} = 4$ the uncertainty increases by a factor of 3. The mean uncertainty of the surface topography shown in the right panels of fig. 5.1 is almost the same in all cases and does not change as much as the uncertainty of the tidal Love number.

The increase in the uncertainty of the tidal Love number is related to the decrease in the number of observations. Rough approximations show that the number of simulations which are used for the analyses are halved. The larger increase for step functions compared to linear and cubic spline functions is related to the effect which the laser shots have. Step functions affect only the neighboring point, while linear and cubic spline function affect more points. The best results with smallest uncertainty of the tidal Love number are obtained when combining two grid points to one for the output topography in longitudinal direction. In that case, the 1σ -standard deviation is 0.05 (approximately 15 % uncertainty for a 2σ -standard deviation) for cubic spline functions. The decrease of the accuracy in the case of the altitude restriction is based on the reduced number of different tidal elevations which are detected. When all data over the orbit are available, the tidal signal is observed 24 times within 4 Mercury years at any location on Mercury's surface. When the altitude restriction is included, the tidal elevation change is only observed 12 times. Due to the non-resonant orbit the maximum number of 24 different tidal changes

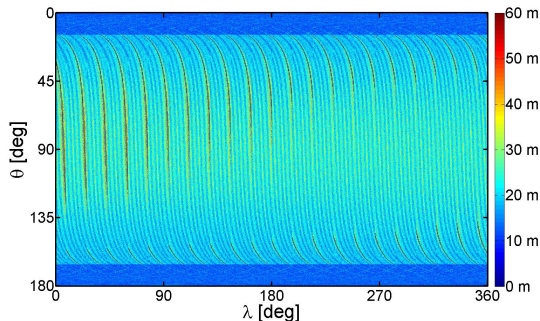


Figure 5.3: Standard deviations of the extracted topography with respect to the input topography for the case of restricting the spatial coverage to locations where the spacecraft altitude is less than 1000 km. Step functions are used in longitude and latitude direction as local basis functions, and the input and output topographic grid are chosen to have the same resolution. Dark colors indicate areas with a lower number of observations or no observations at all.

can in fact not be observed even without altitude restriction; there are only 2 to 3 different tidal phases at a specific grid point. This is close to the limit where aliasing arises. When observing an even smaller fraction of the surface, the results can not be trusted any more.

Figure 5.3 shows the extracted standard deviations for 22 different realizations of the topography when step functions are used as local basis functions in longitude direction. Due to the non-resonant orbit the surface is covered with a rather uniform standard deviation. Restricting the spacecraft altitude nevertheless limits the density of the surface coverage. The mean global standard deviation increases with increasing i_{long} . If i_{long} equals 1 or 2, the mean global standard deviation will be approximately 16 m for linear functions and 13 m for cubic spline functions. If i_{long} is 4, the mean global standard deviation will increase for the different basis functions to more than 30 m. Figure 5.3 also shows the areas where no observations are taken. The areas are related to the pattern of the spacecraft tracks. This is obvious because local basis functions are used.

When the Polar Regions which are observed twice are down-weighted by a factor of 2, the uncertainty of the tidal Love number increases. The topography extraction does not change. Therefore no further plot is shown. As there is no improvement after down-weighting areas which are observed twice, no additional weighting is included in the following simulations.

5.4.2 Temporal restriction

After having investigated a spatial restriction due to the limitation of the data coverage to areas where the spacecraft altitude is below 1000 km, it shall be investigated here, whether and how large a temporal restriction of the data coverage is, i.e. data are taken during 3.5 instead of 4 Mercury years. The temporal restriction mainly has to be understood as a less complete coverage of the tidal phase. It turns out that a shorter time duration does

not affect the determination of the tidal Love number h_2 using the method with local basis functions as much as it did for the method using global basis functions (sec. 5.4.1). The results are plotted as E and F in fig. 5.1. The decrease in accuracy is caused by the

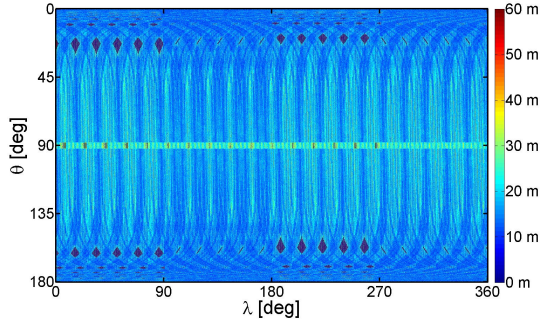


Figure 5.4: Standard deviations of the extracted topography with respect to the input topography when restricting the temporal coverage to 3.5 Mercury years. Step functions are used in longitude and latitude direction as local basis functions. The input and output topographic grids are chosen to have the same resolution. Dark colors indicate areas with a lower number of observations or no observations at all.

decrease in the total number of observations. The uncertainty is only 1.5 times larger than the uncertainty which was retrieved by simultaneous analyses for 4 Mercury years. The retrieved value of the standard deviation of h_2 for the linear and cubic spline functions is about 0.015 (1σ -uncertainty). This is about 5 % for a 2σ -uncertainty, which is a factor of 2 better than the results which are retrieved by a non-resonant orbit for a simulation time of 4 Mercury years (sec. 4.4). It is in the same range as for a resonant orbit when global basis functions expressed as a spherical harmonic expansion are used. Best results for the tidal Love number are obtained for the cases when the output topographic grid has the same resolution, $i_{long} = 1$, or half the resolution, $i_{long} = 2$, of the grid for the input topography. Combining more grid points in longitude direction causes an increase of the uncertainty.

Several areas of the surface are observed less. Transforming 3.5 Mercury years into Mercury's rotation period means that the simulation lasts 5.25 Mercury days. Three quarters of the surface are less observed, shown in brown color. The standard deviation of the topography is still in the same range as without temporal restriction. The increase of the mean standard deviation of the topography due to increasing i_{long} is still present. Adopting the weighting scheme to have an equal coverage on the surface with observations for the tidal cycle of 2 Mercury years does not improve the precision of the tidal Love number. The tidal Love number is even extracted with larger uncertainty. Therefore, no weighting scheme due to temporal restrictions is implemented for the further simulations. The determined standard deviation of the topographic heights with respect to the input topography at the output grid points are plotted in fig. 5.4 for step functions. The plot looks similar for both the weighted and equal-weighted topography extraction. Imprecise

topographic values of the mean standard deviation are assigned to grid points for linear and cubic spline functions, which are excluded for step functions. This makes the mean standard deviation much larger than the chosen range in fig. 5.1b.

5.4.3 Altitude and temporal restriction

In the previous sections the temporal and spatial coverage have been restricted independently. Now, the effect of applying both restrictions together is investigated. The simula-

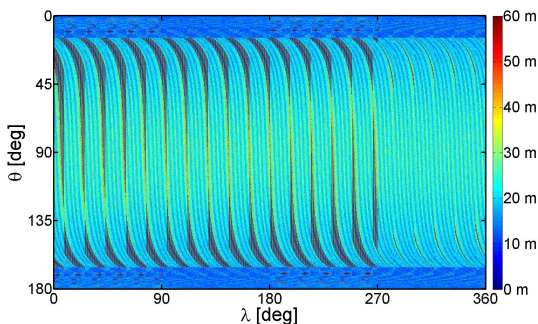


Figure 5.5: Standard deviations of the extracted topography with respect to the input topography when restricting the temporal coverage to 3.5 Mercury years and taking observations only up to 1000 km spacecraft altitude. Step functions are used in longitude and latitude direction as local basis functions, and the input and output topographic grids are chosen with the same resolution. Dark colors indicate areas with a lower number of observations or with no observations at all.

tion time is chosen to be 3.5 Mercury years and the data coverage is restricted to spacecraft altitudes less than 1000 km. The extracted uncertainty of the tidal Love number (case G in fig. 5.1) is slightly larger than for the investigation carried out for the spatial coverage alone. The slight increase is related to the additional restriction of the number of observations. In general, the same effects are found as for the independent investigation of the spatial and temporal coverage. Here, no assumptions of the weighting scheme are made, as it previously turned out that it does not improve the uncertainty of the tidal Love number. The global topography for step functions as local basis functions in longitude and latitude direction is shown in fig. 5.5 for the case when the amount of grid points is equal in longitudinal and latitudinal direction.

5.4.4 Resonant versus non-resonant orbit

The results for the simulations with a resonant orbit (909.750 MPO cycles within 1 Mercury year; resonance with 4 Mercury years) are plotted in fig. 5.1 as case H for the tidal Love number and the global mean topography standard deviation. This orbit is very unrealistic, but it is investigated briefly for comparison to uncertainties retrieved by using

global basis functions (ch. 4). First, it is important to mention that the mean standard deviation of the global topography, which has been chosen as a quantity for the precision of the extracted topography, is outside the usual range for $i_{long} = i_{lat} = 1$ and when using linear and cubic spline functions (fig. 5.1b). When grid points in longitude direction are binned, this quantity decreases. The optimum is expected to occur for $i_{long} = 4$. The

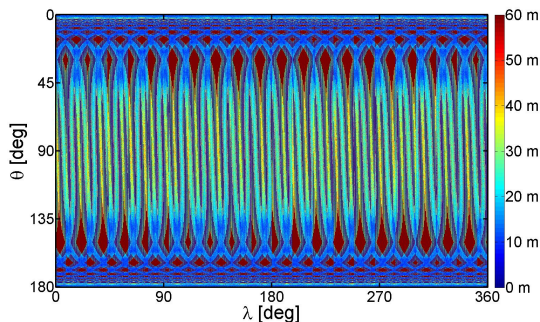


Figure 5.6: Standard deviations of the extracted topography with respect to the input topography for the case of no temporal and spatial restriction but for a resonant orbit with 4 Mercury years (909.750 MPO cycles within 1 Mercury year). Step functions in longitude and latitude direction are used as local basis functions, and the input and output topographic grid are chosen to have the same resolution. Dark colors indicate areas with a low number of observations or no observations at all.

tidal Love number is extracted with an uncertainty $\ll 0.01$, except when linear and cubic spline functions are used for the case of the finest resolution of the output grid (equal to the input topographic grid). These uncertainties are below 5 % with 2σ -uncertainty. The two exceptions shown in the two upper parts of fig. 5.1a arise from the limited coverage of the surface. Due to the resonant orbit several parts of the surface are not observed. Figure 5.6 shows these areas. Between the brown regions where no observations are available, some grid points with topographic altitudes are present, but the majority of them in these regions is hard to determine. A resonant orbit gives much better results than a non-resonant one for the Love number and for the areas near the spacecraft tracks, but then parts of the surface are not covered. However, the retrieved uncertainty for a resonant orbit would allow a better understanding of Mercury's internal structure and to determine the size of the outer liquid core with a precision of less than 10 km. This would help to improve dynamo models for explaining the origin of Mercury's global magnetic field and would allow putting more detailed constraints in the models.

In general it can be concluded that the resonant orbit gives good results for the tidal Love number which are at least five times more precise, except for the two cases which were explained above. The topography is accurately mapped, but there are several areas without any observations (fig. 5.6).

5.4.5 Orbital data coverage restriction

The instruments of the MPO shall be shut-down when Mercury has a true anomaly of 10 to 40 and 310 to 340 degrees. Within these regions MPO will never be in the shade of Mercury to cool down the instruments. Therefore, simulations are performed for testing the impact on the extraction of the tidal Love number and of its uncertainty by local basis functions.

Best results are obtained for using half of the grid points in longitude and the same number of grid points in latitude direction compared to the number of grid points of the input topography model. Additionally the altitude restriction is included. The tidal Love number was determined to 0.7026 ± 0.0549 . Including the data restriction due to thermal constraints gives a tidal Love number of 0.7053 ± 0.0629 . Both simulations use 22 different topography models. The uncertainty of the tidal Love number increases by 28 % from the case without thermal constraints. Without data restriction the uncertainty is about 7.8 %, and with data restriction about 9.0 %.

For the method with local basis functions, the precision of the extraction decreases approximately linearly with the reduction of the data coverage of the surface. As data are available in Mercury's perihelion, where the tidal signal is largest, and as this region is sampled again at different tidal phase, the effect on the extraction of the tidal Love number is moderate. The standard deviations of the topography with respect to the input topography are not much affected either. The regions which are covered less by simulations hardly show an increase of the uncertainty, but as the basis functions are local, restrictions have less effect than for the approach using the global basis functions.

5.5 Transformation of the extracted topography into a spherical harmonic expansion

The extracted topography models are also transformed into a spherical harmonic expansion. The description of the topography as a spherical harmonic expansion is important as the long-wavelength topography shall be compared and analyzed with the long-wavelength gravity field of Mercury. The topography is transformed by the approach of a projection where the extracted topographic grid is transformed into a spherical harmonic expansion by

$$C_{lm} = \frac{1}{4\pi} \int \int T(\theta, \lambda) P_{lm}(\cos \theta) \cos(m\lambda) \sin \theta d\theta d\lambda, \quad (5.51)$$

$$S_{lm} = \frac{1}{4\pi} \int \int T(\theta, \lambda) P_{lm}(\cos \theta) \sin(m\lambda) \sin \theta d\theta d\lambda, \quad (5.52)$$

where $P_{lm}(\cos \theta)$ are the associated Legendre functions and $T(\theta, \lambda)$ the extracted topographic altitudes at the grid points. Three different cases are investigated (fig. 5.7): a) simultaneous analysis without any restrictions for a non-resonant orbit (\diamond), b) simultaneous analysis with restrictions by the maximum spacecraft altitude where observations can be taken up to 1000 km for a non-resonant orbit (\times), and c) simultaneous analysis without an restrictions for a resonant orbit (\circ). The transformation is compared for three different grid definitions: I) $i_{long} = 1$, II) $i_{long} = 2$, and III) $i_{long} = 4$. The mean degree error is

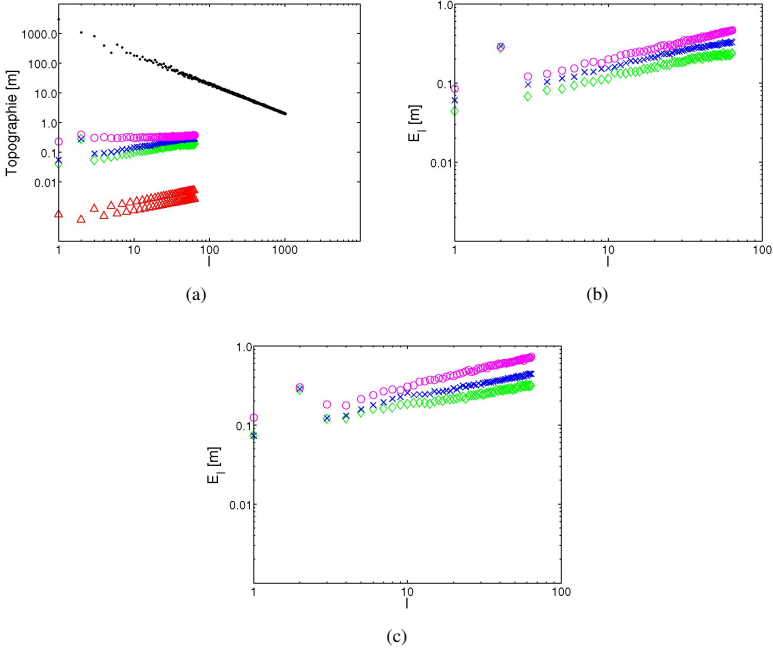


Figure 5.7: Harmonic degree amplitude $\sqrt{V_l}$ (eq. 3.1) of static input topography (\cdot) and mean degree error E_l (eq. 5.53) of the input topography (Δ), as well as mean errors of the transformed output topography for step functions: for a non-resonant orbit without data restrictions (\diamond), for a non-resonant orbit with limiting measurements up to 1000 km spacecraft altitude (\times), and for a resonant orbit with 4 Mercury years (\circ). No grid points are combined in latitude direction ($i_{lat} = 1$). In panel a) no grid points are combined in longitude direction ($i_{long} = 1$), in b) 2 grid points are combined ($i_{long} = 2$), and in c) 4 grid points ($i_{long} = 4$).

similarly derived as eq. (4.7),

$$E_l = \sqrt{\sum_{m=0}^l (C_{lm}^{inv} - C_{lm})^2 + (S_{lm}^{inv} - S_{lm})^2}, \quad (5.53)$$

where the index *inv* indicates topography coefficients obtained by the transformation.

Figure 5.7a shows one specific input topography model (\cdot) and the uncertainty of the transformation when the input topography are directly transformed back into a spherical harmonic expansion (Δ). This precision is the upper limit of the precision which can be obtained by transformation of the output topography. The standard deviations for the 22 different topographies is marginally small with less than 2 cm uncertainty. Even degrees

5.5 Transformation of the extracted topography into a spherical harmonic expansion

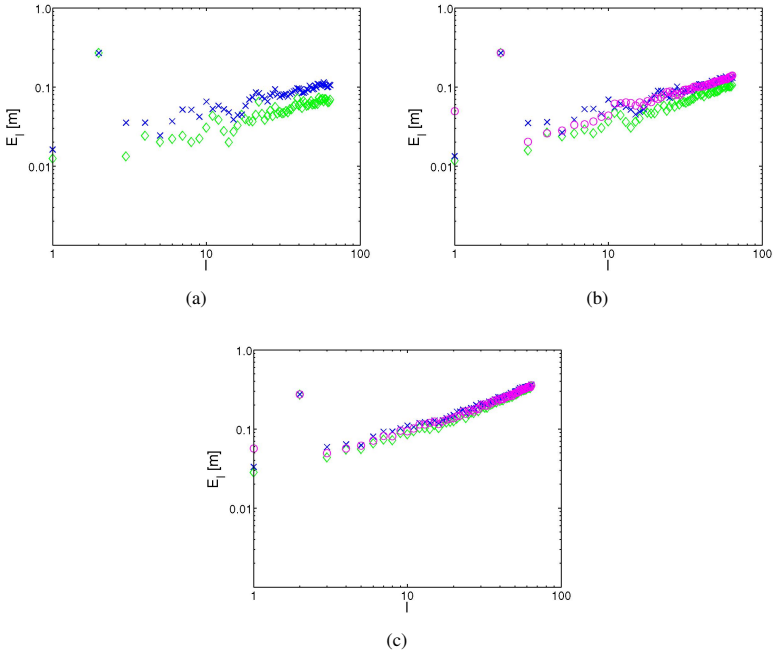


Figure 5.8: Mean errors of the transformed output topography applying now linear functions, else similar to fig. 5.7.

are more accurately extracted than the odd ones. The function of the odd degrees has a maximum value at the equator, while the even ones are zero there. A large uncertainty can be predicted for the equatorial region, as there the laser tracks are widely spaced to each other. The surface weighting factor $\sin \theta$ makes this effect even more pronounced.

Figure 5.7 includes the results of the performed transformations when step functions are used as local basis functions in longitude direction whereas in fig. 5.8 the local basis functions are linear functions and in fig. 5.9 are cubic spline functions. The parameters of the different orbits are given in tab. 3.1.

The transformation of the results for step functions in longitudinal direction has a dependency on the binning parameter i_{long} and on the different orbit restrictions. The mean errors of the degrees are in the range from 5 cm for low degrees up to 20 cm for the maximum degree of 64 when a non-resonant orbit and equal number of grid points of the input and output topography are used. The mean errors increase to 30 cm for low degrees up to 80 cm for the maximum degree in the case of a resonant orbit and the binning parameter $i_{long} = 4$ (fig. 5.7). The uncertainties E_l are rather large compared to the results obtained with linear and cubic spline functions.

The errors of the transformation for linear functions increase with increasing i_{long} from

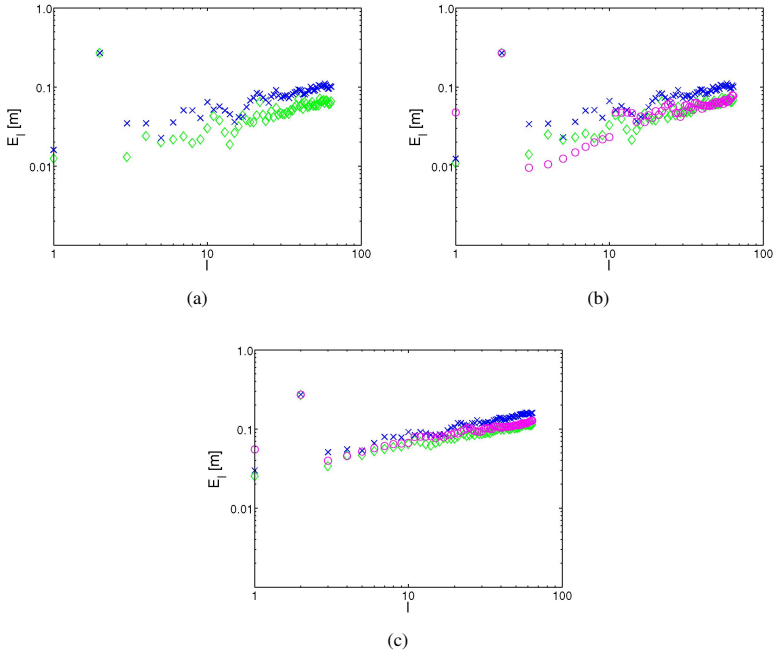


Figure 5.9: Mean errors of the transformed output topography applying now cubic spline functions, else similar to fig. 5.7.

an error of about 6 cm for $i_{long} = 1$ to 30 cm for $i_{long} = 4$. Such an increase has also been found in sec. 5.3.2. The errors of the transformation for cubic spline functions in longitudinal direction do not depend as much on i_{long} as the errors for linear functions and are approximately 10 cm for $i_{long} = 1, 2$ and less than 20 cm for $i_{long} = 4$. The effect is not larger than several millimeters for different tests which are performed. Restricting observations to 1000 km spacecraft altitude has a minor effect. The uncertainties only increase by several millimeters. Different orbits do not significantly affect the analyses, while increasing i_{long} has large effect.

If the obtained results are compared with the results of sec. 4.4, the errors of this approach are smaller than for the direct determination of the spherical harmonic coefficients. The errors for the cubic spline functions and for the binning parameter $i_{long} < 4$ are half as large as for the direct determination (sec. 4.4).

Figures 5.7 to 5.9 also show that the mean error for degree 2 is significantly larger (approximately 30 cm) than the other mean errors for all the tests. Analyzing the different coefficients of degree 2 shows that the coefficients C_{20} and C_{22} have an offset. This offset corresponds to the permanent tidal deformation of Mercury due to the solar gravitation.

5.5 Transformation of the extracted topography into a spherical harmonic expansion

From eq. (2.22) and (5.51) it follows that the quantity of $C_{20,\text{tide}}$ is given by approximately

$$\begin{aligned} C_{20,\text{tide}} &\approx -h_2 \frac{M_{\text{Sun}}}{M_{\text{Merc}}} \frac{a^4}{R^3} \frac{1}{4\pi} \int_0^\pi \int_0^{2\pi} \frac{1}{16} (3 \cos^2 \theta - 1)^2 \sqrt{\frac{5}{\pi}} \sin \theta d\theta d\lambda \\ &\approx -0.3 \text{ m} \end{aligned}$$

for $h_2 = 0.7$. A more detailed evaluation will follow as future work.

6 Extraction of the tidal signal at orbit crossovers in the polar regions

The previous chapters contain approaches where the basis functions are either globally expressed as a spherical harmonic expansion (ch. 4) or locally expressed as a rectangular grid (ch. 5). Both approaches are based on a simultaneous extraction of the static topography and the time-dependent variations of the topography. The parameters describing the time-dependence of the topography are the tidal Love number h_2 and the 88-day forced libration amplitude Φ_{lib} . The following investigations neglect a more detailed analysis for the global static topography and the forced libration amplitude (sec. 2.4). The presented approach investigates in more detail crossovers and uncertainties which limit the uncertainty of a crossover. By determining the uncertainty of a crossover, estimations are conducted to investigate a possible uncertainty for the tidal Love number which is assumed to have a peak-to-peak amplitude of 60 cm in the Polar Regions of Mercury.

Smith et al. (2001a) show that an extraction of snow-depth variations for Mars is possible in the polar region by using the laser altimeter data (MOLA, sec. 2.3.3) of the MGS spacecraft. The snow-depth variation has an amplitude of 1 m which is approximately the amplitude of the tidal Love number on Mercury.

6.1 Introduction

Chapter 4 and 5 show approaches for extracting the global topography simultaneously with the Love number, and additionally in a second step the libration amplitude (Koch et al. 2008, 2009a). Both time-dependent variations (sec. 2.4), tidal Love number h_2 and libration amplitude Φ_{lib} , have their maximum amplitude in the equatorial plane. While the amplitude of the libration decreases to zero closer to the poles, there is still some tidal elevation to be expected in the Polar Regions. The tidal amplitude is three times smaller than in the equatorial region, but still present.

Equation (2.22) describes the distribution of the tidal signal Ψ on Mercury's surface depending on the solar hour angle Λ

$$\frac{3}{2} \cos^2 \Psi - \frac{1}{2} \approx -\frac{1}{4} (3 \cos^2 \theta - 1) + \frac{3}{4} \sin^2 \theta \cos 2(\Lambda + \lambda) . \quad (6.1)$$

The first term on the right side of the equation is the long periodic, zonal part of the tide, while the semi-diurnal (sectorial) part of the tide is included in the second term. The whole equation depends on the co-latitude θ , and has a maximum for the cosine-term at the poles ($\theta = 0$ and 180°) and for the sine-term at the equator ($\theta = 90^\circ$). Equation (6.1)

becomes

$$\frac{3}{2} \cos^2 \Psi - \frac{1}{2} \approx -\frac{1}{4} (3 \cos^2 \theta - 1), \quad (6.2)$$

if $\theta \approx 0$ degree or $\theta \approx 180$ degrees. Mercury also shows a tidal effect at its poles because of its eccentric orbit which leads to a variation of the strength of solar gravitation (sec. 2.1). Orbit crossovers, which are concentrated in the Polar Regions of Mercury, can be used for extracting time-dependent topographic variations. For the computation of a topographic height difference between two laser tracks passing a crossover at different times, three groups of parameters have to be investigated:

1. Uncertainties related to the measurement have to be analyzed. This includes uncertainties of the spacecraft position, the range uncertainty, and pointing uncertainties (sec. 6.2.1).
2. The small-scale topography between the next neighboring laser shots and the crossover has to be considered as uncertainty, as it is not measurable (sec. 6.2.2).
3. Additional investigations have to be carried out for the uncertainties arising from the interpolation method for the topography between the next neighboring laser shots and the crossover (sec. 6.2.3).

The main limitation of the analysis is based on whether the instrumental and positioning uncertainties are the main error source. In that case a more detailed analysis of systematic errors with non-Gaussian distribution is needed. These errors will be studied during calibration of the instrument. The instrument temperature is one of those systematic uncertainties. The latter is effected by Mercury's surface temperature variation which can be described by trigonometric functions and by Mercury's orbital parameters. A more detailed analysis has to be part of future work (ch. 8).

The yet unknown small-scale topography of Mercury is estimated in more detail by using investigations of the Moon, Mars, Venus, and other terrestrial bodies. The distribution of the small-scale topography is expressed as power spectral density (fig. 2.3) to show the direct relation to the approach of ch. 4 and 5. There, the input topography is expressed as a spherical harmonic expansion where the spectral density is a function of the spherical harmonic degree (sec. 3.1).

Different interpolation methods can be used here. To take into account more observations at larger distances to a crossover, higher-order interpolation methods are analyzed. Simple interpolation such as linear interpolation is useful when only neighboring observations of the respective crossover are taken into account. A higher-order interpolation can give a better fit of the surface, while low-order interpolations may reflect less detail of the surface structure. More variation than that of a simple slope is shown in general for variations within 300 m distance. Two laser shots are separated by 300 m for the orbit of MPO in the equatorial region if it is mapped by BELA with a 5 Hz shot frequency. For the Polar Regions this value decreases due to slower motion. In that part of the orbit, the 300 m represent the worst case. As the whole analysis is a worst case study, the largest possible value is chosen. The slope variation is not known. The easiest approximation is to use low order interpolation methods, even if they smooth the topography (sec. 6.3.1).

Small-scale topography and interpolation uncertainties have to be expressed in higher orders because the tidal signal which shall be retrieved is assumed to be only 30 cm.

This is only half of the predicted amplitude of the tidal elevation in the Polar Regions of Mercury. The uncertainty of the laser altimeter is assumed to be about 1 m after post-processing. The determination of the tidal amplitude cannot directly be achieved from one single topographic difference measurement at a crossover. Therefore, the approach is based on a statistical analysis of all possible crossovers where the contributions of different sources of uncertainty are included by an error propagation (sec. 6.2.4).

6.2 Setup of the analysis

Different error sources have to be taken into account for the analyses of topographic measurements at orbit crossovers: a) interpolation uncertainties, b) uncertainties due to the small-scale topography between the observations, and c) positioning and instrumental uncertainties. The complete mathematical approach on which the analysis is based will be explained in detail.

6.2.1 Positioning and instrumental uncertainties

Positioning and instrumental uncertainties which affect the determination of crossovers will separately be described. At the end a final equation summarizes the previously mentioned uncertainties that are then used for the error estimation (sec. 6.2.4) by an error propagation which assumes that all used uncertainties are purely Gaussian.

Instrumental uncertainties are a sum of different single components. The first component is the uncertainty of the spacecraft position. Positioning uncertainties of the spacecraft will be observed by the radio science experiment (Milani et al. 2001), which tracks the position of the spacecraft. Further uncertainties are measured from the star tracker camera which is needed for the orientation of the spacecraft itself. The positioning uncertainty is the most important one. The spacecraft position is abbreviated as SC . The uncertainty is assumed to be 1 m (sec. 2.2.3). This uncertainty is assumed to be known with a precision of 0.1 m after post-processing the observations of the radio science experiment MORE of the BepiColombo mission (personal communication with Iess, 2006; Milani et al. (2001)). An uncertainty of 1 m is assumed as worst case to ensure that the estimations are not too optimistic. Furthermore, there are instrumental uncertainties of the laser altimeter itself. Instrumental uncertainties of laser altimeter observations are analyzed by Gardner (1982, 1992). He found that the main uncertainties arise by the pointing jitter, beam divergence, and surface slope within the laser footprint. Uncertainties of laser altimeter records are described in more detail in sec. 2.3.1.

When the altimeter does not point towards nadir, the main angular offsets are known and can be corrected within the analyses. Therefore, they are set to zero and only the pointing jitter remains. Pointing jitter is the sum of the pointing uncertainties of the instrument which are not known. These uncertainties are marginally small. Gunderson et al. (2006), Thomas (2006) and Thomas et al. (2007) specify the instrumental parameters in more detail. A brief overview for the BepiColombo laser altimeter is given in sec. 2.3.5 and in tab. 2.4.

The topography height for one measurement can be derived as

$$T = SC - R - Ra \cos(\alpha), \quad (6.3)$$

where T is the topographic height at the sampling point, SC is the radius from the center of mass of Mercury to the spacecraft, R the radius of the reference sphere which is assumed to be equal with the aeroid of the planet, Ra the range of the altimeter, and α the off-nadir angle of the instrument which is set to zero for simplification.

The analyses of topographic difference measurements at crossovers need several observations along two tracks. The topographic difference on the one hand is based on uncertainties from the determination of the crossover, and on the second hand on tidal elevation changes. The number of observations depend on the chosen interpolation method (sec. 6.2.3). Altimetry measures topographic points along a track. The distance between two observations depends on the radial velocity of the spacecraft and the shot frequency of the instrument. The distance between two observations has to be assumed to be known (sec. 6.2.2). All observations used for determining a crossover are assumed to have the same range of uncertainties. The observations affecting the determination of a crossover are taken within 1 s. Huge variations of uncertainties within this time-duration are not expected as the spacecraft does not change its position or orientation. Therefore the positioning and pointing uncertainties along one spacecraft track can be assumed to be nearly stable. It is more critical to assume that the uncertainties are approximately the same for all the different tracks. Therefore worst case values are chosen for the study. Assuming a similar range uncertainty for all positions is realistic, as observations are taken at the same part of MPO's orbit. Non-Gaussian uncertainties are neglected, although they are important, but are beyond the scope of this work. The pointing direction of the instrument can vary within the different tracks, but this can be corrected due to the observed off-nadir angle α . More important is that the pointing jitter does not become larger than the given maximum value which is chosen for the analyses. This value is given by Gunderson et al. (2006) and Thomas (2006).

6.2.2 Uncertainties related to small-scale topography

The second uncertainty which affects the uncertainty of a measurement at a crossover is the small-scale topography between the centroids of two laser records. The small-scale topography of Mercury is described in more detail (sec. 2.1) where the introduction of Mercury as a planet, its orbit, its surface, its internal structure, and its weak magnetic field has already been given.

Mercury is assumed to be an end-state planet which is geologically very old. Atmospheric erosion can be neglected because Mercury does not have any significant atmosphere, only an exosphere. Mercury's surface can be assumed being similar to the surface of the Moon or the rough surfaces of the Southern Highlands of Mars.

A detailed description of the Moon's topography can be found in McEwen and Robinson (1997), Neumann (2001), Rummel (2005) and Wieczorek (2007). For Mars, Aharonson et al. (2001) have measured the power spectral density of the topography for two types of areas: a) the Southern Highlands, which are geologically old and thus heavily cratered, and b) the Northern Lowlands, which resemble an ocean floor dominated by geological features from sedimentation. Figure 2.3 shows the different types of areas expressed as a power spectral density.

The small-scale topography of the Northern Lowlands is described by

$$\begin{aligned} P\left(\frac{1}{\lambda}\right) &= 1 \frac{\text{m}^2}{\left(\frac{\text{cycles}}{\text{km}}\right)} \left(\frac{1 \text{ km}}{\lambda}\right)^{-\beta} = 10^3 \text{ m}^3 \left(\frac{10^3 \text{ m } 2\pi}{2\pi \lambda}\right)^{-\beta} \\ &= P_{\text{ST}} k^{-\beta}; \quad F_0 \approx 3.3 \cdot 10^{-5} \text{ m}^3 \text{ s}^{-\beta}, \end{aligned} \quad (6.4)$$

where k is $2\pi/\lambda$ and $\beta = 3.4$.

Generally, the two types of Martian topography described by Aharonson et al. (2001) can be characterized by three parameters (see eq. (6.5) below):

1. The roll-over scale $\lambda_{\text{ro,SH/NL}} = 2\pi/k_{\text{ro,SH/NL}}$ indicating the transition from the large scales dominated by relief-building tectonics and volcanism to the small scales dominated by planation processes such as sedimentation and erosion. The subscripts SH and NL denote ‘‘Southern Highlands’’ and ‘‘Northern Lowlands.’’
2. The pre-factor $P_{\text{ro,SH/NL}}$ indicating the power spectral density at the roll-over scale.
3. The spectral indices $\beta_{\text{LS/SS,SH/NL}}$ of the power spectral density as a function of the wave number $k = 2\pi/\lambda$, which usually follows a power law. The subscripts LS and SS denote large-scale ($\lambda > \lambda_{\text{ro}}$) and small-scale ($\lambda < \lambda_{\text{ro}}$) topography.

With these parameters the power spectral density is expressed as

$$P(k) = P_{\text{ro,SH/NL}} \left(\frac{k}{k_{\text{ro,SH/NL}}}\right)^{-\beta_{\text{LS/SS,SH/NL}}}. \quad (6.5)$$

The parameters are $\lambda_{\text{ro,SH}} \approx \lambda_{\text{ro,NL}} \approx 10 \text{ km}$, $\beta_{\text{SS,SH}} \approx \beta_{\text{SS,NL}} \approx 3.4$, $\beta_{\text{LS,SH}} \approx 2.0$, $\beta_{\text{LS,NL}} \approx 1.4$, $P_{\text{ro,SH}} \approx 7.5 \times 10^6 \text{ m}^3$, and $P_{\text{ro,NL}} \approx 2.3 \times 10^5 \text{ m}^3$.

The large-scale power spectral density of the Martian Southern Highlands is approximately – within a factor 2 – concordant with the scaling law for the degree power used in the presented results of ch. 4 and 5

$$V_l = \frac{A^2}{l^2}; \quad A \approx 2000 \text{ m}. \quad (6.6)$$

If wave numbers $k_l = l/R_{\text{Merc}}$ are defined, $R_{\text{Merc}} \approx 2440 \text{ km}$, the degree power is the integral over the power spectral density of the topography from k_l to k_{l+1}

$$\begin{aligned} V_l &= \int_{k_l}^{k_{l+1}} dk P(k) = \int_{k_l}^{k_{l+1}} dk P_0 k^{-\beta} \\ &= \frac{P_0}{1-\beta} k_l^{1-\beta} \left[\left(\frac{l+1}{l}\right)^{1-\beta} - 1 \right] \approx \frac{P_0}{l} k_l^{1-\beta} \\ &= P_0 k_1^{1-\beta} l^{-\beta} =: A^2 l^{-\beta}. \end{aligned} \quad (6.7)$$

This means, the parameter A is $A = k_1^{1-\beta}$, or if $\beta = 1$, then $A = P_0/k_1 = P_0 R_{\text{Merc}}$. From $P_{\text{ro,SH}} \approx 7.5 \times 10^6 \text{ m}^3$ and $\lambda_{\text{ro,SH}} \approx 10 \text{ km}$, $P_0 = 0.075 (2\pi)^2 \text{ m}^3$ is computed, and thus $A^2 \approx 7.4 \times 10^6 \text{ m}^2$ or $A \approx 2720 \text{ m}$. From the comparison of the impact crater size-frequency distributions of Mars, Mercury, and the Moon in fig. 21 of Head et al. (2007),

one can conclude that Mercury should be somewhat subdued in comparison to the Moon. Therefore, the number $A \approx 2000$ m is a conservative estimate.

The amplitude of the small-scale topography at wave numbers larger than $k_{\text{BELA}} = \pi/300 \text{ m}^{-1} \approx 0.01 \text{ m}^{-1}$ is calculated as

$$\begin{aligned} \Delta T^2(k > k_{\text{BELA}}) &= \int_{k_{\text{BELA}}}^{\infty} P_{\text{ST}} k^{-\beta} dk = \frac{P_{\text{SS}}}{\beta - 1} k_{\text{BELA}}^{1-\beta} = 0.45 \text{ m}^2 \\ \Rightarrow \Delta T(k > k_{\text{BELA}}) &\approx 70 \text{ cm}, \end{aligned} \quad (6.8)$$

where the values given for ΔT apply for $P_{\text{ST}} = 10^{-4} \text{ m}^{3-\beta}$ and $\beta = 3.4$ describing the topography of the Southern Highlands of Mars.

The topography is split into a long-wavelength part $T_{LS}(x)$ including wave numbers $k < k_{\text{BELA}}$ and a short-wavelength part $T_{SS}(x)$ including wave numbers $k > k_{\text{BELA}}$, respectively

$$T(x) = T_{SS}(x) + T_{LS}(x). \quad (6.9)$$

6.2.3 Uncertainties caused by interpolation

The position of a crossover is assumed not to be identical with the position of a laser record in most cases. If it was identical, the tidal amplitude and the tidal Love number h_2 could be determined very precisely. Using only the two neighboring laser records for interpolating the topography to the crossover has large uncertainties. A better description of the surface can be achieved by higher order interpolation methods, as spline interpolation or a polynomial interpolation which more precisely approximate the laser records.

Low-order interpolation methods, as step function or linear interpolation, can be used for approximations. As shown in sec. 6.2.2, Mercury has an old surface which can be described similar to the Moon's surface or Martian Southern hemisphere which is highly cratered. The surface has then larger altitude variations between two laser records than the approximated amplitude of the tidal Love number of 30 cm (sec. 6.1).

6.2.3.1 Cubic spline interpolation

The uncertainty contribution of a cubic spline interpolation $S(x)$ to the topography function $T_{LS}(x)$ is given in, e.g., Freund and Hoppe (2007) as

$$\Delta T_{\text{CS}} = |F(x) - S(x)| \leq 2.5 L^4 \supr |T_{LS}^{(4)}(x)|, \quad (6.10)$$

where $L \approx 300$ m is the shot-to-shot distance for measurements of BELA when MPO is in perihelion and a shot frequency of 5 Hz is assumed. This is the largest shot-to-shot distance. For all other parts of the orbit of MPO, the laser shots are closer to each other. The value of 300 m is chosen to be a worst case, when observations can continuously be taken all over the orbit.

The fourth derivative of the function $T_{LS}(x)$ can be estimated from the Fourier spectrum of the topography

$$T_{LS}^{(4)}(x) \approx \sqrt{\frac{2}{\pi}} \int_0^{\frac{\pi}{L}} dk k^{4-\frac{\beta}{2}} \cos(kx) \quad (6.11)$$

$$\begin{aligned} \Rightarrow \left\langle |T_{LS}^{(4)}(x)|^2 \right\rangle &\leq \frac{1}{2\pi} \int_0^{\frac{\pi}{L}} dk P_{ST} k^{8-\beta} = \frac{P_{ST}}{2\pi(9-\beta)} \left(\frac{\pi}{L}\right)^{9-\beta} \\ \Rightarrow 2.5L^4 |T_{LS}^{(4)}(x)| &\leq \frac{2.5\sqrt{P_{ST}}}{2\pi(9-\beta)} \pi^{\frac{9-\beta}{2}} L^{\frac{\beta-1}{2}}. \end{aligned} \quad (6.12)$$

This leads to an interpolation uncertainty of

$$\Delta T_{CS} = 10.40.00057 300^{1.2} \text{ m} \approx 56 \text{ m}. \quad (6.13)$$

Interestingly, the estimate of the fourth derivative diverges, if $T_{SS}(x)$ is included. Additionally, the residual uncertainty ΔT_{CS} when approximating $T_{LS}(x)$ is quite large and not sufficient for a determination of the tidal Love number from a crossover analysis.

6.2.3.2 Polynomial interpolation

Another approach for the interpolation of the crossover is based on a polynomial interpolation, for which Freund and Hoppe (2007) give a residual uncertainty of

$$T(\bar{x}) - P_{01\dots n}(\bar{x}) = \frac{\omega(\bar{x}) T^{(n+1)}(\xi)}{(n+1)!}. \quad (6.14)$$

The mean distance of approximately 300 m between two laser shots in the frame of the BELA instrument is used. Then the following expression can be found, where n has to be optimized for an minimum value

$$\sqrt{\frac{k_{\text{BELA}}^{2n+3-\beta}}{2n+3-\beta} \frac{\omega(x)}{(n+1)!}}. \quad (6.15)$$

High polynomial interpolation show the effect of Runge's phenomena which states that within an interpolation interval $(n+2)$ maxima and minima will be present, especially close to the borders of the interpolation. The interpolation is done for a) $n=1$ for a linear polynomial interpolation, b) $n=2$ for a quadratic polynomial interpolation, and c) $n=3$ for a cubic polynomial interpolation. They can be written as

$$T_{int}^{n=1} = \sqrt{\frac{k^{5-\beta}}{5-\beta}} \sqrt{\frac{P_{ST}}{2\pi}} \frac{L\Delta L - \Delta L^2}{2}, \quad (6.16)$$

$$T_{int}^{n=2} = \sqrt{\frac{k^{7-\beta}}{7-\beta}} \sqrt{\frac{P_{ST}}{2\pi}} \frac{L^2\Delta L - \Delta L^3}{6}, \quad (6.17)$$

$$T_{int}^{n=3} = \sqrt{\frac{k^{9-\beta}}{9-\beta}} \sqrt{\frac{P_{ST}}{2\pi}} \frac{2L^3\Delta L - L^2\Delta L^2 - 2L\Delta L^3 - \Delta L^4}{24}. \quad (6.18)$$

Equations (6.16) to (6.18) include the uncertainty based on the interpolation. They are assumed to be the standard deviation of the interpolation.

According to the Nyquist theorem, BELA cannot sample wave numbers $k > k_{\text{BELA}}$. The uncertainty for a topography difference measurement at a crossover introduced by the small-scale topography $T_{SS}(x)$ depends on the distances ΔL_I and ΔL_{II} from a crossover

to the next measurement locations belonging to the crossing spacecraft tracks *I* and *II*. This uncertainty can be estimated by making use of the autocorrelation function and the Wiener-Khintchine theorem

$$\langle |T_{SS}(x) - T_{SS}(x + \Delta L)|^2 \rangle = 2 [R_{SS}(0) - R_{SS}(\Delta L)], \quad (6.19)$$

where

$$R_{SS}(\Delta L) = \frac{1}{\pi} \int_{\pi/h}^{\infty} P_{SS}(k) \cos(k\Delta L) dk. \quad (6.20)$$

Applying partial integration gives

$$R_{SS}(\Delta L) = \frac{P_{ST} k_{\text{BELA}}^{-\beta+1}}{\pi \beta - 1} \left[\cos(k_{\text{BELA}}\Delta L) + \frac{\Delta L k_{\text{BELA}}}{2 - \beta} \sin(k_{\text{BELA}}\Delta L) \right. \quad (6.21)$$

$$\left. + \frac{\Delta L^2}{2 - \beta} \int_{k_{\text{BELA}}}^{\infty} dk k^{2-\beta} \cos(k_{\text{BELA}}\Delta L) \right]. \quad (6.22)$$

This leads to

$$\begin{aligned} & \langle |T_{SS}(x) - T_{SS}(x + \Delta L)|^2 \rangle = \\ & = \Delta T_{SS} = (k_{\text{BELA}}\Delta L) \sqrt{C_{\text{BELA}}(\beta) R_{\text{BELA}}^0} \left(\sqrt{1 + \frac{\Delta L^2}{(L - \Delta L)^2}} \right)^{-1}, \end{aligned} \quad (6.23)$$

with

$$C_{\text{BELA}}(\beta) \leq \frac{\beta}{\beta - 3}, \quad (6.24)$$

$$R_{\text{BELA}}^0 = \frac{P_{ST} k_{\text{BELA}}^{1-\beta}}{\pi \beta - 1}, \quad (6.25)$$

where P_{SS} is computed by eq. (6.5). β is assumed to be larger than 3. The above expression takes into account the measurements at x and $x + L$.

The uncertainties for the small-scale topography and the uncertainties based on the interpolation method are combined to one general equation which depends on ΔL where ΔL is the distance to the closest observation on one track:

$$\sigma_{\Delta L} = \sqrt{(\Delta T_{SS})^2 + (T_{\text{int}}^{n=i})^2}. \quad (6.26)$$

6.2.4 Error propagation of the uncertainties

An overview over the included uncertainties is given in sec. 6.2.1 to 6.2.3. Here, the error propagation is computed for those uncertainties which affect a crossover. First the main equations of the above sections are summarized and afterwards the derivatives are finally shown. The general approach is described in detail in Niemeier (2002).

6.2.4.1 Basic equations for the error propagation

The analytical approach is based on the above mentioned uncertainties. The following steps are carried out:

- Measurement $T_{i,j}$
The observation $T_{i,j}$ can be described as the i th measurement on track j which includes all positioning and instrumental errors (eq. 6.3).
- Crossover $T_{C;j}$
The topographic measurement at a crossover depends on the observations on track j and their uncertainties as well as on the uncertainties related to the interpolation and the small scale topography.
- Crossover difference ΔT_C
The topographic height changes at the crossovers can be determined as a difference between two chosen orbits j and $j + 1$:

$$\Delta T_C = T_{C;j} - T_{C;j+1}. \quad (6.27)$$

- The uncertainty of the topographic difference $\sigma_{\Delta T_C}$ at a crossover is computed from the rules of error propagation.
- The mean uncertainty of the topographic difference measurements at all crossovers $\bar{\sigma}_{\Delta T_C}^2$ is:

$$\bar{\sigma}_{\Delta T_C}^2 = \frac{\sigma_{\Delta T_C}^2}{N}. \quad (6.28)$$

6.2.4.2 Derivatives for the error propagation

The correlation between the single uncertainties is neglected for the error propagation here. This is only partly true; especially for the positioning and instrumental errors correlations are expected. Further analyses have to be performed where correlations are considered. The variance matrix has the following structure

$$\mathbf{P} = \text{diag} \left(\sigma_{SC;j}^2; \sigma_{Ra;j}^2; \sigma_{\alpha;j}^2; \sigma_{\Delta L;j}^2; \sigma_{SC;j+1}^2; \sigma_{Ra;j+1}^2; \sigma_{\alpha;j+1}^2; \sigma_{\Delta L;j+1}^2 \right). \quad (6.29)$$

The functional matrix has the following structure

$$\mathbf{F} = \left[\frac{\partial \Delta T_C}{\partial SC_j}; \frac{\partial \Delta T_C}{\partial Ra_j}; \frac{\partial \Delta T_C}{\partial \alpha_j}; \frac{\partial \Delta T_C}{\partial \sigma_{\Delta L_j}}; \frac{\partial \Delta T_C}{\partial SC_{j+1}}; \frac{\partial \Delta T_C}{\partial Ra_{j+1}}; \frac{\partial \Delta T_C}{\partial \alpha_{j+1}}; \frac{\partial \Delta T_C}{\partial \sigma_{\Delta L_{j+1}}} \right]. \quad (6.30)$$

The estimation of the measurement uncertainty at the crossover by error propagation has the structure

$$\sigma_{\Delta T_C}^2 = \mathbf{F} \mathbf{P} \mathbf{F}^T. \quad (6.31)$$

The partial derivatives of eq. (6.27) are

$$\frac{\partial \Delta T_C}{\partial S C_j} = 1, \quad (6.32)$$

$$\frac{\partial \Delta T_C}{\partial S C_{j+1}} = -1, \quad (6.33)$$

$$\frac{\partial \Delta T_C}{\partial \alpha_j} = -R a_j \sin(\alpha_j), \quad (6.34)$$

$$\frac{\partial \Delta T_C}{\partial \alpha_{j+1}} = R a_{j+1} \sin(\alpha_{j+1}), \quad (6.35)$$

$$\frac{\partial \Delta T_C}{\partial R a_j} = -\cos(\alpha_j), \quad (6.36)$$

$$\frac{\partial \Delta T_C}{\partial R a_{j+1}} = \cos(\alpha_{j+1}), \quad (6.37)$$

$$\frac{\partial \Delta T_C}{\partial \sigma_{\Delta L_j}} = 1, \quad (6.38)$$

$$\frac{\partial \Delta T_C}{\partial \sigma_{\Delta L_{j+1}}} = -1. \quad (6.39)$$

6.3 Results

The statistical estimation is divided into three different parts, which are separately investigated. First the error propagation at one single crossover is analyzed in more detail, i.e. which uncertainty of sec. 6.2 may have the largest impact. It will then be shown that there is no dependency of ΔL which is previously defined as the distance between two laser shots. At the end, a closer look is taken to the uncertainty which can be achieved when averaging the measurements at all crossovers in the whole polar region. This can directly be translated into the achievable precision for the tidal Love number (Koch et al. 2009b).

6.3.1 Error propagation at a crossover

The error propagation is described in more detail in sec. 6.2.4. The different components of the crossover uncertainty are explained in sec. 6.2.1 to 6.2.3. It will be shown that the uncertainties based on the interpolation and small-scale topography have the largest effect. In a second step the error propagation of all components is computed for different interpolation methods. The achieved uncertainties at the crossovers can then be used in a second step for the determination of a mean uncertainty (sec. 6.3.2).

The results for the single components are listed in tab. 6.1. The uncertainties caused by the positioning, pointing, and instrumental errors are assumed to be equal for all laser shots contributing to the determination of the tidal amplitude at a crossover because the shot points affecting a measurement at a single crossover are taken within less than 1 s. The variation of the positioning, pointing, and instrumental uncertainties are assumed to be marginally small within a time-duration less than 1 s. The crossing track is assumed to be in a similar range as for the first track. A more detailed description for solving the idealized simulation will be given in ch. 8.

Table 6.1: List of the uncertainties of the single error components at one crossover in meter. The uncertainties of the small-scale topography ΔT and the interpolation f_{int}^n are shown for different distances from the crossover ΔL up to the center between two shot points which is assumed to be 150 m. The uncertainties for the Polynomial interpolation are shown for the orders $n = 1, 2$ and 3

Positioning uncertainty σ_{SC} :	1.00
Pointing jitter uncertainty σ_{α} :	$4 \cdot 10^{-7}$
Range uncertainty (for $\sigma_{Ra} = 0.2$ m) :	0.20
Range uncertainty (for $\sigma_{Ra} = 1.0$ m) :	1.00
$\Delta T, \beta = 3.4, \Delta L = 0.0$ m :	0.00
$\Delta T, \beta = 3.4, \Delta L = 30.0$ m :	1.42
$\Delta T, \beta = 3.4, \Delta L = 60.0$ m :	2.78
$\Delta T, \beta = 3.4, \Delta L = 90.0$ m :	3.95
$\Delta T, \beta = 3.4, \Delta L = 120.0$ m :	4.77
$\Delta T, \beta = 3.4, \Delta L = 150.0$ m :	5.06
$f_{int}^{n=1}, \beta = 3.4, \Delta L = 0.0$ m :	0.00
$f_{int}^{n=1}, \beta = 3.4, \Delta L = 30.0$ m :	0.60
$f_{int}^{n=1}, \beta = 3.4, \Delta L = 60.0$ m :	1.07
$f_{int}^{n=1}, \beta = 3.4, \Delta L = 90.0$ m :	1.40
$f_{int}^{n=1}, \beta = 3.4, \Delta L = 120.0$ m :	1.60
$f_{int}^{n=1}, \beta = 3.4, \Delta L = 150.0$ m :	1.67
$f_{int}^{n=2}, \beta = 3.4, \Delta L = 0.0$ m :	0.00
$f_{int}^{n=2}, \beta = 3.4, \Delta L = 30.0$ m :	0.46
$f_{int}^{n=2}, \beta = 3.4, \Delta L = 60.0$ m :	0.90
$f_{int}^{n=2}, \beta = 3.4, \Delta L = 90.0$ m :	1.27
$f_{int}^{n=2}, \beta = 3.4, \Delta L = 120.0$ m :	1.57
$f_{int}^{n=2}, \beta = 3.4, \Delta L = 150.0$ m :	1.75
$f_{int}^{n=3}, \beta = 3.4, \Delta L = 0.0$ m :	0.00
$f_{int}^{n=3}, \beta = 3.4, \Delta L = 30.0$ m :	0.55
$f_{int}^{n=3}, \beta = 3.4, \Delta L = 60.0$ m :	1.01
$f_{int}^{n=3}, \beta = 3.4, \Delta L = 90.0$ m :	1.32
$f_{int}^{n=3}, \beta = 3.4, \Delta L = 120.0$ m :	1.43
$f_{int}^{n=3}, \beta = 3.4, \Delta L = 150.0$ m :	1.28

The single components are further plotted in fig. 6.1. The uncertainties are plotted versus the distance from a shot point to the crossover between two shot points ΔL . The different symbols denote the uncertainty arising from the positioning uncertainty (\diamond), from pointing jitter ($*$), from the range measurement (Δ), from the small-scale topography (\times), and from the interpolation (∇). The different interpolation methods are presented with different line styles: green for $n = 1$, cyan for $n = 2$, and magenta for $n = 3$. The range uncertainty is assumed to be red for 0.2 m, and blue for 1.0 m. Table 6.1 and fig. 6.1 show that the main influence comes from the small-scale topography which is unknown, and can only be estimated (sec. 6.2.2).

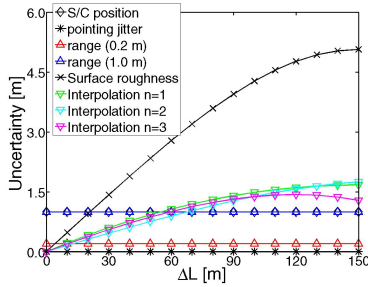


Figure 6.1: Uncertainties of each single component of the analyses plotted vs. the distance of the crossover to the closest observation ΔL (at maximum 150 m): the positioning uncertainty (\diamond), the uncertainty due to pointing jitter ($*$), the range uncertainty (Δ), the error related to the small scale topography (SST, \times), and the error based on the interpolation method (∇). The range uncertainty is plotted for the cases of 0.2 m uncertainty (red), and of 1.0 m uncertainty (blue). The polynomial interpolation is made for the linear case ($n = 1$; blue), for a quadratic expression ($n = 2$; cyan), and for a cubic expression ($n = 3$; magenta).

Analyses are only performed for distances of ΔL up to 150 m which is half of the distance between two laser shots. When the laser shot is further away than the center point, the next laser shot is taken. Uncertainties resulting from small-scale topography and interpolation are investigated up to this point and have their maximum at the center point. Instrumental and positioning uncertainties are only related to the laser shot itself and do not depend on the exact position of the crossover. The crossover depends on the uncertainty of the laser shot which is observed there. The range uncertainty and pointing uncertainty are chosen to satisfy the recent requirements of the BELA laser altimeter. The pointing uncertainty is chosen to fulfill eq. (6.3) where the pointing is approximated by a simple computation and the assumption that the surface is strictly flat at the center of the laser footprint. Then the pointing uncertainty is smaller than 1 mm and can be neglected. Extending the laser shot from a point measurement to the laser footprint which is affected by the surface slope, the uncertainty based on pointing uncertainties increases. For simplification, the laser footprint is assumed to be marginally small. The range uncertainty is firstly assumed to be 1 m for observations without post processing. Post processed data reach a range uncertainty of 0.2 m. The positioning uncertainties will vary due to gravity forces, solar

radiation, etc. For this, an uncertainty of 1 m is assumed. Higher precision shall be possible for some parts of the orbit for other parts a lower one on the other hand.

Figure 6.1 and table 6.1 show that the instrumental and positioning uncertainties are the main uncertainty up to a distance of 30 m from the closest shot point. The small-scale topography and the interpolation uncertainty dominate the error of a crossover after 30 m distance from an observation (fig. 6.1). That means the small-scale topography is the dominant uncertainty in most cases.

In a second step, the error propagation is computed for all above mentioned and analyzed uncertainties. Figures 6.2 to 6.4 show the retrieved results for one crossover. A linear polynomial interpolation (fig. 6.2), a quadratic polynomial interpolation (fig. 6.3), and a cubic polynomial interpolation (fig. 6.4) are used for a small range uncertainty of 0.2 m which can be determined by post-processing of the data, and of 1.0 m which can be assumed for the raw data. The range uncertainty of 0.2 m is shown in the left panel and of 1.0 m in the right panel of the figures. These figures illustrate the relation between the distance of a crossover to its closest observation ΔL_I on one track and the uncertainty at a crossover. The lines show the uncertainty as a function of the distance L_I on the one track, for certain values ΔL_{II} on the other track for the cases when the point of observation on the second track and the crossover are identical (\diamond), in 30 m distance (\circ), in 60 m ($*$), in 90 m (∇), in 120 m (Δ), and in 150 m (\times) distance.

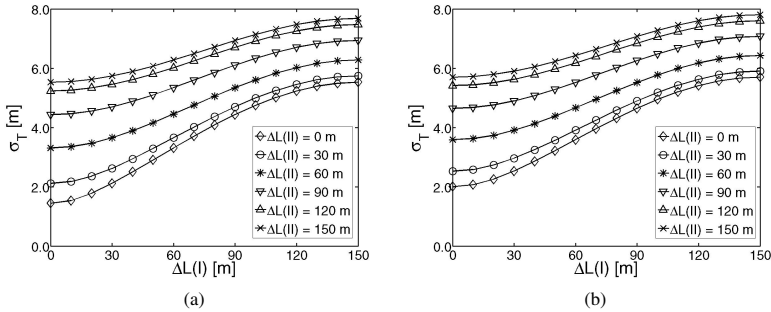
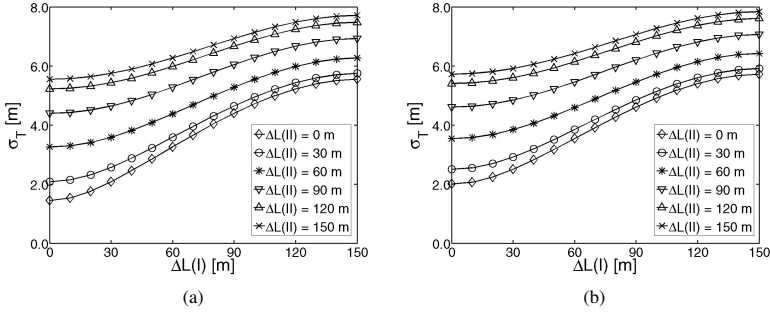
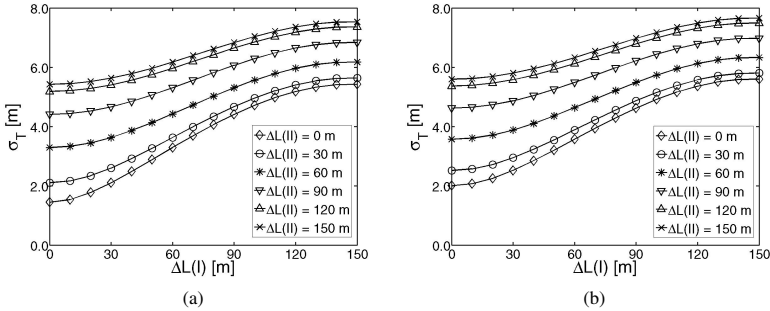


Figure 6.2: The uncertainty at a crossover after computing the error propagation plotted vs. the distance of the crossover to the closest observation on the one track ΔL_I for a polynomial interpolation with degree $n = 1$. The left panel shows the uncertainty at the crossover for a range uncertainty of 0.2 m, and the right one for an uncertainty of 1.0 m. The different lines refer to certain distances ΔL_{II} between the crossover and the observation point on the second track for the cases $\Delta L_{II} = 0$ m (\diamond), $\Delta L_{II} = 30$ m (\circ), $\Delta L_{II} = 60$ m ($*$), $\Delta L_{II} = 90$ m (∇), $\Delta L_{II} = 120$ m (Δ), $\Delta L_{II} = 150$ m (\times).

The different orders of polynomial interpolations include several advantages and disadvantages. The cubic polynomial interpolation has an additional oscillation close to the center point. This effect is called Runge's phenomena. The Runge's phenomena causes $(n+2)$ maxima and minima within an interpolation interval for an interpolation function of order n . Higher polynomial orders than the cubic one are not simulated because of this effect. The linear and quadratic polynomial interpolations give results of similar precision.

Figure 6.3: Same as fig. 6.2 for a Polynomial interpolation with $n = 2$.Figure 6.4: Same as fig. 6.2 for a Polynomial interpolation of $n = 3$.

The linear polynomial interpolation gives better results when the distance between the closest shot point and the crossover (ΔL) is larger than 140 m. The quadratic polynomial interpolation has smaller uncertainties close to the shot point. The quadratic interpolation leads to a better determination of the topographic height difference at the crossover. It is used for the following analyses of the mean uncertainty at crossovers, sec. 6.3.2.

6.3.2 Mean uncertainty at the crossovers

The computation of the mean uncertainty is shown in eq. (6.28). The equation contains the number of effective crossovers N which can be analyzed. Therefore each satellite track is assumed to be crossed with all the other satellite tracks. This is idealized. A limitation will be given later in this section. An additional parameter is included which represents the assumed mission duration. The mission duration is assumed to be at least 2 Mercury years. The nominal mission duration is 4 Mercury years. The number of Mercury years I which is used as additional parameter is an extra variable to be analyzed. Approximately $J = 910$ satellite tracks map the surface within one Mercury year. The

Table 6.2: Estimated mean uncertainties at the crossovers ($\bar{\sigma}_{\Delta T_C}$) and in brackets the percentage of the achievable, relative uncertainty p_{h_2} of the tidal Love number h_2 with an amplitude A_{h_2} of 30 cm in the Polar region, computed by eq. (6.41) and (6.42). The columns include the number of orbits (J) which are used for the estimation, and the rows the number of Mercury years (I)

I	J	
	455	910
2	0.010 m (3.3 %)	0.005 m (1.7 %)
4	0.007 m (2.3 %)	0.004 m (1.3 %)

number of satellite tracks within one Mercury year is fixed through the orbital parameters of MPO. The number must be around 910 orbital cycles of MPO within 1 Mercury year. Two cases are also assumed here. First, each track crosses all the others, and second only that half of the orbits is used which are closest to Mercury's peri- and apohelion. This minimizes J approximately to 455. N can be rewritten and then introduced in eq. (6.28)

$$N = I J^2, \quad (6.40)$$

$$\bar{\sigma}_{\Delta T_C} = \pm \frac{\sigma_{\Delta T_C}}{\sqrt{I} J}. \quad (6.41)$$

The estimation is performed for the worst case, when a range uncertainty of $\sigma_{Ra} = 1$ m, and the quadratic polynomial interpolation method are used, and when the crossover is on both tracks at largest distance $\Delta L_{J/II} = 150$ m. The uncertainty is then 8.2 m. The results are summarized in tab. 6.2. The columns include the different numbers of satellite tracks J which are used in eq. (6.40). The rows contain the number of Mercury years I as observation time. The mean uncertainty for crossovers is shown.

A required relative uncertainty of 3 % is introduced for the tidal Love number h_2 . From that a required measurement uncertainty for a single crossover measurement is calculated. The tidal Love number has an amplitude A_{h_2} of about 30 cm in the polar regions. The value is chosen to be half of the expected amplitude. The relative uncertainty is computed by

$$p_{h_2} = \frac{\bar{\sigma}_{\Delta T_C}}{A_{h_2}}. \quad (6.42)$$

The mean uncertainty of the tidal Love number (Σ_{Tide}) is less than 3 % corresponding to only 9 mm. Equation (6.41) can also be transformed to compute the mean uncertainty of the tidal Love number

$$\Sigma_{\Delta T_C} = \Sigma_{Tide} \sqrt{I} J. \quad (6.43)$$

The estimated maximum possible uncertainty at a single crossover is listed in tab. 6.3. Crossing 910 orbits is an ideal case. However, for the nominal mission duration and half of the satellite tracks assumed to cross gives a similar uncertainty. Taking into account that the amplitude of the tidal Love number is conservatively estimated to be 30 cm, half of the orbits give the needed accuracy for an extraction of the tidal Love number with an uncertainty smaller than 3 %. The other half of the points can then additionally be used for calibrating the instrument.

Table 6.3: Estimated uncertainties at the crossovers ($\Sigma_{\Delta T_C}$) for a determination of the tidal Love number with less than 3 %. The columns include the number of orbits (J) which are used for the estimation, and the rows the number of Mercury years (I)

	J	
	455	910
2	5.791 m	11.582 m
4	8.190 m	16.380 m

6.3.3 Optimum selection of crossover points

In a further step it shall be investigated whether crossovers which are closer to the observation shall get a higher weight for the analyses. High importance arises for the interpolation error which depends on the large-scale topography. The small-scale topography also causes a dependence on the distance to the closest observation. The error due to the interpolation can be written as

$$\Delta T_{\text{int}}^2(\Delta L_i, \Delta L_j) = C_{SST}^2(\Delta L_i^2 + \Delta L_j^2) + C_{LST}^2(\Delta L_i^2 + \Delta L_j^2), \quad (6.44)$$

$$= (C_{SST}^2 + C_{LST}^2)(\Delta L_i^2 + \Delta L_j^2), \quad (6.45)$$

$$= C^2 \frac{L^2}{4} \left[\frac{(i-1)^2}{I_{\text{max}}^2} + \frac{(j-1)^2}{J_{\text{max}}^2} \right], \quad (6.46)$$

$$\Delta T_{\text{int}}^2(\Delta L_i, \Delta L_j) = \Delta T_{\text{topo}}^2 \left[\frac{(i-1)^2}{I_{\text{max}}^2} + \frac{(j-1)^2}{J_{\text{max}}^2} \right], \quad (6.47)$$

where i and j are the number of crossovers in order of their distance to the next observation point. There are in total I_{max} and J_{max} crossovers. C_{SST} includes the effect due to the small-scale topography, and C_{LST} due to the large-scale topography.

The following relations are valid for selecting a subset of crossovers

$$I \leq I_{\text{max}}; J \leq J_{\text{max}}. \quad (6.48)$$

Summing the errors up

$$\begin{aligned} \sum_{i,j}^{I,J} \Delta T_{ij}^2 &= 2 \Delta T_{\text{meas}}^2 I J + \sum_{i,j}^{I,J} \Delta T_{\text{topo}}^2 \left[\frac{(i-1)^2}{I_{\text{max}}^2} + \frac{(j-1)^2}{J_{\text{max}}^2} \right], \\ &= 2 \Delta T_{\text{meas}}^2 I^2 + \frac{2}{3} \frac{I^4}{I_{\text{max}}^2} \Delta_{\text{topo}}^2, \end{aligned} \quad (6.49)$$

where each crossover has 2 nearest measurements. The effect for the tidal Love number is

$$\delta r_0 h_2 = \sum_{i,j}^{I,J} (T_i - T_j) \frac{1}{IJ}. \quad (6.50)$$

Additionally the topography variation can be written as $\Delta T_{i,j} = \Delta(T_i - T_j)$. The tidal amplitude can then be written as

$$\langle \Delta(\delta r_0 h_2) \rangle^2 = \sum_{i,j} \frac{\Delta T_{ij}^2}{I^2 J^2} = \frac{2\Delta T_{meas}^2}{I^2} + \frac{2\Delta T_{topo}^2}{3I_{max}^2}, \quad (6.51)$$

$$\Delta(\delta r_0 h_2) = \sqrt{\frac{2\Delta T_{meas}^2}{I^2} + \frac{2\Delta T_{topo}^2}{3I_{max}^2}}. \quad (6.52)$$

by using $\sum_{i=0}^n i^2 = \frac{1}{3}n(n+1)(n+2) \approx \frac{n^3}{3}$ for $n > 1$. The upper derivation shows that no advantages are achieved by selecting crossovers for the analysis which have a small $\Delta L_i \Delta L_j$.

7 Discussion of the results

It could be shown that the tidal Love number h_2 can be determined accurately from a simulated laser altimeter data set of Mercury. Three different approaches have been investigated. Two of these approaches are based on a simultaneous extraction of the tidal elevation and the global static topography, while one of them is based on a purely analytical estimate of the uncertainty for the extraction of the tidal signal at orbit crossover points. The determination of the tidal signal with high precision is the main goal of the presented approaches.

In the first approach the global topography is decomposed into an ortho-normal set of global basis functions, where the static component is expressed as a spherical harmonic expansion, while the tidal signal is described by one time-dependent basis function. In this approach, the static topography has to be separated accurately from the time-dependent tidal signal. This implies that the static topography is determined precisely as a by-product of the extraction of the tidal Love number h_2 . The spherical harmonic expansion of the static topography has the advantage that topographic data can easily be compared with gravity measurements of the radio science experiment MORE because gravity data are usually also extracted in the form of a spherical harmonic expansion. This first approach, which uses a direct decomposition of the static topography, however, has the disadvantage that the computation is very time-consuming. Each topographic measurement contributes to all elements of the inversion matrix. The number of these elements is of order l_{inv}^4 , where l_{inv} is the maximum degree of inversion for the spherical harmonic expansion. To keep the simulation time within reasonable limits, the maximum degree of inversion has been limited to $l_{inv} = 64$. Up to this degree, the expansion coefficients $C_{inv,lm}$ and $S_{inv,lm}$ can be determined precisely with a degree error of a few centimeters at low degrees and still less than 1 meter at larger degrees as reported in ch. 4.

With this first approach, not only the tidal Love number h_2 but also the amplitude of forced libration Φ_{lib} could be determined with a precision of about 10 % (2σ -uncertainty). Margot et al. (2007) obtained the libration amplitude with a comparable uncertainty with Earth-based radio-interferometry. High precision can be reached for a resonant orbit with full data coverage of Mercury's surface. Restricting the data coverage significantly increases the uncertainty of the tidal Love number. Using more realistic input data like a non-resonant orbit and limited to spacecraft altitudes below 1000 km, the uncertainty of the tidal Love number h_2 increases significantly by a factor of 3 (Sec. 4.5). The uncertainty of the libration amplitude does not depend on the orbit and restriction of the data coverage. Strongly increased computational effort would lead to higher precisions. It could be shown that the decrease of the uncertainty of the tidal Love number h_2 and amplitude of forced libration Φ_{lib} scales as a power law with the maximum degree of inversion with an exponent of approximately $-2/3$.

In the second approach the static topography is decomposed into local basis functions which only extend over one or a few cells of a quasi-rectangular grid in covering all longitudes and latitudes of Mercury's surface. The main advantage in comparison to the global basis function approach is the shorter computation time. A particular laser shot only contributes to a few coefficients belonging to the surrounding local basis functions. This means, a particular topographic measurement only contributes to a few elements near the diagonal of the inversion matrix. In the approach based on global basis functions, most computation time is used for building up the inversion matrix. This time is substantially reduced by using local basis functions because most off-diagonal elements of the inversion matrix are zero a priori. Three types of local basis functions have been used in longitudinal direction, step functions, "hat" functions, and cubic spline functions. In latitudinal direction, only step functions have been used because the laser shot spacing in latitude is very small (of order 300 m) so that interpolations into areas of the topography with data gaps or with low data coverage by linear and spline functions are not necessary.

Only the tidal signal is retrieved simultaneously with the local basis function expansion of the static topography. The extraction of the libration amplitude with this approach remains to be implemented in the future. The simultaneous extraction of the tidal signal and the static topography expanded into local basis functions gives 1σ -uncertainties of order 1 % for the tidal Love number h_2 which allows to determine the size of the outer liquid core with a precision of less than 10 km. Best results for the tidal Love number are achieved when the output grid has half the resolution in longitude direction in comparison to the chosen resolution of the input topography grid (sec. 5.3). In this case, the longitudinal width of the output grid cell corresponds approximately to the mean longitudinal spacing of the spacecraft ground tracks on Mercury's surface. For realistic orbit scenarios i.e. non-resonant orbit and data coverage limited to spacecraft altitudes below 1000 km, the expansion of the topography into cubic spline functions in longitude direction gave best results. Only for a resonant orbit, the expansion into step functions gives better results for the tidal Love number. A resonant spacecraft orbit has fairly large data gaps between the ground tracks. Presumably, the interpolation of the static topography by linear functions and by spline functions into these data gaps creates artifacts in the tidal signal.

The mean value of the standard deviation for the topographic heights for all grid points which are influenced by a laser shot are chosen to be a global measure of the uncertainty of the extraction of the static topography. This standard deviation is of about 20 m for the case where the number of grid points in longitude direction are equal or half compared to the input topography, and of about 30 m for binning four grid points of the extracted topographic grid in longitude direction compared to the input topography model. Transforming the retrieved topographic grid into a spherical harmonic expansion by using the approach of a projection gives results which are about as precise as the results of the direct expansion of the measured topography into a spherical harmonic representation. The uncertainty is marginally small with less than 1 cm which is a precision of 10^{-5} for the low degrees and orders. Different realistic orbits and spacecraft altitude restrictions did not affect much the precision of the analysis when linear or cubic spline functions have been used. Combining grid points of the input topographic grid for the output rectangular grid is more important. However, when observations are partly not used for simulating that BELA is shut down for thermal reasons decreased the precision of the retrieved Love

number approximately proportionally to the decrease of the number of measurements. Such shut-downs should only be done outside the peri- and apohelion part of Mercury's orbit that the tidal amplitude can be extracted (sec. 5.4.5). Otherwise, the BELA measurements do not cover the regions of maximal tidal signal.

The third approach for the extraction of the tidal Love number h_2 is based on topographic height difference measurements at orbit crossover points which are passed by the spacecraft at times of different tidal phases. Using a crossover analysis of the tidal signal in the Polar Regions shows that the uncertainty of the measured tidal Love number could be less than 3 %. This uncertainty is dominated by the uncertainty of the small-scale topography between two laser shots. Instrumental and positioning uncertainties are only dominant when the crossing point is close to the observation points themselves. This third approach may be applied to double-check results from the two other approaches or in case that for some reason full coverage of Mercury's surface with laser shots will not be achieved.

Baseline for the work with real BELA data will be the second approach including a still to be developed method to retrieve the amplitude of forced libration. The first approach of a direct extraction of the static topography as a spherical harmonic expansion gives rather small uncertainties of less than 1 m for the degree amplitudes up to order 64. However, the spherical harmonic degree of 64 corresponds to a rather rough description of the topography as nodes are separated with a distance larger than 250 km. Using local basis functions the topography is approximated more realistically with a distance between of the grid points of around 5 to 10 km. As MPO's orbit is separated at best by roughly 2 km distance, the grid resolution does not really need to be increased.

The retrieved uncertainty for the tidal Love number in ch. 4 and 5 is in the range of 10–14 % (2σ -uncertainty) for the most realistic case where a non-resonant orbit and a restriction for observations up to 1000 km spacecraft altitude are included. This uncertainty allows retrieving the outer core radius with an uncertainty of several tens of kilometers. The precise knowledge of the internal structure and size of the different layers allows verifying dynamo theories on the generation of Mercury's magnetic field. Planetary evolution models can additionally be improved. It should be possible to find out whether the diffusion of light elements such as sulfur from the inner core to the outer core is driving the dynamo of Mercury's magnetic field.

8 Outlook

The determination of the static topography and its time-dependent variations was presented in the previous chapters. Two different approaches for expressing the topography were analyzed. First the topography was expressed as a spherical harmonic expansion where the basis functions are global (ch. 4), and the tidal elevation amplitude and the forced libration amplitude and their uncertainties are precisely obtained. The second approach used local basis functions, where the global topography is expressed as a rectangular grid (ch. 5). The tidal Love number h_2 is also extracted by using the approach with the local basis functions. Laser shots affect only locally the topography. These are the first detailed investigations for analyzing a global data set of laser altimeter records for time-dependent global parameter of the static topography in planetary science. Another analysis was carried out to investigate the possibility of determining the tidal Love number from crossovers in the Polar Regions of Mercury where the laser shots are denser than in the equatorial region, and because there the amplitude of the tidal Love number and forced libration amplitude are largest. As these are the first detailed investigations, a lot of simplifications are used. Most of the simplifications can be turned into more realistic scenarios in further studies. The most important simplifications which have to be investigated in more detail in the future will be described in the following.

The approaches for analyzing a global data set seem to be promising. The analyses are based on idealized data which can be improved in the usage of more realistic orbits than a pure Keplerian orbit, in the sense that more uncertainties, especially concerning the spacecraft position, can be included. The uncertainties of the spacecraft position and pointing misalignment are set to a common value which can be improved to use more realistic values. On changing the analyses into more realistic uncertainties, also the systematic uncertainties have to be investigated in more detail. Systematic uncertainties will be based on solar radiation which is reflected at Mercury's surface. This limits the possibility of detecting a laser shot with the receiver optics. Furthermore, the temperature variations of Mercury's surface and additionally at the spacecraft are a systematic uncertainty which needs more effort to be investigated. Another source for systematic uncertainties are the gravitational fields of Mercury, the Sun, and Venus, as it is the direct neighboring planet of Mercury, and therefore has largest effect on the determination of the spacecraft position. However, the effect of the gravity field of Venus was investigated to be marginally small, and even too small for a significant change in MPO's position (Van Hoolst and Jacobs 2003). Mercury's gravity field shall be extracted and is an unknown at present state. MESSENGER will investigate and provide a good determination of Mercury's gravity field. Then its gravity field can be assumed as known, and is not an error source any more. The effect of Sun's gravity field shall be investigated by the time-dependent variations of the topography. Systematic errors can therefore not arise due to this gravity field,

as the effect is directly considered by extracting the time-dependent variations, expressed as the tidal Love number h_2 or the forced libration amplitude Φ_{lib} or both. It is further important to test instrumental uncertainties and their effect on their determination, especially for a single laser shot. It is possible to extend the simplifications of Gardner (1982, 1992) to the general equations and investigate them in more detail. This gives a reduction of uncertainties during analyzing the laser altimeter data set. Then pointing misalignment can be investigated in more detail without using simplifications of the equations.

The approaches using global and local basis functions can be improved by extending the input topography model which is right now set up to a maximum harmonic degree of $l_{max} = 1024$ to higher orders. This reduces the effect of the not-modeled part of the topography from 62.5 m to 32.1 m for an increase of the maximum harmonic degree to 4096. A higher resolution of the input topography shall especially improve the mean uncertainty of the global topography, which was retrieved to be in the range of the uncertainty of the small-scale topography. The optimum grid size for an increased maximum harmonic degree for the use of the local basis functions has to be derived either analytically or numerically by simulations. Such tests are not performed right now. A significant increase of the accuracy for the time-dependent variations seems to be possible, when the maximum harmonic degree of the input model is increased. The transformation of the rectangular grid to a spherical harmonic expansion can be improved by using Gaussian points as equal spaced points in latitude direction or on changing the analysis method from a projection to an inversion as done for the global basis functions. If Gaussian grid points are used as latitudinal points, the analyses will have to be tested again.

When more computational power is available or the code is parallelized, further analyses can be performed up to larger degrees of the spherical harmonic expansion of the topography. The uncertainty of the time-dependent variations are found to be dependent on the maximum inversion degree l_{inv} . Determining the topography for smaller scales than 64 will lead to a better knowledge of the time-dependent variations and therefore a better understanding of the internal structure of Mercury's interior. An inversion degree l_{inv} of 16 gives good results for the time-dependent variations. Why such a high accuracy is achieved, is, however, not completely understood and needs more investigations.

The analysis method using local basis functions can be improved in several details. First the direct determination of the libration amplitude can be introduced. The approach of global basis functions determines the forced libration amplitude in a second step simultaneously with the topography and the tidal Love number. The forced libration amplitude is weakly non-linearly dependent on the static topography and the tidal Love number. Initial values for topography and tidal Love number must be known before introducing the libration amplitude as another parameter to be determined. The approach used for global basis functions has also to be implemented and investigated for the local basis functions for retrieving the forced libration amplitude simultaneously with the static topography and the tidal Love number. Right now the analysis of the forced libration amplitude is not taken into account. Furthermore, the structure of the set-up of the basis functions for the libration amplitude has to be addressed, and additionally the inversion matrix, the right-hand-side vector, and result vector have to be extended for the effect of the libration amplitude.

Now only step functions are used as interpolation method in latitudinal direction. Higher order interpolations like linear interpolation or cubic spline interpolation can be

used. Furthermore data gaps which have been started to analyze should be investigated in more detail. The perihelion shift of the spacecraft is not included at all so far. This can either be considered for local basis function or global basis functions.

The analysis of crossovers should be extended to the case where non-Gaussian noise distributions are assumed. This will require a lot of work, as the presented approach of ch. 6 is purely analytical. The approach can additionally be extended to assuming a correlation between the single error components, especially related to positioning and instrumental uncertainties. The small-scale topography would show a further correlation when the equations including positioning and instrumental uncertainties contain information about the surface slope. A laser shot is presently assumed to be a point measurement which is an idealized case.

A laser shot contains additional information like the factor between the tidal Love numbers h_2 and k_2 . This relation is small in comparison to the tidal Love number h_2 which is accurately determined with the presented approaches. k_2 includes the information of potential variations. An accurate determination needs a precise knowledge of the spacecraft position. Furthermore, this additional uncertainty needs more effort for investigations, then the model has to be increased to use these parameters. The simulations have to be changed to include this effect. A precise determination of this factor gives more information about the mass distribution of Mercury's interior. Furthermore, the simulations can be extended to determine other libration amplitudes than the 88-day forced libration amplitude. Other libration amplitudes have been extracted by Earth-based radar interferometry (Margot et al. 2007). These amplitudes have been studied for the laser altimeter, but it is more challenging to extract them. Their uncertainty is limited, especially due to their dependency on the 3 : 2 resonance of Mercury's rotation period and sidereal year. The potential how to determine those amplitudes should be studied.

It will be challenging to adopt the program for investigating real data either for the case of MOLA right now or of real BELA data which will then be available in 2020. More effort will be necessary to implement functions for analyzing a real data set. Furthermore, investigations can be made for a joint analyses of the SIMBIO-SYS pictures and the MORE gravity data.

Bibliography

- Abramov, O., McEwen, A., 2004. An evaluation of interpolation methods for Mars Orbiter Laser Altimeter (MOLA) data. *Int. J. Remote Sensing* **25**, 669–676.
- Abshire, J.B., Smith, J.C., Schutz, B.E., 1998. The Geoscience Laser Altimeter (GLAS). *Space Technology and Applications International Forum, The American Institute of Physics*, 211–214.
- Afzal, R.S., 1994. Mars Observer Laser Altimeter: laser transmitter. *Applied Optics* **33**, 3184–3188.
- Aharonson, O., Zuber, M.T., Rothman, D.H., 2001. Statistics of Mars' topography from the Mars Orbiter Laser Altimeter: slopes, correlations and statistical models. *J. Geophys. Res.* **106**, 23723–23735.
- Aharonson, O., Zuber, M.T., Solomon, S.C., 2004. Crustal remanence in an internally magnetized non-uniform shell: a possible source for Mercury's magnetic field? *Earth Planet. Sci. Lett.* **218**, 261–268.
- Aharonson, O., Zuber, M.T., Neumann, G.A., Head, J.W., 1998. Mars: Northern hemisphere slopes and slope distributions. *Geophys. Res. Lett.* **25**, 4413–4416.
- Anderson, J.D., Colombo, G., Esposito, P.B., Lau, E.L., Trager, G.B., 1987. The mass, gravity field, and ephemeris of Mercury. *Icarus* **71**, 337–349.
- Balogh, A., Giampieri, G., 2002. Mercury: the planet and its orbit. *Rep. Prog. Phys.* **65**, 529–560.
- Balogh, A., Grard, R., Solomon, S.C., Schulz, R., Langevin, Y., Kasaba, Y., Fujimoto, M., 2007. Missions to Mercury. *Space Sci. Rev.* **132**, 611–645.
- Bois, E., Rambaux, N., 2007. On the oscillations in Mercury's obliquity. *Icarus* **192**, 308–317.
- Brenner, A.C., Zwally, H.J., Bentley, C.R., Csathó, B.M., Harding, D.J., Hofton, m.A., Minster, J.-B., Roberts, L., Saba, J.L., Thomas, R.H., Yi, D., 2003. Geoscience Laser Altimeter System (GLAS) - Derivation of range and range distributions from laser pulse waveform analysis for surface elevations, roughness, slope, and vegetation heights. *Algorithm Theoretical Basis Document Version 4.0*, 1–91.
- Breuer, D., Hauck, S.A., Buske, M., Pauer, M., Spohn, T., 2007. Interior Evolution of Mercury. *Space Sci. Rev.* **132**, 229–260.

- Capaccioni, F., De Sanctis, M.C., Piccioni, G., Flamini, E., Debei, S., SIMBIO-SYS International Team, 2005. VIHI: the Visible and Infrared Hyperspectral Imager channel of the SIMBIO-SYS instrument for the BepiColombo mission to Mercury. AAS, DPS meeting #37, #57.02.
- Cavanaugh, J.F., Smith, J.C., Sun, X., Bartels, A.E., Ramos-Izquierdo, L., Krebs, D.J., McGarry, J.F., Trunzo, R., Novo-Gradac, A.M., Britt, J.L., Karsh, J., Katz, R.B., Lukemire, A.T., Szymkiewicz, R., Berry, D.L., Swinski, J.P., Neumann, G.A., Zuber, M.T., Smith, D.E., 2007. The Mercury Laser Altimeter Instrument for the MESSENGER Mission. *Space Sci. Rev.* **131**, 451–479.
- Chen, G., Ezraty, R., 1997. Non-tidal aliasing in seasonal sea-level variability and annual Rossby waves as observed by satellite altimetry. *Ann. Geophysicae* **15**, 1478–1488.
- Christensen, U.R., 2006. A deep dynamo generating Mercury's magnetic field. *Nature* **444**, 1056–1058.
- Christensen, U.R., Wicht, J., 2008. Models of magnetic field generation in partly stable planetary cores: Applications to Mercury and Saturn. *Icarus* **196**, 16–34.
- Connerney, J.E.P., Ness, N.F., 1988. Mercury's magnetic field and interior. In: Vilas, F., Chapman, C.R., Matthews, M.S. (Eds.), *Mercury*. Univ. Arizona Press, Tucson, pp. 494–513.
- Domingue, D.L., Russell, C.T. (Eds.), 2008. *The MESSENGER Mission to Mercury*. Springer-Verlag GmbH, 1.
- Erd, C., den Hartogh, R., Jeanes, A., Owens, A., Pablos, P., Rando, N., Kraft, S., Collon, M., Montella, J., Harris, J., Buis, E.J., Beijersbergen, M., ESA/SCI-A, cosine Research b.v., 2004. BepiColombo Payload Study Document. ESA-SCI (2004)7, ESA/ESTEC, Noordwijk, The Netherlands.
- McEwen, A.S., Robinson, M.S., 1997. Mapping of the Moon by Clementine. *Adv. Space Res.* **19**, p. 1523–1533.
- Freund, R.W., Hoppe, R., 2007. *Stoer/Burlich: Numerische Mathematik 1*. Springer Verlag **10**, Heidelberg, 2007.
- Gardner, C.S., 1982. Target analysis for laser altimeters: An analysis. *Applied Optics* **21**, 448–453.
- Gardner, C.S., 1992. Ranging performance of satellite laser altimeters. *IEEE Transactions on Geoscience and Remote Sensing* **30**, 1053–1068.
- Gold, R.E., Solomon, S.C., McNutt Jr., R.L., Santo, A.G., Abshire, J.B., Acuña, M.H., Afzal, R.S., Anderson, B.J., Andrews, G.B., Bedini, P.D., Cain, J., Cheng, A.F., Evans, L.G., Feldman, W.C., Follas, R.B., Gloeckler, G., Goldsten, J.O., Hawkins, S.E., Izenberg, N.R., Jaskulek, S.E., Ketchum, E.A., Lankton, M.R., Lohr, D.A., Mauk, B.H., McClintock, W.E., Murchie, S.L., Schlemm, C.E., Smith, D.E., Starr, R.D., Zurbuchen, T.H., 2001. The MESSENGER mission to Mercury: scientific payload. *Planet. Space Sci.* **49**, 1467–1479.

- Gunderson, K., Thomas, N., Rohner, M., 2006. A Laser Altimeter Performance Model and Its Application to BELA. *IEEE Trans. Geosci. Remote Sensing* **44**, 3308–3319.
- Harder, H., Schubert, G., 2001. Sulfur in Mercury's core? *Icarus* **151**, 118–122.
- Hauck, S.A., Dombard, A.J., Phillips, R.J., Solomon, S.C., 2004. Internal and tectonic evolution of Mercury. *Earth Planet. Sci. Lett.* **222**, 713–728.
- Head, J.W., Chapman, C.R., Domingue, D.L., Hawkins, S.E., McClintock, W.E., Murchie, S.L., Prockter, L.M., Robinson, M.S., Strom, R.G., Watters, T.R., 2007. The Geology of Mercury: The View Prior to the MESSENGER Mission. *Space Sci. Rev.* **131**, 41–84.
- Heimpel, M.H., Aurnou, J.M., Al-Shamali, F.M., Gomez Perez, N., 2005. A numerical study of dynamo action as function of spherical shell geometry. *Earth Planet. Sci. Lett.* **236**, 542–557.
- Helfenstein, P., Shepard, M.K., 1999. Submillimeter-Scale Topography of the Lunar Regolith. *Icarus* **141**, 107–131.
- Herring, T.A., Quinn, K., 1999. Geoscience Laser Altimeter System (GLAS) - Atmospheric delay correction to GLAS laser altimeter ranges. Algorithm Theoretical Basis Document Version 1.2, 1–22.
- Hofmann-Wellenhof, B., Moritz, H., 2005. *Physical Geodesy*. Springer Verlag **2**, Wien, 2005.
- Jehn, R., Corral, C., Giampieri G., 2004. Estimating Mercury's 88-day libration amplitude from orbit. *Planet. Space Sci.* **52**, 727–732.
- Koch, C., Christensen, U.R., Kallenbach, R., 2008. Simultaneous Determination of global Topography, tidal Love number and libration amplitude of Mercury by Laser altimetry. *Planet. Space Sci.* **56**, 1226–1237, doi:10.1016/j.pss.2008.04.002.
- Koch, C., Christensen, U.R., Kallenbach, R., 2009a. Extraction of the global topography expressed as rectangular grid and the tidal signal from laser altimeter data. *Planet. Space Sci.*, in preparation.
- Koch, C., Christensen, U.R., Kallenbach, R., Hilchenbach, M., 2009b. Study of the interior structure of planetary bodies by laser altimetry. *Advances of Geoscience*, accepted.
- Krebs, D.J., Novo-Gradac, A.-M., Li, S.X., Lindauer, S.J., Afzal, R.S., Yu, A.W., 2005. Compact, passively Q-switched Nd:YAG laser for the MESSENGER mission to Mercury. *Applied Optics* **44**, 1715–1718.
- Kreslavsky, M.A., Head, J.W., 1999. Kilometer-scale slopes on Mars and their correlation with geologic units: Initial results from Mars Orbiter Laser Altimeter (MOLA) data. *J. Geophys. Res.* **104**, 21,911–21,924.
- Kreslavsky, M.A., Head, J.W., 2003. North–south topographic slope asymmetry on Mars: Evidence for insolation-related erosion at high obliquity. *Geophys. Res. Lett.* **30**, PLA 1-1–PLA 1-4, doi:10.1029/2003GL017795.

- Kreslavsky, M.A., Head, J.W., Harmon, J.K., 2008. Large-scale topographic roughness of terrestrial planets: a comparison. 39th Annual Lunar and Planetary Science Conference, March 10-14, 2008, League City, Texas, abstract no. 1472.
- Lucchesi, D.M., Iafolla, V., 2006. The non-gravitational perturbations impact on the Bepi-Colombo Radio Science Experiment and the key role of the ISA accelerometer: direct solar radiation and albedo effects. *Celestial Mechanics and Dynamical Astronomy* **96**, 99–127.
- Margot, J.L., Peale, S.J., Jurgens, R.F., Slade, M.A., Holin, I.V., 2007. Large longitude libration of Mercury reveals a molten core. *Science* **316**, 710–714.
- Milani, A., Rossi, A., Vokrouhlický, D., Villani, D., Bonanno, C., 2001. Gravity field and rotation state of Mercury from the BepiColombo radio science experiments. *Planet. Space Sci.* **49**, 1579–1596.
- Montenbruck, O., Gill, E., 2005. *Satellite Orbits*. Springer Verlag **3**, Heidelberg, 2005.
- Murray, C.D., Dermott, S.F., 1999. *Solar system dynamics*. Cambridge Univ. Press.
- Ness, N.F., 1979. The magnetic field of Mercury. *Phys. Earth Planet. Inter.* **20**, 209–217.
- Neumann, G., 2001. Some Aspects of processing extraterrestrial Lidar data: Clementine, Near, MOLA. *International Archives of Photogrammetry and Remote Sensing*, XXXIV-3/W4 Annapolis.
- Neumann, G.A., Zuber, M.T., Wieczorek, M.A., McGovern, P.J., Lemoine, F.G., Smith, D.E., 2004. Crustal structure of Mars from gravity and topography. *J. Geophys. Res.* **109**, doi:10.1029/2004je002262.
- Niemeier, W., 2002. *Ausgleichsrechnung*. deGryuter Lehrbuch, 2, Berlin, 2002.
- Oberst, J., BELA-Team, 2007. BELA Science Requirements Document. BC-BEL-RS-33001-0-3.
- Peale, S.J., 1972. Determination of parameters related to the interior of Mercury. *Icarus* **17**, 168–173.
- Peale, S.J., 1976a. Does Mercury have a molten core?, *Nature* **262**, 765–766.
- Peale, S.J., 1976b. Orbital resonances in the Solar System. *Ann. Rev. Astro. Astrophys.* **14**, 215–246.
- Peale, S.J., 2005. The free precession and libration of Mercury. *Icarus* **178**, 4–18.
- Peale, S.J., Phillips, R.J., Solomon, S.C., Smith, D.E., Zuber, M.T., 2002. A procedure for determining the nature of Mercury's core. *Meteor. Planet. Sci.* **37**, 1269–1283.
- Pettengill, G.H., Dyce, R.B., 1965. A Radar Determination of the Rotation of the Planet Mercury. *Nature* **206**, 1240.

- Phillips, H.E., Ridgway, J.R., Minster, J.-B., 1999. Geoscience Laser Altimeter System (GLAS) - Tidal corrections. Algorithm Theoretical Basis Document Version 2.0, 1–18.
- Rambaux, N., Van Hoolst, T., Dehant, V., Bois, E., 2007. Inertial core-mantle coupling and libration of Mercury. *Astron. Astrophys.* **468**, 711–719.
- Rummel, R., 2005. Gravity and topography of Moon and planets, Earth, Moon, and Planets. Springer **94**, pp. 103–111.
- Santo, A.G., Gold, R.E., McNutt Jr., R.L., Solomon, S.C., Ercol, C.J., Farquhar, R.W., Hartka, T.J., Jenkins, J.E., McAdams, J.V., Mosher, L.E., Persons, D.F., Artis, D.A., Bokulic, R.S., Conde, R.F. Dakermanji, G., Goss Jr., M.E., Haley, D.R., Heeres, K.J., Maurer, R.H., Moore, R.C., Rodberg, E.H., Stern, T.G., Wiley, S.R., Williams, B.G., Yen, C.L., Peterson, M.R., 2001. The MESSENGER mission to Mercury: spacecraft and mission design. *Planet. Space Sci.* **49**, 1481–1500.
- Schubert, G., Ross, M.N., Stevenson, D.J., Spohn, T., 1988. Mercury's thermal history and the generation of its magnetic field. In: Vilas, F., Chapman, C.R., Matthews, M.S. (Eds.), *Mercury*. Univ. Arizona Press, Tucson, pp. 429–460.
- Smith, D.E., Zuber, M.T., Neumann, G.A., 2001a. Seasonal variations of snow depth on Mars. *Science* **294**, 2141–2146.
- Smith, D.E., Zuber, M.T., Frey, H.V., Garvin, J.B., Head, J.W., Muhlemann, D.O., Pettengill, G.H., Phillips, R.J., Solomon, S.C., Zwally, H.J., Banerdt, W.B., Duxbury, T.C., 1998. Topography of the Northern Hemisphere of Mars from the Mars Orbiter Laser Altimeter. *Science* **279**, 1686–1691.
- Smith, D.E., Zuber, M.T., Solomon, S.C., Phillips, R.J., Head, J.W., Garvin, J.B., Banerdt, W.B., Muhlemann, D.O., Pettengill, G.H., Neumann, G.A., Lemoine, F.G., Abshire, J.B., Aharonson, O., Brown, C.D., Hauck, S.A., Ivanov, A.B., McGovern, P.J., Zwally, H.J., Duxbury, T.C., 1999. The Global topography of Mars and Implications for Surface Evolution. *Science* **284**, 1495–1502.
- Smith, D.E., Zuber, M.T., Frey, H.V., Garvin, J.B., Head, J.W., Muhleman, D.O., Pettengill, G.H., Phillips, R.J., Solomon, S.C., Zwally, H.J., Banerdt, W.B., Duxbury, T.C., Golombek, M.P., Lemoine, F.G., Neumann, G.A., Rowlands, D.D., Aharonson, O., Ford, P.G., Ivanov, A.B., Johnson, C.L., McGovern, P.J., Abshire, J.B., Afzal, R.S., Sun, X., 2001b. Mars Orbiter Laser Altimeter: Experiment summary after the first year of global mapping of Mars. *J. Geophys. Res.* **106**, 23,689–23,722.
- Solomon, S.C., McNutt, R.L., Gold, R.E., Domingue, D.L., 2007. Messenger mission overview. *Space Sci. Rev.* **131**, 3–39.
- Solomon, S.C., McNutt, R.L., Watters, T.R., Lawrence, D.J., Feldman, W.C., Head, J.W., Krimigis, S.M., Murchie, S.L., Phillips, R.J., Slavin, J.A., Zuber, M.T., 2008. Return to Mercury: A Global Perspective on MESSENGER's First Mercury Flyby. *Science* **321**, 59–62.

- Solomon, S.C., McNutt Jr., R.L., Gold, R.E., Acuña, M.H., Baker, D.N., Boynton, W.V., Chapman, C.R., Cheng, A.F., Gloeckler, G., Head, J.W., Krimigis, S.M., McClintock, W.E., Murchie, S.L., Peale, S.J., Phillips, R.J., Robinson, M.S., Slavin, J.A., Smith, D.E., Strom, R.G., Trombka, J.I., Zuber, M.T., 2001. The MESSENGER mission to Mercury: scientific objectives and implementation. *Planet. Space Sci.* **49**, 1445–1465.
- Spohn, T., Sohl, F., Wiczerkowski, K., Conzelmann, V., 2001. The interior structure of Mercury: what we know, what we expect from BepiColombo. *Planet. Space Sci.* **49**, 1561–1570.
- Stanley, S., Bloxham, J., Hutchinson, W.E., Zuber, M.T., 2005. Thin shell dynamo models consistent with Mercury's weak observed magnetic field. *Earth Planet. Sci. Lett.* **234**, 27–38.
- Strom, R.G., Sprague, A.L., 2003. Exploring Mercury – The Iron Planet. Springer Praxis books in astronomy and space science **1**, Heidelberg, 2003.
- Thomas, N., BELA-Team, 2006. BELA Pointing and Alignment Requirements Document. BC-BELA-UBE-TN-0002.
- Thomas, N., Spohn, T., Barriot, J.-P., Benz, W., Beutler, G., Christensen, U., Dehant, V., Fallnich, C., Giardini, D., Groussin, O., Gunderson, K., Hauber, E., Hilchenbach, M., Iess, L., Lamy, P., Lara, L.-M., Lognonné, P., Lopez-Moreno, J.J., Michaelis, H., Oberst, J., Resendes, D., Reynaud, J.-L., Rodrigo, R., Sasaki, S., Seiferlin, K., Wiczerok, M., Whitby, J., 2007. The BepiColombo Laser Altimeter (BELA): concept and baseline design. *Planet. Space Sci.* **55**, 1398–1413.
- Torge, W. 2003. Geodäsie. deGryuter Lehrbuch **2**, Berlin, 2003.
- Van Hoolst, T., Jacobs, C., 2003. Mercury's tides and interior structure. *J. Geophys. Res.* **108**, 7-1–7-16, doi:10.1029/2003je002126.
- Vening Meinesz, F.A., 1950. A remarkable feature of the Earth's topography. *Proc. K. Ned. Akad. Wet.* **53**, 973–974.
- Wicht, J., Manda, M., Takahashi, F., Christensen, U.R., Matsushima, M., Langlais, B., 2007. The Origin of Mercury's Internal Magnetic Field. *Space Sci. Rev.* **132**, 261–290.
- Wiczerok, M.A., 2007. The gravity and topography of the terrestrial planets. *Treatise on Geophysics* **10**, 165–206, doi:10.1016/B978-044452748-6/00156-5, 2007.
- Wu, X., Bender, P.L., Peale, S.J., Rosborough, G.W., Vincent, M.A., 1997. Determination of Mercury's 88 day libration and fluid core size from orbit. *Planet. Space Sci.* **45**, 15–19.
- Yoder, C.F., Konopliv, A.S., Yuan, D.N., Standish, E.M., Folkner, W.M., 2003. Fluid core size of Mars from detection of the solar tide. *Science* **300**, 299–303.
- Yseboodt, M., Margot, J.-L., 2006. Evolution of Mercury's obliquity. *Icarus* **181**, 327–337.

- Zuber, M.T., Smith, D.E., Solomon, S.C., Muhleman, D.O., Head, J.W., Garvin, J.B., Abshire, J.B., Bufton, J.L., 1992. The Mars Observer Laser Altimeter Investigation. *J. Geophysic. Res.* **97**, 7781–7797.
- Zuber, M.T., Aharonson, O., Aurnou, J.M., Cheng, A.F., Hauck, S.A., Heimpel, M.H., Neumann, G.A., Peale, S.J., Phillips, R.J., Smith, D.E., Solomon, S.C., Stanley, S., 2007. The Geophysics of Mercury: Current Status and Anticipated Insights from the MESSENGER Mission. *Space Sci. Rev* **131**, 105–132.
- Zuber, M.T., Smith, D.E., Solomon, S.C., Phillips, R.J., Peale, S.J., Head, J.W., Hauck, S.A., McNutt Jr., R.L., Oberst, J., Neumann, G.A., Lemoine, F.G., Sun, X., Barnouin-Jha, O., Harmon, J.K., 2008. Laser Altimeter Observations from MESSENGER’s First Mercury Flyby. *Science* **321**, 77–79.

Publications

Teilergebnisse aus dieser Arbeit sollen mit Genehmigung der Fakultät für Bauingenieurwesen und Geodäsie in folgenden Beiträgen vorab veröffentlicht werden:

Koch, C., Christensen, U.R., Kallenbach, R., 2008. Simultaneous Determination of global Topography, tidal Love number and libration amplitude of Mercury by Laser altimetry. *Planet. Space Sci.* **56**, 1226–1237, doi:10.1016/j.pss.2008.04.002.

Koch, C., Christensen, U.R., Kallenbach, R., 2009a. Extraction of the global topography expressed as rectangular grid and the tidal signal from laser altimeter data. *Planet. Space Sci.*, in preparation.

Koch, C., Christensen, U.R., Kallenbach, R., Hilchenbach, M., 2009b. Study of the interior structure of planetary bodies by laser altimetry. *Advances of Geoscience*, accepted.

Acknowledgements

I want to try to acknowledge the people who helped and supported me for a successful completion of this thesis.

I firstly want to thank Prof. Dr. Ulrich Christensen who motivated, advised, and allowed me to work in such an interesting project. Furthermore, I want to thank Prof. Dr. Jürgen Müller for supporting me and accepting my thesis. I also want to thank Mr. Prof. Dr. Christian Heipke for being the third referee.

Special thanks belong to Mr. Dr. Reinald Kallenbach who was available when I needed someone for discussing numerical or analytical problems. He further read the thesis before submitting, and helped to improve the language with his remarks.

Thanks also belong to Mr. Dr. Dieter Schmitt, the coordinator of the Research School, for organizing the different talks, lectures and seminars which gave me the chance to improve my knowledge and learn more details about physics. He gives many students and me the chance to work in such a great institute.

This work was supported by the International Max Planck Research School on Physical Processes in the Solar System and Beyond. Reviews by U.R. Christensen, J. Müller, and R. Kallenbach helped to improve the work. I want to thank the directors of the Max-Planck-Institut für Sonnensystemforschung and the Max-Planck-Society for the financial support and the chance for writing my Ph.D. thesis.

Finally, I want to thank my family for supporting me, whenever and wherever it was needed. I appreciate that they encouraged me to follow my dream.

Curriculum Vitae

Persönliche Daten

geboren am 05. April 1979 in Dresden
Familienstand: ledig

Schule/ Bundeswehr/ Studium

- 08/1985 – 07/1991 Gesamtschule "Einetal-Vorharz" in Welbsleben
08/1991 – 09/1991 Europaschule Gymnasium Stephaneum in Aschersleben
10/1991 – 06/1999 Abitur an der Winfriedschule in Fulda, Note 2,8
07/1999 – 04/2000 Grundwehrdienst beim 1. Raketenbattalion in Walldürn
05/2000 – 07/2000 Vorbereitendes Praktikum beim Katasteramt in Fulda
10/2000 – 05/2005 Studium an der Universität Hannover der Fachrichtung
"Vermessungswesen", Note 2,1
10/2003 – 07/2004 Vertiefungsstudium mit Schwerpunkt GPS und physikalischer
Geodäsie und Bearbeitung des Projektes
Präzise Höhenbestimmung mit GPS
10/2004 – 05/2005 Diplomarbeit, Note 1,5
*Implementierung eines neuen Integrators in die 'Lunar
Laser Ranging'- Auswertesoftware und Erzeugung von
Standardlösungen für die zu bestimmenden Zielparameter*

Berufliche Tätigkeiten

- 10/2003 – 09/2004 Hilfwissenschaftliche Tätigkeit an der Universität Hannover
beim Institut für Photogrammetrie und GeoInformation
06/2005 – 07/2005 Hilfwissenschaftliche Tätigkeit an der Universität Hannover
- weitergehende Datenanalyse der Lasermessungen zum Mond
und deren Darstellung sowie weitergehende Softwareanpassungen
08/2005 – 08/2006 Projektingenieur beim Max-Planck-Institut für Sonnensystem-
forschung
- Mitarbeit am BELA- Laseraltimeter der BepiColombo-Mission
- Simulationen zum Testen des Gerätedesigns
09/2006 – Stipendiant an der "International Max Planck Research School
on Physical Processes in the Solar System and beyond" (IMPRS)
beim Max-Planck-Institut für Sonnensystemforschung